LUND UNIVERSITY

Strain Mapping of Single Nanowires

Hammarberg, Susanna

2021

Link to publication

Citation for published version (APA):
Hammarberg, S. (2021). *Strain Mapping of Single Nanowires*. Lund University.

Total number of authors:
1

General rights
Unless other specific re-use rights are stated the following general rights apply:
Copyright and moral rights for the publications made accessible in the public portal are retained by the authors and/or other copyright owners and it is a condition of accessing publications that users recognise and abide by the legal requirements associated with these rights.
• Users may download and print one copy of any publication from the public portal for the purpose of private study or research.
• You may not further distribute the material or use it for any profit-making activity or commercial gain
• You may freely distribute the URL identifying the publication in the public portal

Read more about Creative commons licenses: https://creativecommons.org/licenses/

Take down policy
If you believe that this document breaches copyright please contact us providing details, and we will remove access to the work immediately and investigate your claim.

LUND UNIVERSITY

PO Box 117
221 00 Lund
+46 46-222 00 00

Strain Mapping of Single Nanowires

Susanna Hammarberg

LUND
UNIVERSITY

LICENTIATE THESIS

by due permission of the Faculty of Science, Lund University, Sweden.
To be defended in lecture hall K457 at the Division of Synchrotron Radiation Research, Department of Physics on the 13th of December 2021 at 13:15 pm.

Thesis advisor:

Jesper Wallentin

Faculty opponent
Lindsay Richard Merte

© Susanna Hammarberg 2021

Faculty of Science
Department of Physics
Division of Synchrotron Radiation Research

ISBN
978-91-8039-115-3 (tryck)
978-91-8039-116-0 (pdf)

Table of Contents

List of publications

This thesis is based on the following publications:

I. *High resolution strain mapping of a single axially heterostructured nanowire using scanning X-ray diffraction*

Hammarberg, S., Dagytė, V., Chayanun, L., Hill, M.O., Wyke, A., Björling, A., Johansson, U., Kalbfleisch, S., Heurlin, M., Lauhon, L.J., Borgström, M.T. and Wallentin, J., 2020. *Nano Research*, *13*(9), pp.2460-2468. https://doi.org/10.1007/s12274-020-2878-6

II. *Combining nanofocused X-rays with electrical measurements at the NanoMAX beamline*

Chayanun, L., Hammarberg, S., Dierks, H., Otnes, G., Björling, A., Borgström, M.T. and Wallentin, J., 2019. *Crystals*, *9*(8), p.432. https://doi.org/10.3390/cryst9080432

Publications not included in this thesis, to which I have contributed:

Inducing ferroelastic domains in single-crystal CsPbBr3 perovskite nanowires using atomic force microscopy

Marçal, L.A., Benter, S., Irish, A., Dzhigaev, D., Oksenberg, E., Rothman, A., Sanders, E., Hammarberg, S., Zhang, Z., Sala, S. and Björling, A., Unger, E., Mikkelsen, A., Joselevich, E. Timm, R., and Wallentin, J., 2021. *Physical Review Materials*, *5*(6), p.L063001.

In situ imaging of ferroelastic domain dynamics in CsPbBr3 perovskite nanowires by nanofocused scanning x-ray diffraction

Marçal, L.A., Oksenberg, E., Dzhigaev, D., Hammarberg, S., Rothman, A., Björling, A., Unger, E., Mikkelsen, A., Joselevich, E. and Wallentin, J., 2020. *ACS nano*, *14*(11), pp.15973-15982.

Strain mapping inside an individual processed vertical nanowire transistor using scanning X-ray nanodiffraction

Dzhigaev, D., Svensson, J., Krishnaraja, A., Zhu, Z., Ren, Z., Liu, Y., Kalbfleisch, S., Björling, A., Lenrick, F., Balogh, Z.I. and Hammarberg, S., Wallentin, J., Timm, R., Wernersson, LE. and Mikkelsen, A., 2020. *Nanoscale*, *12*(27), pp.14487-14493.

Coherent Bragg imaging of 60 nm Au nanoparticles under electrochemical control at the NanoMAX beamline

Björling, A., Carbone, D., Sarabia, F.J., Hammarberg, S., Feliu, J.M. and Solla-Gullón, J., 2019. *Journal of synchrotron radiation*, *26*(5), pp.1830-1834.

Nanoscale mapping of carrier collection in single nanowire solar cells using X-ray beam induced current

Chayanun, L., Otnes, G., Troian, A., Hammarberg, S., Salomon, D., Borgström, M.T. and Wallentin, J., 2019. *Journal of synchrotron radiation*, *26*(1), pp.102-108.

Nanobeam X-ray fluorescence dopant mapping reveals dynamics of in situ Zn-doping in nanowires

Troian, A., Otnes, G., Zeng, X., Chayanun, L., Dagyte, V., Hammarberg, S., Salomon, D., Timm, R., Mikkelsen, A., Borgstrom, M.T. and Wallentin, J., 2018. *Nano letters*, *18*(10), pp.6461-6468.

List of abbreviations

2D	Two-dimensional
3D	Three-dimensional
FEM	Finite element modelling
FFT	Fast Fourier transform
HAADF	High angle annular dark field
InP	Indium Phosphide
InGaP	Indium Gallium Phosphide
KB	Kirkpatrick-Baez
LED	Light-emitting diode
NW	Nanowire
STEM	Scanning transmission electron microscopy
STXM	Scanning transmission X-ray microscopy
TEM	Transmission electron microscopy
XBIC	X-ray beam induced current
XRD	X-ray diffraction
XRF	X-ray fluorescence

Abstract

The benefits of producing electronic and optoelectronic devices out of semiconductor nanowires are many and include scalability and improvements in efficiency. The material properties change on this scale and can be significantly different from bulk; one such property is how strain is relaxed. In axial heterostructures, the lattice mismatch at the interface will cause strain in the nanowire. It is of high interest for future electronic devices to determine deviations from a perfect crystal lattice in terms of strain, tilt and imperfections, as it can relate to the electronic properties of the future devices.

The development of X-ray imaging techniques has been limited by the difficulties in producing focusing devices for X-rays. Resent developments in focusing techniques, as well as in increased intensity from synchrotron sources, has given the opportunity to image nanostructures with nanoscale resolution. At MAX IV, the first 4^{th} generation synchrotron source in the world, the updated design means that this synchrotron can deliver higher coherent flux to its experimental stations.

In this thesis, we demonstrate strain mapping of axial heterostructured nanowires and contacted nanowires with high resolution scanning X-ray diffraction. We performed the first scanning X-ray diffraction experiments at the then newly opened beamline NanoMAX at MAX IV, which specializes in delivering highly coherent X-ray nanobeams. We probed a nanowire which was 170 nm in diameter and had three segments of InP with different lengths, 45 nm, 80 nm, and 170 nm., in a $Ga_xIn_{1-x}P$ nanowire. The probe was focused down to 90 nm with a KB mirror setup, and the nanowire was scanned while we measured the 3D Bragg peak from InP and $Ga_xIn_{1-x}P$ simultaneously in each scanning position. This resulted in diffraction maps resolving single nanowire heterostructures and their heterostructure segments. From this, we calculated maps of relative strain that had a relative sensitivity of about 10^{-4}. The strain mapping shows a complex strain profile in the largest segment, with a dome-shaped distribution from the interface, while the smallest segment is almost fully adapted to the $Ga_xIn_{1-x}P$ nanowire. From the diffraction, we also calculated the lattice tilts. The results were compared to simulations from a finite element model, which showed good agreement in both lattice tilt and strain.

Furthermore, we imaged strain of a complete InP nanowire device and combined it with the electric characterization method XBIC that we commissioned at the NanoMAX beamline. Here, we observed that the lattice was strained and tilted by the contacts.

Popular scientific summary

Like visible light, X-rays are electromagnetic waves but with a shorter wavelength which means more energetic waves. X-rays have enough energy to penetrate deep into materials, which makes them a valuable tool for analysis. Scientists use X-rays to investigate materials in many different ways and for different purposes. At the doctor's or dentist's office, X-rays penetrate tissue but are absorbed by bone, and that contrast creates an image of the bones. Around the globe, highly technological facilities called synchrotrons are built to produce high-quality X-ray beams. A "high-quality" beam of X-rays means, among other things, that it has a lot of X-rays in a small spot and of the same energy and that they are travelling in the same direction. X-ray beams are created at several experimental stations around a synchrotron, each designed for different types of experiments.

In this work, we have used an X-ray beam at a synchrotron to study tiny cylinders called nanowires. Their diameter is typically in the order of nanometers (0.000000001 m). For comparison, a sheet of paper or a strain of hair is typically 100 000 nanometers thick. There are many advantages to building electronic devices, like transistors, LEDs, and solar cells, in the nanowire format. One is the reduced amount of material that is needed. Another is the fact that you can make new combinations of materials that are not possible in larger formats. When a nanowire consists of two parts of different materials, it is called a *heterostructure*. The most interesting reason, though, might be that the material properties change at this length scale. Recently, researchers have been finding ways to utilize nanoscale properties to build more efficient devices.

We have studied a nanowire heterostructure of indium phosphide (InP) and indium gallium phosphide (InGaP) manufactured at Lund University. As most solids, these materials are *crystalline*, which means that the atoms are densely packed on a regular grid. In a solid that is not crystalline, for example, glass, the atoms are placed in an unordered fashion. The spacings of the atoms in a solid are on the order of tenths of nanometers. Importantly for this work, different materials have different atom sizes and, therefore, spacings. We have measured detailed maps of *strain* in the InP/GaInP nanowire. When a material is compressed or stretched, the atoms inside it are displaced from their original positions. This displacement is called strain. In a heterostructure, the different materials compress or stretch each other so that strain arises. Nanowires can also be strained when they are produced and processed. The resulting strain, the change in crystal lattice spacing, can be measured with scanning X-ray diffraction. Strain can affect the performance of a nanowire device, and therefore, it is essential to map it out in detail.

In 2016, the very first experiments were performed at the brand new synchrotron facility MAX IV Laboratory in Lund, Sweden. With a new synchrotron design, MAX IV is referred to as the first of the 4th generation of synchrotrons. The improvement in design means that the X-ray beams that it can produce have higher quality. This means that materials can be investigated with higher accuracy and resolution and lead to developments in material science, biotechnology and medicine, among other fields.

As part of this work, we performed the first X-ray diffraction experiment at the experimental station NanoMAX beamline at MAX IV in June 2017, which was also one of the first experiments in general. This beamline focuses on creating highly focused X-ray beams, making it possible to develop strain images of single nanostructures. A lot of factors need to come together for the commissioning of such an experiment, performance of the storage ring, alignment of the beam, IT, the proficiency of the researchers, and many other things. This experiment came together, and we produced strain maps that showed that the strain distribution in the nanowires varied depending on the heterostructure design. In the second part of this thesis, a technique to measure the electric performance of a nanowire device was added to the toolbox at NanoMAX and was measured simultaneously as the composition and strain distribution.

Populärvetenskaplig sammanfattning

Röntgenljus, kallat X-rays på engelska är, precis som synligt ljus, elektromagnetisk strålning fast med kortare våglängd vilket innebär högre energi. Eftersom den har mer energi kan röntgenstrålningen passera genom många material, vilket gör den användbar för materialforskning. Forskare använder röntgenstrålning för en rad olika tekniker som undersöker olika egenskaper hos materialen. Hos läkaren eller tandläkaren så går röntgenstrålning igenom vävnad, men stoppas av ben. Det ger en konstrast mellan vävnad och ben som gör att man får en bild av benen i kroppen. Runt omkring jordklotet finns det flera stora faciliteter som kallas *synkrotroner*. De producerar röntgenstrålning av hög kvalitet som kallas synkrotronljus. Hög kvalitet i det här sammanhanget betyder bland annat att man kan producera en stråle som är koncentrerat till ett litet område, att strålarna färdas i samma riktning och att de har samma energi. Vid en synkrotron finns flera olika experimentstationer som inriktar sig på olika typer av metoder.

I det här arbetet har vi använd synkrotronljus för att studera små cylindrar som kallas nanotrådar. Deras diametrar är i storleksordning av nanometer (0.000000001 m). I jämförelse är ett pappersark eller ett hårstrå ungefär 100 000 nanometer i tjocklek. Det finns många fördelar med att bygga elektroniska komponenter, tex transistorer, LEDs och solceller, i form av nanotrådar. En av fördelarna är att det går åt mindre material för att producera dem. En annan att man kan kombinera material som inte går att kombinera när de är i ett större format. När en nanotråd består av två delar olika material kallas de *heterostrukturer*. Den kanske mest spännande anledningen till att göra komponenter av nanotrådar är att materialets egenskaper ändrar sig på den här längskalan. Forskare jobbar på att utnyttja dessa egenskaper för att bygga mer effektiva komponenter.

Vi har studerat en nanotråd-heterostruktur som består av indiumfosfid (InP) och galliumindiumfosfid (GaInP) som har producerats på Lunds universitet. Som de flesta fasta material är dessa kristaller, vilket betyder att atomerna är packade på ett regelbundet rutnät. I material som inte är kristaller, som till exempel glas, är atomerna helt i oordning. I en kristall är avstånden mellan atomerna i storleksordning av tiondels nanometer. Dessa avstånd är materialspecifika, eftersom olika sorters atomer är olika stora, vilket är viktigt för det här arbetet. Vi har mätt detaljerade kartor av *strain*, eller deformation på svenska, i nanotrådarna. När ett material tänjs eller trycks ihop flyttas atomerna inuti ifrån deras ursprungliga positioner, vilket kallas strain. I en heterostruktur gör skillnaderna i kristallavstånd hos de olika material att det uppstår strain. Det kan också uppstå när nanotrådarna produceras eller när de processas. I den här avhandlingen har vi mätt strain med en metod som heter ”scanning X-ray diffraction”. Anledningen till att det är intressant att mäta de här väldigt små förflyttningarna av atomer är inte bara akademiska, det är också intressant för att det påverkar hur den färdiga komponenten, byggd av en nanotråd, presterar. För att förbättra effektiviteten av nanotrådskomponenter är det därför viktigt att kartlägga strain i detalj.

Under 2016 gjordes de allra första experimenten på den nya synkrotronen i Lund, MAX IV Laboratory. MAX IV har en ny design jämför med andra synkrotroner, och det talas till och med om att det är den första av en ny generation av synkrotroner, den fjärde. Förbättringarna i designen gör att röntgenstrålarna som produceras är av en mycket hög kvalitet. Det gör att material kan undersökas med högre noggrannhet och upplösning och leda till utvecklingen av nya material, och genombrott i forskning i bioteknik, arkeologi och medicin.

Som en del av det här arbetet gjorde vi det allra första experimentet av sitt slag på experimentstationen NanoMAX på MAX IV i Juni 2017. Den här experimentstationen fokuserar på att skapa fokuserade röntgenstrålar som gör det möjligt att titta på strain i enskilda nanostrukturer. Många faktorer måste fungera för att genomföra ett sådant experiment för första gången. Synkrotronen, IT, alla justeringar av röntgenstrålen och dessutom personalen måste leverera. Vi producerade strain-kartor och lyckades visa

hur fördelningen av strain berodde på designen av heterostrukturen. I den andra delen av det här arbetet så adderade vi en ny tekning för att mäta elektrisk prestanda i en nanotrådskomponent på NanoMAX, samtidigt som vi mätte strain och komposition.

Acknowledgements

I would like to thank my supervisor, Jesper Wallentin for the dedicated support during my Ph.D studies so far. You always find time to help and discuss when I have problems, and you help me keep up the enthusiasm for my projects.

I also want to thank my co-supervisors, Alexander Björling and Anders Mikkelsen, for your help and encouragement and for involving me in new projects.

I would like to thank Lert Chayanun, Luças Marcal, Megan Hill, Dmitry Dzhigaev and Andrea Troian for collaborations on beamtimes and data analysis. Thanks to Dagytė, Vilgailė for providing me with samples. Thanks also to all personnel at the NanoMAX beamline for great support during experiments.

At sljus I have gotten too many friends to list them here, so I just say a great thank you to everyone for creating such a nice and friendly working environment.

Finally, thank you to my family for your love and support and to my little family, Johannes and Lone, for filling everyday life with love and joy.

1 Introduction

Nanowires (NWs) are said to be one-dimensional objects because they have a far smaller diameter than length, with diameters on the nanoscale (10^{-9} m). For materials like solids, it is well known that the physics at the surface is typically different from the bulk. Since NWs have such small diameters, the majority of their volume is considered as close to the surface. It is easy to imagine how the properties of a NW, therefore, cannot be described simply in terms of the bulk. This is one of the key insights in nanophysics; the properties of a material can change at the nanoscale. Semiconductors in the form of NWs are commonly used to make photovoltaics [1-3], light-emitting diodes [4-7], and electronics [8-10], and with good reason. Reduced material usage and scalability are two of the advantages [2], and scientists take advantage of the nanoscale properties when designing new devices and use them to increase efficiency.

Another advantage with nanostructures has to do with the variety of materials they can be manufactured from. When two types of semiconductor crystals are grown on top of each other to form a new combination, it is called a *heterostructure*. In the NW form, a larger variety of semiconductors can be combined into heterostructures because of the small diameter [11]. A NW heterostructure can be either radial, with the second material as an inner core, or axial, with alternating segments along the long axis. Because the two materials have different crystal lattice spacing, they *strain* each other, and there will be a transition at the interface where the materials need to adjust. From the strained interface, there will be a gradual change in lattice constant to the relaxed state at a distance from the interface. Investigating the crystal structure in detail is, therefore, not only interesting from a fundamental point of view but an important task toward the goal of producing more efficient devices [12].

How do we create an image of structures of this order of magnitudes? The resolution of an optical microscope is theoretically limited by the diffraction limit. The smallest distance d that can be resolved is

$$d = \frac{\lambda}{2nsin(\theta)}$$

where λ is the wavelength of the light, n is the refraction index that will be discussed in later theory, and θ is the maximum angle of the light, coming from the object, that can be collected. The limit for visible light will be somewhere above 100 nm, and that is for the ideal case with a microscope without any imperfections.

Therefore, to image nanostructures with a relevant spatial resolution, it is necessary to turn to either X-ray or electrons as a probe. Whether the choice is X-rays or electrons depend on the sample, what specific properties are investigated and the demands in terms of sensitivity and resolution. Electron probes give excellent spatial resolution on the atomic level, but electrons, being charged particles, interact more strongly with matter which leads to a shorter penetration depth. Therefore, electrons are better suited for looking at surfaces or alternatively, the sample needs to be prepared in very thin slices in a process that can alter the crystal.

X-rays, being highly energetic, are highly penetrable and enable probing the interior structure of a sample, also when it is embedded. Developments in focusing techniques, as well as an increased intensity in the sources, has given the opportunity to focus hard X-rays down to the nanoscale [13, 14]. If X-rays of the same wavelength diffracts from a nanostructure, the X-rays will interfere and produce a measurable diffracted signal that is related to the crystal structure. Variations in the crystal alter the diffracted signal, and by scanning the structure with a nanofocused X-ray beam, these variations can be imaged. The increased intensity and ability to focus X-ray beams have enabled X-ray diffraction to

become a popular tool to image the strain distribution in single nanocrystal structures [15-18] and in NW devices [19-22].

The experiments in this thesis were performed at MAX IV Laboratory, a synchrotron situated in Lund, Sweden, which is the first operational diffraction-limited storage ring (DLSR) in the world. We performed the scanning XRD experiment at the NanoMAX beamline [23, 24] in June 2017 as one of the beamlines first experiments and the very first of its kind. This beamline takes advantage of the high coherent flux that the facility delivers and produce highly coherent beams that can be focused to the nanoscale.

In this thesis, we investigate the strain in NWs and NW devices using scanning XRD with nanoscale resolution. In the first project, the NW is a $Ga_xIn_{1-x}P$/InP heterostructure with a series of alternating segments of various lengths. We measure strain with high resolution and high strain sensitivity. In more detail, we investigate how the relative length of the segments affects the strain relaxation from the interface. We relate the strain relaxation to the segment size. Furthermore, we build a theoretical model of the NW, which helps us interpret the results.

In the second project, we investigate the strain in a contacted InP NW device. A new setup is developed that enables four different X-ray techniques for a NW device at the NanoMAX beamline. Morphology, composition, strain, and electronic properties are investigated simultaneously. The strain mapping shows a small bending of the NW because of the contacting of the NW, which also leads to strain.

This licentiate thesis is outlined as follows: Chapter 2 deals with the theory behind scanning X-ray diffraction; how and why the X-rays form diffractions patterns when they are scattered off a crystal. Chapter 3 goes through the basics of how a nanofocused X-ray beam is produced at a synchrotron laboratory. In chapter 4, we explain how a nanofocused X-ray beam can be used to investigate single nanostructures. Next, we present the experiment, simulations and results of paper I, strain mapping of $Ga_xIn_{1-x}P$ -InP axial heterostructures in chapter 5. In chapter 6, the experiment and findings of paper II are presented, which investigates strain in a contacted InP NW device. The thesis ends with an outlook and summary in chapter 7.

2 X-ray diffraction from crystals

In which we describe how X-rays propagate, interact with matter, and produce diffraction patterns from which we can measure strain in nanostructures

2.1 The nature of X-rays and their interaction with matter

A year memorized in many X-ray physicists' minds is 1895, the year when W. C. Röntgen discovered X-rays. It was later concluded that X-rays are electromagnetic radiation with higher energy than visible light. X-rays are between ultraviolet light and gamma rays in the electromagnetic spectrum, with energies between 100 eV and about 100 keV. With the development of quantum mechanics in the early 1900s, it was concluded that electromagnetic waves exhibit qualities of both particles and waves. X-rays, like all electromagnetic waves, exhibit typical wave properties such as interference. At the same time, they have particle properties. When looking at light as particles, or quantas of light, they are referred to as photons. The energy of a photon is $E = \frac{hc}{\lambda}$ where h is Planks constant. This *wave-particle duality* holds for all quantum objects such as photons or electrons.

2.1.1 X-ray absorption and scattering

Now we will turn our attention to the ways that X-rays can interact with matter. In the energy range of X-rays, the main process is *photoelectric absorption*. Here, a photon is absorbed by an atom, transferring all its energy to an electron in a core shell which is emitted from the atom, leaving a vacancy. The vacancy is filled with an electron from a higher shell, and the excess energy from that transition is released either as a photon, or it is transferred to an electron in a higher electron shell, called an Auger electron. If it is released as a photon, it is called X-ray fluorescence (XRF), and its energy will be equal to the difference between the energy levels. Since this is element-specific, the XRF will be a fingerprint for that element. The probability for photoelectric absorption to occur is high when the photon energy is just above the binding energy of a core electron. As an example, the cross-section for photoelectric absorption in carbon is displayed in Fig. 1. The cross-section is high when the photon energy corresponds to the binding energy of the core electrons. Above the X-ray energy range, energies no longer correspond to electron binding energies and the cross-section goes to zero. There are peaks in cross-section when the photon energy reaches just above the binding energy of a new shell, and electrons from that shell can be ejected. The edge before the peak, just at the binding energy, is referred to as an absorption edge.

The other main process of interaction for X-rays is scattering. *Compton scattering* occurs when a photon scatters off an electron, and in the interaction, a portion of its energy is transferred to the electron. Since some of the photon energy is lost, this is called *inelastic* scattering.

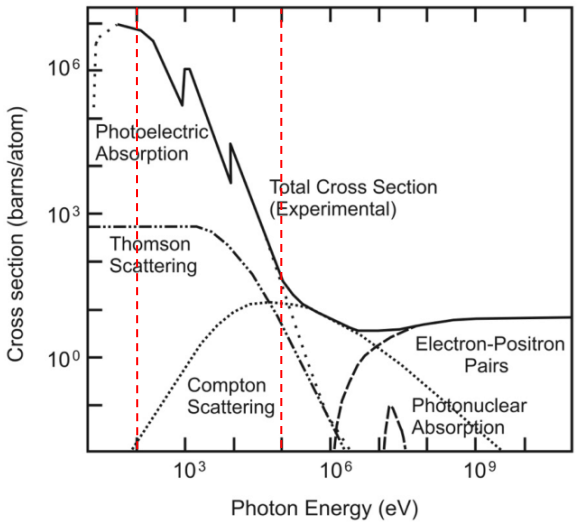

Figure 1 The cross-section for different types of interactions in carbon as a function of photon energy. The approximate energy range of X-rays is marked with red dashed lines. From ref. [25], adapted from ref. [26].

In contrast, in *Thomson scattering,* a photon scatters off an electron without changing its energy. In the interaction, the photon does not give any energy to the electron, but, importantly, it undergoes a phase shift of 180°. Such scattering, which does not involve a transfer of energy, is called *elastic scattering.* In a classical view, the electric field from the light wave sets the electron in an oscillatory motion, creating a dipole. This dipole releases a light wave that has the same energy as the initial light wave. The released wave will always have a phase shift of 180° compared to the initial wave. The description can also be treated fully quantum mechanically. In that description, the photon is absorbed by the electron, which is then excited to a state in the continuum, and in the process of deexcitation back to the ground state, it releases a photon of the same energy.

Thomson scattering is the most important light-matter interaction in this thesis because it is this process that gives rise to diffraction patterns. The diffraction patterns come from constructive interference of scattered photons, and the photons can interfere constructively only when they are coherent, that is, of the same energy and phase. Coherent photons that are Thomson scattered undergo a constant phase shift and no loss of energy, so after the scattering, the photons are still coherent. In contrast, photons that are Compton scattered will be incoherent and cannot interfere constructively to produce a diffraction pattern. As it is the more important process in this thesis, Thomson scattering will be referenced as 'scattering' throughout the rest of the thesis.

2.1.2 Refraction and reflection

In the previous section, the possible light-matter interactions are described in the atomic picture. This can be related to the macroscopic phenomena of refraction and reflection via the refractive index. When light travels from one media into another, it will change direction; this is called refraction. The relation between the incident angle θ_1 and the outgoing angle θ_2 is described by Snell's law:

$$n_1 \sin\theta_1 = n_2\theta_2 \qquad (1)$$

where n_1 and n_2 are the refractive indices of each media. Snell's law describes how the angle of refraction changes when passing between different media. Optical light has a refractive index usually above one (one in vacuum, 1.333 in water). For X-rays, the refractive index is often expressed as:

$$n = 1 - \delta + i\beta \qquad (2)$$

where the correction term δ is related to Thomson scattering and β to absorption. For hard X-rays, δ is in the order of 10^{-5} while β is in the order of 10^{-6}, and hence, the refractive index for X-rays is close to

and slightly below one. Looking at Snell's law, it is evident that if the refractive indices deviation from one is small, the change in refraction angle will be slight. Since this is true for X-rays, it has the consequence that it is harder to make lenses and other optical elements for X-rays than for optical light. Furthermore, if the incidence media is vacuum, $n_1 = 1$, and n_2>1 as for optical light, as a consequence: $\theta_1 < \theta_2$. On the other hand, if n_2<1, then $\theta_1 > \theta_2$. This means that X-rays will refract in the opposite direction compared to optical light and, as a consequence, a lens that focuses optical light (convex) will, on the contrary, diverge X-rays.

It is not possible to create a mirror with total internal reflection, as for optical light, but a corresponding total *external* reflection is possible. For total external reflection, the critical angle between the incident photon and the flat surface of the mirror is

$$\alpha_{crit} = \sqrt{2\delta} \tag{3}$$

So, for a surface to work as a mirror for X-rays, the incidence angle must be below the critical angle, which for X-rays is in the order of milliradians.

2.1.3 Fraunhofer diffraction

Electromagnetic waves like X-rays consist of an electric ***E(r,t)*** field and a magnetic ***B(r,t)*** field, which is often described by a single complex scalar field $\psi(\boldsymbol{r}, t)$. It is often approximated as a plane wave which is described by:

$$\psi(\boldsymbol{r}, t) = \mathrm{A}e^{\mathrm{i}(\mathbf{k}\cdot\mathbf{r}-\omega\mathrm{t})} \tag{4}$$

where the exponential term is the phase factor and ***(k·r-wt)*** is referred to as the *phase*, while *A* is the amplitude. Often, a wave is described in terms of its wave vector ***k,*** which specifies the direction of the wave and has the magnitude: $|\boldsymbol{k}| = \frac{2\pi}{\lambda}$.

When a photon scatters off a sample, a spherical wave is released in each scattering event. The outgoing wave becomes a sum of spherical waves. In the *far-field limit*, or *Fraunhofer regime*, the spherical waves have propagated and can be approximated as plane waves. This occurs when the sample to detector distance *R* is:

$$R \gg \frac{a^2}{\lambda} \tag{5}$$

where *a* is the length scale of interest in the sample and λ is the wavelength of the radiation. The propagation of the time independent exit wave to the far-field corresponds to a Fourier transform:

$$\Psi(\boldsymbol{q}) = \mathcal{F}\psi(\boldsymbol{r}) = \int \psi(\boldsymbol{r}) e^{i\boldsymbol{q}\cdot\boldsymbol{r}} d\boldsymbol{r} \tag{6}$$

which is a very important relationship. The intensity, *I*, measured on a detector in the far-field is equal to:

$$I = |\Psi(\boldsymbol{q})|^2 \tag{7}$$

The phase term of $\Psi(\boldsymbol{q})$ disappears in the complex conjugate multiplication in Eq. (7), so the intensity is proportional only to the amplitude of $\Psi(\boldsymbol{q})$, and not the phase. Hence, we cannot directly measure the phase of $\Psi(\boldsymbol{q})$, and the information that is encoded in the phase is lost. Because of the loss of the phase information, an inverse Fourier transform of $\sqrt{I}$, does not generate the correct $\psi(\boldsymbol{r})$, this is known as the *phase problem*.

2.2 X-ray diffraction from crystals

2.2.1 Crystal structure

The different states of matter that can form when atoms come together are, in essence, solids, liquids, gases, and plasmas. In a solid, the atoms are densely packed, either ordered (crystalline) or unordered (amorphous). In crystals, the atoms are sitting on a regular grid, a crystal lattice. The spacing of the lattice is in the order of a few Ångström (0.1 nm). The atoms positioned at every lattice point can be referred to as the basis. The basis can be one or several atoms of the same or different types. The lattice repeats itself many times in all three dimensions. Sometimes the same lattice is repeated throughout the whole material, such as in table salt, and the lattice structure on atom level becomes visible at the macroscopic level. More often, as with metals, the material consists of grains of crystals of varying size and orientation; it is then called polycrystalline. Most semiconductors are crystals. When grown in nanostructure form, it is under very controlled conditions with a clear goal for the crystal structure.

A unit that can be repeated to make up the lattice is called a *cell*. The smallest cell that can be constructed is the *unit cell*. A cell is spanned by the basis vectors $(\boldsymbol{a}_1, \boldsymbol{a}_2, \boldsymbol{a}_3)$. There is a classification system for all cells that can make up a lattice. In the *cubic system*, all sides of the cell are of equal length, $|\boldsymbol{a}_1| = |\boldsymbol{a}_2| = |\boldsymbol{a}_3| = a$.

Any point in the lattice can be reached by the lattice vector $\boldsymbol{R}_n$:

$$\boldsymbol{R}_n = \mathrm{n}_1\boldsymbol{a}_1 + n_2\boldsymbol{a}_2 + n_3\boldsymbol{a}_3 \tag{8}$$

Where n_1, n_2, n_3 are integers. The *reciprocal lattice* is the Fourier transform of the real space lattice, and it is a key concept to understand crystal diffraction. The reciprocal lattice vector is:

$$\boldsymbol{G}_{hkl} = \mathrm{h}\boldsymbol{a}_1^* + k\boldsymbol{a}_2^* + l_3\boldsymbol{a}_3^* \tag{9}$$

where (h, k, l) are integers called the Miller indices, and the reciprocal basis vectors are defined as:

$$\boldsymbol{a}_m^* = 2\pi\frac{\boldsymbol{a}_n^* \times \boldsymbol{a}_p^*}{\boldsymbol{a}_m^* \cdot (\boldsymbol{a}_n^* \times \boldsymbol{a}_p^*)} \tag{10}$$

Diffraction patterns are physical representations of the reciprocal lattice. If the diffraction patterns are measured such that the reciprocal lattice can be mapped out, the crystal lattice can be found through a Fourier transformation.

The Miller indices are also used to signify a unique crystal plane in the real space unit cell. The indices describe where the plane cuts the lattice axes. When designating a plane, the indices are written in brackets, i.e., *(100)*. The spacing between the planes *(h,k,l)*, sometimes called the *d-spacing*, is denoted d_{hkl}. In a cubic system, the relation to d_{hkl} is:

$$\frac{1}{d_{hkl}^2} = \frac{h^2+k^2+l^2}{a^2} \tag{11}$$

The d-spacing for other types of lattices are calculated in similar manners, see for example [27].

2.2.2 X-ray diffraction from a crystal

In 1912, Max von Laue suggested that a lattice made up of atoms on a grid might work as a diffraction grating for X-rays. The idea behind this suggestion is that for light to diffract off matter, there has to be a distance in the matter that is on the same length-scale as the wavelength of the light. The wavelength of X-rays corresponds to the length-scale of the distance between the lattice planes in a crystal (1 Å). In an experiment based on this suggestion, a beam of X-rays were sent through thin slabs of crystals, and

diffraction patterns were indeed recorded. Laue's idea, and the wave natured aspect of X-rays, was confirmed.

We want to arrive at a description for the diffraction from crystals. Throughout, the kinematic approximation will be used, which means that the scattering is weak with no multiple scattering events.

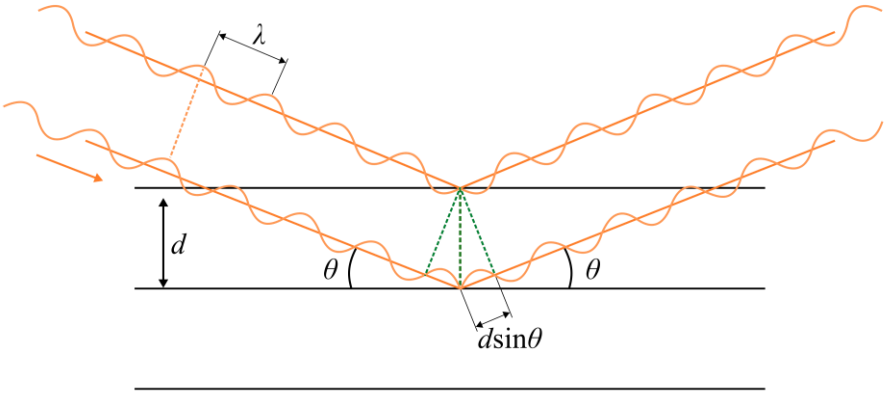

Figure 2 An illustration of Bragg's law. Three planes are separated by a distance *d*. Two incoming waves with wavelength λ travels to the planes with an incoming angle θ and scatter off the first and second planes. At the scattering event, the phase is shifted with 180°. After the scattering event, the second wave has travelled a distance $2d\sin\theta = \lambda$ further than the first wave, and the waves are again in phase.

First, we can derive a simple relationship by imagining the crystal planes as mirrors. Consider a crystal lattice with planes separated by a distance *d*, see Figure 2. A beam of coherent X-rays of wavelength λ, travels to the planes with an incoming angle θ. One ray scatters off the first plane and a second ray scatters off the second plane. To get maximum constructive interference from these two rays, they should be in phase. That is, the additional path the second wave travels is equal to a multiple of λ. Looking at the geometry in Figure 2, the extra path is equal to $2d\sin\theta$. Whichever plane the second ray scatter off, the extra path will be a multiple of $2d\sin\theta$. It follows that the condition for maximum constructive interference from the scattered X-ray beam is:

$$2d\sin\theta = n\lambda \qquad (12)$$

This is Bragg's law, and the peak in intensity that appears at the Bragg condition is called a *Bragg peak*. The Bragg peak is one of the lattice points in the reciprocal lattice of the crystal. Looking at both sides of this equation, it is notable that the wavelength must be of a similar magnitude as *d* for the condition to hold.

Bragg's law is easy to understand but not sufficient to describe X-ray diffraction. To get a more complete model of crystal diffraction, it is useful to introduce vector notation for the scattering wave. In Fig. 3, scattering from two volume elements in a crystal is illustrated. $\boldsymbol{k}$ and $\boldsymbol{k}'$ represents the incoming and outgoing wave, respectively. Since we consider elastic scattering, the magnitude is the same for the incoming and the outgoing wave $|\boldsymbol{k}'|=|\boldsymbol{k}|$.

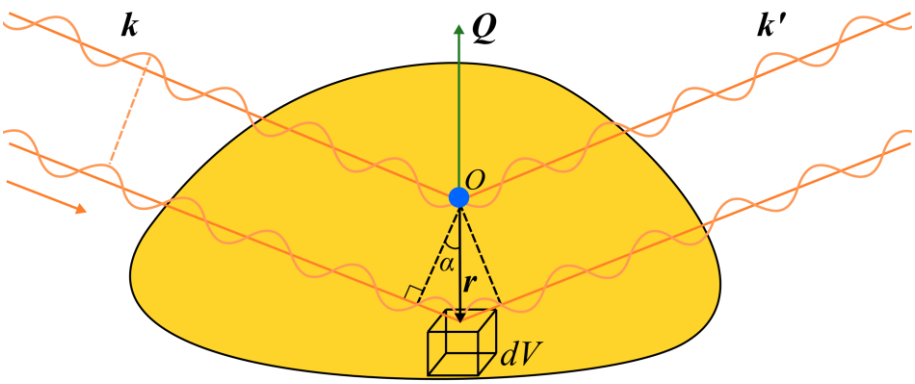

Figure 3 Two waves scatter from two volume elements in a crystal, one from point *O* and one from point *O*+$\boldsymbol{r}$. The total phase difference between the two waves is $\boldsymbol{k}\cdot\boldsymbol{r}-\boldsymbol{k}'\cdot\boldsymbol{r}$.

Comparing waves scattering from the point *O*, and point *O*+$\boldsymbol{r}$, a wave at *O*+$\boldsymbol{r}$ has travelled an additional path of $|\boldsymbol{r}|sin(\alpha)$. In one wavelength, the phase shift is 2π so to get the phase shift of the extra path, it is divided with λ and multiplied with 2π. Thus, the difference in phase between two waves at point *O* and *O*+$\boldsymbol{r}$ is: $\Delta\phi = \frac{2\pi}{\lambda}|\mathbf{r}|\sin(\alpha) = |\mathbf{k}||\boldsymbol{r}|\sin(\alpha) = |\mathbf{k}||\boldsymbol{r}|\cos(90°-\alpha)$, which is the scalar product $\boldsymbol{k}\cdot\boldsymbol{r}$. In the same manner, the phase difference between the outgoing wave from point *O* and from *O*+$\boldsymbol{r}$ is equal to the scalar product $-\boldsymbol{k}'\cdot\boldsymbol{r}$. The total phase difference is $\boldsymbol{k}\cdot\boldsymbol{r}-\boldsymbol{k}'\cdot\boldsymbol{r}$. This phase difference defines what is known as the *scattering vector*, or *Q-vector* $\boldsymbol{Q}$:

$$(\mathbf{k}'-\mathbf{k})\cdot\mathbf{r} = \mathbf{Q}\cdot\mathbf{r} \qquad (13)$$

Thus, the phase factor that is added to the second wave scattering from *O*+$\boldsymbol{r}$, relative to the first one, is $e^{-i(\boldsymbol{k}'-\boldsymbol{k})\boldsymbol{r}} = e^{-i\boldsymbol{Q}\boldsymbol{r}}$. When adding up the coherent sum of scattering from a sample in the direction $\boldsymbol{k}'$, they are each added with this phase factor. In X-ray scattering, the photons interact with the electrons in the atoms, not the nucleus. Hence, the amplitude of the scattered wave travelling in direction $\boldsymbol{k}'$ will depend on the electron density $\rho(\boldsymbol{r})$ in the crystal. It will also be proportional to the phase factor $e^{-i\boldsymbol{Q}\cdot\boldsymbol{r}}$. Following ref. [27], if *dV* is a volume element in the crystal, the amplitude of the scattered wave in the far-field is proportional to the *scattering amplitude* $\boldsymbol{A}$, defined by the integral over all volume elements:

$$\boldsymbol{A}(\boldsymbol{Q}) = \int \rho(\boldsymbol{r})e^{-i\boldsymbol{Q}\cdot\boldsymbol{r}}dV \qquad (14)$$

This equation is equivalent to a Fourier transform; the electron distribution is related to the scattering amplitude with a Fourier transform. The electron distribution in a crystal has some special properties. Since the base describing the atoms in the lattice is periodic, so is $\rho(\boldsymbol{r})$. Hence, $\rho(\boldsymbol{r})$ can be expanded in a Fourier series, and Eq. (12) becomes:

$$\mathbf{A}(\mathbf{Q}) = \sum_{\boldsymbol{G}}\int n_{\mathrm{G}}e^{i(\boldsymbol{G}-\boldsymbol{Q})\cdot\boldsymbol{r}}dV \qquad (15)$$

It can be shown that $\boldsymbol{G}$ in Eq. (15) is the reciprocal lattice vector $\boldsymbol{G}_{hkl}$ [27]. For scattering in the $\mathbf{k}'$ direction, $\boldsymbol{A}$ is non-zero when the scattering vector is equal to a reciprocal vector. This is the Laue condition:

$$\mathbf{Q} = \mathbf{G}_{\mathrm{hkl}} \qquad (16)$$

This condition is equivalent to Bragg's law. The reciprocal lattice vector is orthogonal to the real space lattice planes *(h,k,l)*. With d_{hkl} representing the spacing between the planes *(h,k,l)*, the relation to the reciprocal lattice vector is:

$$d_{hkl} = \frac{2\pi}{|\mathbf{G}_{\mathrm{hkl}}|} \tag{17}$$

Hence, d_{hkl} can be found from the length of the Q-vector when the Bragg condition is met. In other words, d_{hkl} can be found by measuring the position of the Bragg peak in reciprocal space. This fact is central to this thesis and will be discussed further later on.

3 X-ray physics

In which we describe the methods to produce hard X-ray beams with a synchrotron and focus them to the nanoscale

3.1 Synchrotrons as X-ray source

Synchrotrons are particle accelerators that are used to produce high-quality X-ray beams. When charged particles travelling at speeds close to the speed of light are accelerated in a circular motion, they produce synchrotron radiation.

In a synchrotron, electrons are first produced with an electron gun and successively accelerated in a series of radiofrequency fields, called a linear accelerator, until they reach speeds close to the speed of light and energies in the GeV range. Next, bunches of electrons are sent into a *storage ring*, where they are travelling in a loop, kept in the path of the ring using bending and focusing magnets. Even though some synchrotron light is produced by the bending magnet, the main part is produced with a more complicated set of magnets that are placed in units around the storage ring, *insertion devices*. There is an insertion device in the storage ring for each experimental station at the synchrotron. There are two types of insertion devices, *undulators* and *wigglers*. In both types, the electrons are bent in a sinusoidal path, using a series of dipole magnets, one period for each dipole. For each period, synchrotron radiation is produced and added up to an X-ray beam. The synchrotron beam then travels towards an experimental station through a *beamline*. Depending on what type of experiment the experimental station focuses on, the beamline has a specialized set of elements to optimize the beam for that experiment. Synchrotron radiation has applications in many fields of science, medicine, and industry, probing the electronic or atomic structure of matter.

It is not obvious what is meant with a high-quality X-ray beam, and the needed properties vary depending on the technique. For XRD, we want a high number of coherent photons in a small area. They should be both spectrally and spatially coherent, i.e., they should be of the same wavelength and travel in the same direction. This is summed up by a quantity called *brilliance*, which can be understood by looking at its unit:

$$[brilliance] = \frac{photons}{second \cdot mrad^2 \cdot mm^2 \cdot 0.1\%BW}$$

For high brilliance, what is needed is a high flux (photons/second), a small angular divergence of the beam (which is a measure of how much the beam is spreading), source size, and small bandwidth (BW) (the wavelength range that is within 0.1% of the central frequency). The angular divergence and photon source size multiplied is known as the *emittance*. The emittance should be minimized for the brilliance to be high. The source size is limited by the *diffraction limit*, if the source size is smaller than that, it will increase the angular divergence, so it also sets a limit to the emittance and, in turn, the brilliance.

MAX IV, the first diffraction-limited storage ring in the world, was commissioned and ready for its first experiment in 2016. The storage ring has a new design that reduces the emittance of the electron beam, and in turn, the emittance of the X-ray beams. The facility consists of two storage rings, one with electron energies of 3 GeV for hard X-ray experiments and one at 1.5 GeV for soft X-ray experiments. Several synchrotrons around the world are planning to update to the DLSR design. MAX IV also have plans to expand the facility with a free-electron laser (FEL), which can deliver pulsed X-ray beams for investigations of time-resolved processes.

3.2 X-ray focusing optics

To produce an image of a nanostructure, we need to scan it with an X-ray beam that is in the same order of magnitude in size as the object. When the X-ray beam is produced in the storage ring and enters a beamlines' front end, it is polychromatic. To make it coherent in wavelength, it is sent through a monochromator to select a certain wavelength and bandwidth. Most often, this is done with a crystal that diffracts a certain wavelength in one direction, according to Braggs law Eq. (12). Next, to scale down the beam, one could use slits and pinholes, but this would waste most of the flux. Instead, we want to focus the beam to the nanoscale. The challenge of focusing an X-ray beam, in contrast to an optical beam, comes from the fact that the refractive index is very close to one. There are three types of elements: diffractive, refractive, and reflective.

In the diffractive class are *Fresnel zone plates* (FZPs, or zone plates), which consist of a circular plate with concentric rings on top, forming a kind of diffraction grating. Every other ring is phase shifting or absorbing, making incoming X-rays diffract at the interfaces. Each ring has a decreasing width, starting with the thickest at the centre. The resolution is given by the size of the outermost ring. At each interface, the X-rays are diffracted with a different angle. X-rays of the same wavelength are divided in diffracted orders m outgoing in discrete angles. The decreasing size of the rings makes each order exit the grating with a larger angle. The radiuses of the interfaces are determined in such a way that the orders interfere constructively at a focus spot. Different wavelengths will diffract to different focus spots. Typically, only the focus from the first order of diffraction is kept, while the others are removed with a beam stop or other apertures. A big part of the beam intensity will therefore be lost.

Compound refractive lenses (CRLs) is an element that, despite the low refractive index of X-rays, use refraction to focus the beam. As mentioned in chapter 2, Snell's law explains why a convex lens focuses optical light, while for X-rays, it is the concave lens that focuses. With a low refracting index, one would normally require a very long focal length (~100 m) to focus the beam [28]. To overcome this, the CRL consists of a series of concave lenses with small curvatures, where each succeeding lens increases the focus. The lenses are formed by making a series of holes in a block of low absorbing material. The material between the holes forms the lenses.

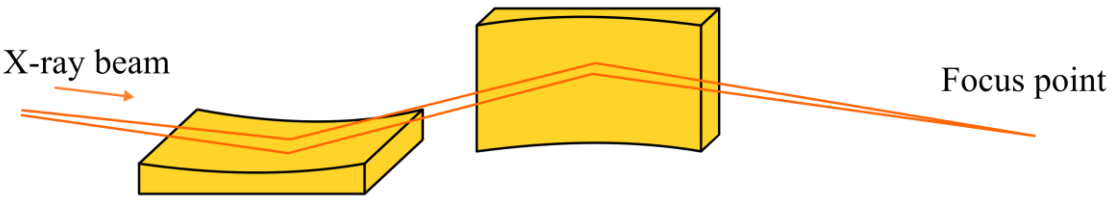

Figure. 4 An X-ray beam focused with a set of KB mirrors, one mirror focusing vertically and one horizontally.

The focusing method used in this work was of the reflective kind. Kirkpatrick-Baez (KB mirrors) [29] are a pair of concave curved mirrors, see Fig. 4. One mirror focuses vertically and one horizontally to a single focus point. For the material to work as mirrors, the incidence angle must be below the critical angle, Eq. (5). The curving of the mirror is slight so that the surface can be seen as flat locally, and the equation is still valid [30]. The mirrors consist of a layer of material coated with a high electron density material like gold or iridium. The δ in Eq. (5) is proportional to electron density so that a high electron density will increase the critical angle, making the experimental gracing incidence setup easier to achieve. The advantage of using KB mirrors or other reflective elements is that if high reflectivity can be achieved, the efficiency is very high. Unlike FZPs and CRLs, the beam position is the same for all energies since the focusing is achromatic.

4 Spatially resolved strain mapping

In the previous chapter, it was explained how a synchrotron X-ray beam can be focused to the nanoscale. It is now possible to resolve variations inside single NWs, by scanning the X-ray beam over the NW. By detecting the Bragg diffraction, information about the local strain will be encoded in the signal. In this chapter, we will describe how the strain information can be extracted to produce high-resolution strain maps from a scanning XRD experiment.

4.1 X-ray diffraction from strained crystals

4.1.1 Strain

In chapter 2, we discussed the structures of crystals and how they are built up by units that are equally spaced on a lattice. In general, however, crystals are not perfect but distorted in different ways. The lattice can, for example, be tilted, or there might be a unit or atom missing in the lattice, which is called a *vacancy*. If the lattice is stretched or compressed so that the lattice points deviate from the ideal lattice points, then the lattice is strained.

Strain is typically modelled with a linear elasticity model, also in nanostructures. The model is based on Hooks law of elasticity, $F = kx$, which says that there is a linear relationship between the applied force F to the object and the displacement x with a proportionality constant k that depends on the object. This is valid as long as x is small. The displacements investigated in paper I and II are a fraction of the lattice constants and are therefore valid under this assumption.

As a simple example of elastic strain, imagine a rod originally with length l_0 that is fixed to the wall in one end while pulled in one end with a force F. By the force, it is displaced to the length l. The magnitude of the displacement will depend on the elasticity of the rod. In the elastic approximation, when the force is removed, the displacement goes back to zero. It is useful to relate this to the concepts of stress and strain. In the example of the rod, the force is applied normal to the rod's cross-section A. The stress is the force per unit area $\sigma = \frac{F}{A}$ while the strain is the relative displacement $\epsilon_x = \frac{l-l_0}{l_0}$, which in the limit of small displacements becomes the derivative. From this equation, we see that strain is a dimensionless quantity. It is positive if it is stretched and negative if it is compressed. When stretching the rod along x, it will also contract along y and z to preserve the volume. The relation is given by Poisson's ratio ν such that:

$$\epsilon_i = \nu\epsilon_j \tag{18}$$

In a more general description of strain, we first introduce the concept of the *displacement field* $\boldsymbol{u}(\boldsymbol{r})$, describing the displacements from the ideal lattice. Here, $\boldsymbol{u}(\boldsymbol{r})$ is a three-dimensional vector field so that each point in space is attributed to a vector that describes the direction and magnitude of the displacement in that point. After displacement, an atom that used to be at $\boldsymbol{r}$ will now be at $\boldsymbol{r}' = \boldsymbol{r} + \boldsymbol{u}(\boldsymbol{r})$. The strain is related to the displacement field by

$$\epsilon_{ij} = \frac{1}{2}\left(\frac{d\boldsymbol{u}_j}{dx_i} + \frac{d\boldsymbol{u}_i}{dx_j}\right) \tag{19}$$

where $\epsilon_{ij} = \epsilon_{ji}$ so that there are six independent components completely describing the strain state: $(\epsilon_{xx}, \epsilon_{xy}, \epsilon_{xz}, \epsilon_{yy}, \epsilon_{yz}, \epsilon_{zz})$. Note the discrepancy between displacement and strain; a crystal is displaced when a wedding ring is moved from one finger to the another, but that does not mean it is strained; the atoms are still in the same place relative to each other. Adding a constant term doesn't change the derivative.

4.1.2 Strain origins: strain from a lattice mismatch

Strain in nanostructures can have many origins, for example, from mechanical force or piezo-electric fields. Crystal distortions such as dislocations lead to strain around the dislocation. In paper I, the strain comes from the heterostructure lattice mismatch, see the discussion below. In paper II, the strain instead comes from the metal contacts attached to the NW. The NW is contacted in both ends, which strains and bends the NW. In both papers, there is also some strain originating from the junction between the gold seed particle and the rest of the NW.

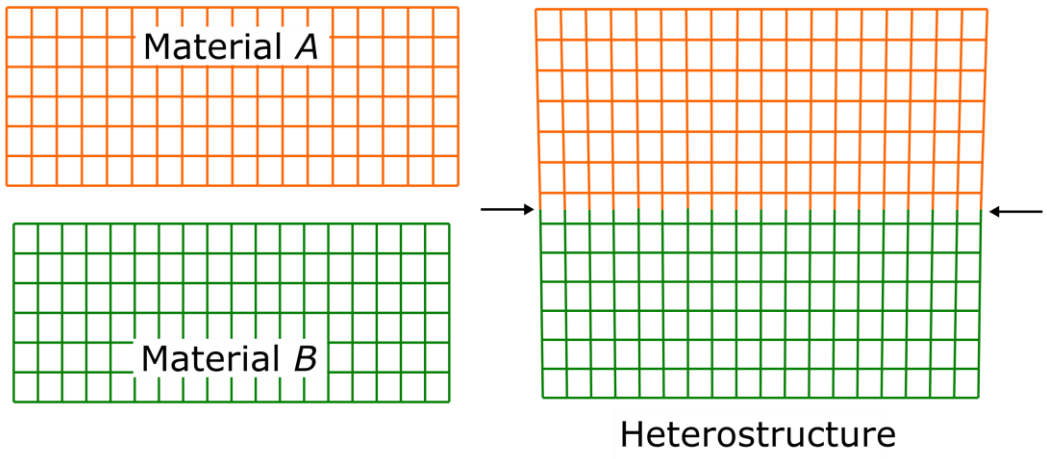

Figure 5 Two materials A and B (left) with lattice constants $a_A > a_B$ form a heterostructure (right). The heterojunction is indicated with two arrows in the heterostructure to the right.

An axial NW heterostructure is formed by growing two materials, *A* and *B*, on top of each other, see Fig. 5. Because they have different lattice constants a_A and a_B, their lattices do not match. At the interface, the lattices need to adjust to each other to form a continuous material. Hence, the materials will be strained at the interface. If a_A and a_b are too different, the mismatch strain can be released by forming one or more dislocations (this is not elastic relaxation). The initial lattice mismatch strain, in the absence of dislocations, is given by:

$$\epsilon_{mismatch} = \frac{a_A - a_B}{a_B} \qquad (20)$$

From the interface, the lattice mismatch strain will be gradually relaxed, and at some distance, the materials will be relaxed or unstrained. The material will try to preserve its volume, so a strain at the interface will also give an opposite strain normal to the interface that follows Poisson's ratio, Eq. (18). If $a_A > a_B$, material *A* will relax by compressing the lattice at the heterojunction axis and expand normal to the heterojunction. The opposite will be true for material *B*.

4.1.3 Diffraction

As we saw in Eq. (15), the scattering amplitude from a crystal will be non-zero when the Laue condition is fulfilled. If there is a presence of strain, the lattice vector $\boldsymbol{R}$ will be locally shifted by the displacement

field $\boldsymbol{R}'(\boldsymbol{r}) = \boldsymbol{R} + \boldsymbol{u}(\boldsymbol{r})$. As the reciprocal space vector $\boldsymbol{G}_{hkl}$ is related to $\boldsymbol{R}$, $\boldsymbol{G}_{hkl}$ will also be shifted. The shift that the displacement field induces will appear in the scattering amplitude as an additional phase factor $e^{i\boldsymbol{G}_{hkl}\cdot\boldsymbol{u}(\boldsymbol{r})}$. Depending on how $\boldsymbol{u}(\boldsymbol{r})$ changes locally in the crystal, the Laue condition will be fulfilled at slightly different Q-vectors.

The effects from strain and lattice tilt on the Bragg peak in reciprocal space are illustrated in Fig. 6. Fig. 6 (a) shows a reference lattice with lattice plane distance *d*. In Fig. 6 (b), *d* is slightly smaller; the crystal is uniformly compressed in one direction. Strain changes the length of $\boldsymbol{G}_{hkl}$, see Eq. (17). The lattice can be either stretched (tensile strain) or compressed. This will make $\boldsymbol{G}_{hkl}$ shorter and longer, respectively. *Tilt* is when the lattice is rotated; this will shift the position of the Bragg peak, Fig. 6 c). A rotation of the real space lattice corresponds to a rotation of the reciprocal lattice. Note that the strains and tilts in Fig. 6 are exaggerated for clarity. The task in scanning XRD is to track the movement of the Bragg peak in 3D space for each point on a measurement grid, and with that, track the change in strain and tilt.

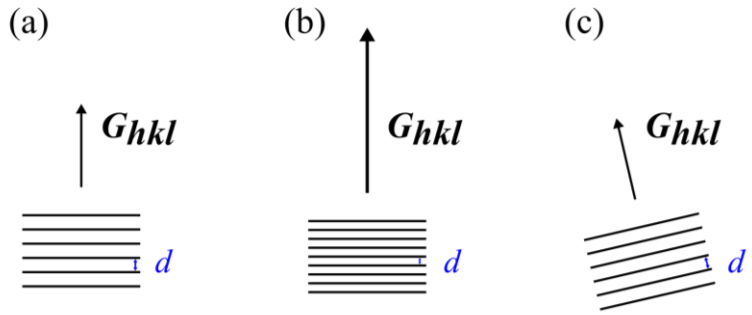

Figure 6 a) A reference lattice and the reciprocal lattice vector b) a compressive strain of the lattice elongates the reciprocal lattice vector and hence moves the position of the Bragg peak in reciprocal space. Tensile strain would instead shorten the reciprocal lattice vector. c) a tilted lattice tilts the reciprocal lattice vector.

For an infinite and perfect crystal in Bragg condition, the Bragg peak from the scattered probe will not have any extension. If the crystal is finite, i.e., if it fits inside the probing illumination, the Bragg peak will have a finite width and fringes. Non-uniform strain is when the displacement changes in the crystal. Non-uniform strain within the footprint of the probe will spread out the Bragg peak. The shape of the crystal will be encoded in the extension of the Bragg peak.

A simulated diffraction peak of a 2D box is illustrated in Fig. 7. The box image in Fig. 7 (a) is multiplied with a plane wave and propagated to the far-field with a Fourier transform. The Fourier transform is normalized to match with the number of photons in a typical nanoprobe (10^9), and Poisson noise is applied to replicate the experimental noise. The resulting simulated diffraction pattern is seen in Fig. 7 (b). The edges of the box give the fringes in the diffraction pattern. From the width of the fringes, the size of the object can be calculated.

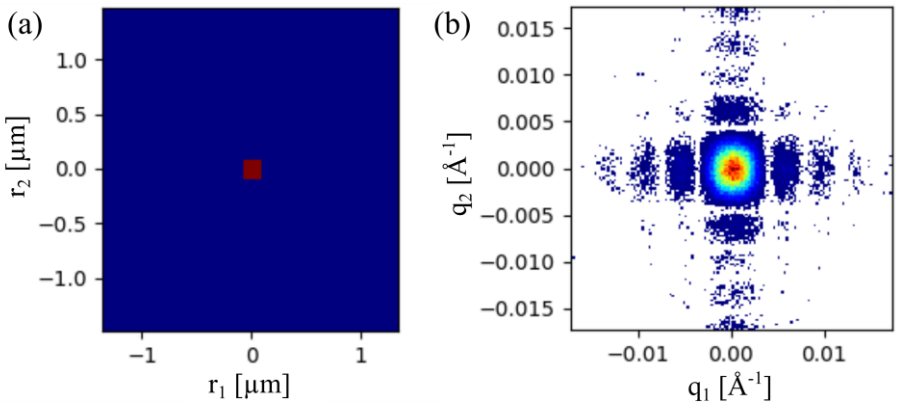

Figure 7 A simulated diffraction pattern from a 170 nm box. In a) the box and in b) the simulated diffraction pattern.

4.2 Scanning X-ray nano-diffraction

4.2.1 Experimental

The principle of a scanning XRD setup is sketched in Fig. 8. The nanofocused probe is scanned over the sample, or equivalently, the sample is scanned in the beam. The pixelated detector in the far-field covers two axes in reciprocal space with a resolution determined by the detector pixel size. The third axis is sampled by rotating the sample in small angular steps along the so-called 'rocking curve'. The curve is in the range of a few degrees to sample a single Bragg peak. This gives the third axis in reciprocal space, with a pixel size determined by the angular step size.

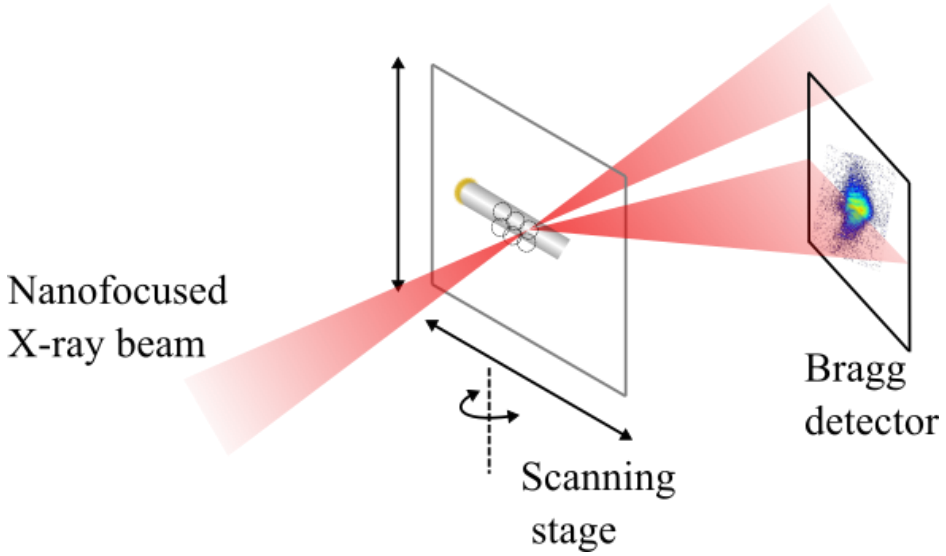

Figure 8 X-ray scanning diffraction measurement setup. The sample is put in the focus of a nanofocused X-ray beam. In the far-field, there is a pixelated detector at the Bragg diffracted beam. A number of lateral scanning positions are indicated on the sample.

4.2.2 Scanning X-ray nano-diffraction of NWs

Previously, ensembles of nanocrystals could be studied with X-ray diffraction [31, 32]. Ensemble data gives statistics on collections of crystals grown on the same sample, such as crystal structure and morphology, but little information about variation between or within single nanostructures. With the recent development in nanoscale focusing of synchrotron X-ray beams, it is possible to measure single NWs [17] and furter, to resolve variations inside nanostructures by scanning the X-ray beam over the sample. X-ray nano-diffraction is a popular tool [33] to probe properties also in other materials, e.g.: strain in thin films [34], strain in single grains in polycrystal solar cells [35] and ferroelastic domains in perovskite NWs [36].

Scanning nano-XRD has been used to resolve strain variations in single semiconductor NWs with a relative sensitivity of 10^{-4}-10^{-5} and spatial resolution of 50-100 nm [15, 16]. For heterostructures, scanning nano-XRD has been demonstrated on core-shell NWs [16, 37] and for axial heterostructures in paper I and ref. [22]. As mentioned earlier, processing of NWs to form electronic devices such as transistors or solar cells can strain the NW. Strain in NW devices have been investigated with scanning nano-XRD in, for example, ref. [21] and a tunnel field-effect transistor, constructed from an embedded axial NW heterostructure, was mapped with a resolution of 50 nm in ref. [22], performed at MAX IV.

Both experiments in paper I and II were done at MAX IV, which, with the first DLSR design, has a great leap in brilliance compared to other available sources [38]. In paper I, we performed the very first nano-diffraction experiment at NanoMAX and demonstrate high-resolution strain maps of InP segments in an axial heterostructure $Ga_xIn_{1-x}P$ NW, a material of high interest for photovoltaics. In the same measurement, we are probing several InP segments of different lengths and relate the mismatch strain

to segment lengths. Such a structural investigation on segment lengths dependence on strain in axial heterostructured NW has, to the best of our knowledge, not been done before. In paper II, we combined nano-XRD with XRF and electrical measurements of a contacted InP NW. The strain in the NW is resolved at the same time as the band structure is probed with the electrical measurements and the composition with XRF.

A way to circumvent the limitation in spatial resolution has been developed with coherent methods. The displacement field is encoded in the phase of the scattered intensity, but what we measure on the detector is the amplitude and not the phase. With coherent methods, the phase can be retrieved by the use of iterative algorithms [39] by oversampling of diffraction patterns as predicted by Sayre in 1952 ref. [40]. With coherent methods, the resolution is no longer limited by the size of the beam. The typical resolution is 8-10 nm. The drawback with coherent methods is the complexity in the analysis and the higher demands on the experiment.

For extended objects, this coherent method is called ptychography, and in Bragg mode, Bragg ptychography. In ref. [41], the 3D resolved strain was mapped in a single InGaAs NW by means of Bragg projection ptychography, a form of Bragg ptychography. A few other demonstrations of Bragg ptychography has been shown in, for example, ref. [42-44]. In CDI and Bragg CDI, the object is fully enclosed in the beam. The object is less oversampled, but the experiment is simplified. Demonstration of strain imaging in NWs is demonstrated in, for example [45] with multiple reflections and in [19] under applied voltage.

5 Scanning XRD of GaInP-InP nanowires

$Ga_xIn_{1-x}P$ is a promising material for NW-based photovoltaics and light-emitting devices, as its bandgap can be adjusted from the near-infrared region to the middle of the visible spectra. The bandgap is tuned by changing the relative amount of Ga and In. In the range $x < 0.74$, it has a direct bandgap which is beneficial for photovoltaics. The composition gradient of $Ga_xIn_{1-x}P$ NW was previously studied with XRD as an ensemble [31]. In paper I, we investigated the strain distribution within a single NW with scanning XRD. We study a $Ga_xIn_{1-x}P$ NW with 5 InP segments of different lengths. We measure how the strain changes depending on segment length and find that it strongly affects both the average strain and the strain distribution.

In this chapter, we first briefly describe the manufacturing and the structure of these types of NWs. Then follows a description of the experimental setup and how the scanning XRD measurements were done. Next, a model of the heterostructure as an elastic strain problem solved with a finite element modelling (FEM) in the software COMSOL is demonstrated. The chapter ends with the experimental results and a comparison with the FEM model.

5.1 InP-InGaP nanowire samples

The NWs in this experiment are around 170 nm in diameter and 2-3 um long. They are axial heterostructures with five segments of InP in a GaInP NW, see Fig. 9. The average amount of Ga in the GaInP is x = 21%. The InP and GaInP lattice constants are a_{InP} = 5.8687 Å and $a_{Ga_{0.21}In_{0.79}P}$ = 5.7809 Å, which amounts to a lattice mismatch of ε = 1.5%.

The nanowires are grown from gold seed particles with vapour-liquid solid growth, see the as-grown NWs in a scanning electron microscopy (SEM) image in Fig. 9(a). This is a technique to produce III-V nanostructures, where the structure grows layer by layer from a liquid gold droplet. Gold seed particles are placed on a regular grid on a substrate. The gold becomes liquid at the growth temperature. The III-V precursors are injected into the growth chamber in vapor form and crystallize at the interface of the gold droplet. The NWs grow in a zinc blende crystal structure with the (111) crystal planes orthogonal to the long axis. The NWs grow upright, but for the experiment, we want them lying flat on the substrate. In this way, it is possible to measure one isolated NW at a time. From the growing-substrate, some of the NWs were transferred to an empty Si_3N_4 membrane substrate to lie flat in a random fashion.

A high angle annular dark field scanning transmission electron microscopy (HAADF-STEM) image of a single NW from this sample batch is shown in Fig. 9 (c). With this method, the denser InP segments are brighter.

5.2 Experimental setup and measurements

We performed the strain mapping experiment at the NanoMAX beamline at MAX IV in Lund. Before the scanning XRD measurements, the X-ray beam was characterized using ptychography. Ptychography in transmission mode gives high-resolution images of both sample and the beam. This was done on a well-known test sample, a Siemens star, and a pixel detector in transmission. The KB mirror focus size was 90 nm, with an energy of 9.49 keV and a flux of 10^9 photons/s.

Using optical microscopes at the beamlines' experimental station, the Si_3Ni_4 substrate was positioned in the X-ray beam using the sample stage motors. A single NW is difficult to see in the optical microscope, so it was aligned in the beam focus using the In and Au signal from an XRF detector. We made sure that the NW was in the centre of rotation of the sample stage so that it did not go out of focus when rotated. The NW was then rotated to the long axis (111) Bragg condition with approximate InP Bragg angle, 8°, and the rotation angle was fine-tuned by searching for the diffracted signal on a pixel detector at angle 2θ, Fig. 9 (e). The Bragg detector was put at a distance far away enough to be in the far-field and close enough to receive a strong signal with both the InP and the GaInP visible on the detector. Due to the smaller lattice constant, the GaInP segments scatter at a higher angle, see Fig. 9 (d).

This concluded the preparations for the strain mapping measurement. For the strain mapping, we scanned the NW with 2D scans while measuring the diffraction. We rotated the sample stage 51 times in steps of 0.02 degrees and repeated the scanning for each rotation. In this way, we measured a 3D Bragg peak in the far-field at each measurement point. The detector in transmission simultaneously captured the transmitted signal from the NW. From that signal, we could track the real-space position of the NW for each rotation.

The measurements were taken in fly-scanning mode, which means that the detector images are taken while the sample is moving. The piezo-electric stage moves the sample at a constant speed, and the detector is triggered with a certain frequency. In this way, the 'dead time' of the detector, the time it takes for the motors to start and stop, is removed. The measurements can be made much faster but at the cost of a blurring effect of the frames. On the other hand, it could be advantageous for the sample position stability not to let the piezo motors stop and restart. A single frame was taken during the acquisition time of 0.12 s.

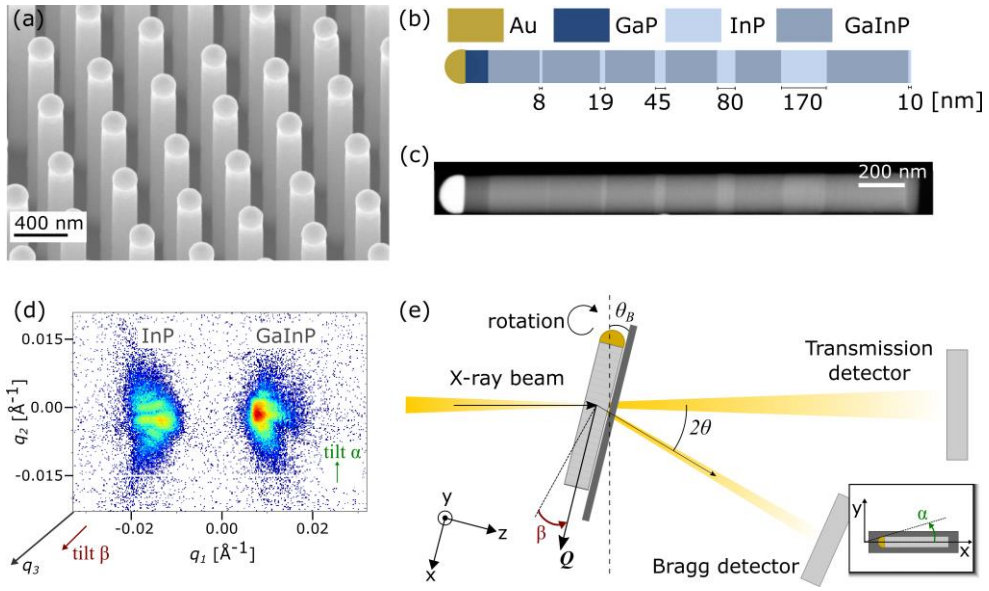

Figure 9 (a) The NWs as-grown vertically from the substrate, shown in a SEM image. (b) Sketch of the NW. (c) HAADF-STEM image of a NW from this sample batch. (d) An example of diffraction from a set of measurement points The InP and GaInP Bragg peaks were captured simultaneously on the Bragg detector. The InP has a higher lattice constant and appears at a lower Bragg angle than GaInP. (e) The measurement geometry. The inset shows the lattice tilt α. Figure from paper I.

5.3 Strain mapping analysis

In short, the strain mapping analysis tracks the position of a Bragg peak in 3D reciprocal space. If the lattice is contracted or stretched at a point on the NW, the scattering vector $\boldsymbol{Q}$ is stretched or contracted. That will be seen as a movement on the detector, mainly along the q_1 axis, see Fig. 9 (d). If the lattice is tilted, the angle of $\boldsymbol{Q}$ will change. The analysis was performed for the InP and GaInP Bragg peaks, separated by using a region of interest on the detector frames.

When looking at the transmission data from each 2D scan, we saw that there was systematic and unsystematic drift of the sample between rotations. These drifts were compensated for when putting together the 3D volumes of diffraction data. With that, some of the measurement frames were discarded, and only the three largest InP segments, with surrounding GaInP maps, are included in the strain maps.

Each point in the 2D scan sampled a slice of a 3D Bragg peak. The slices are not normal to *z*, but at angle θ. That means that the measurement coordinate system (q_1, q_2, q_3), Fig. 9 (a), is not orthogonal but skewed. In the analysis, the 2D slices were out together to 3D and then converted to a Cartesian coordinate system. For each 3D data volume, we calculate the centre of mass (COM). The voxel (3D pixel) in the COM is translated to a coordinate in reciprocal space.

The lattice constant *a* was calculated from the length of the ***Q***-vector. The strain maps were calculated as the change in lattice constant compared with the mean value in the map, $\langle a \rangle$: $\epsilon_{axial} = (a - \langle a \rangle)/\langle a \rangle$. The lattice tilts were calculated from the ***Q***-vector as

$$\alpha = \sin^{-1} \frac{q_y}{|\boldsymbol{Q}|} \tag{19}$$

and

$$\beta = \tan^{-1} \frac{q_x}{q_z} \tag{20}$$

5.4 FEM simulations in COMSOL

We wanted to confirm the results from the experiment and help explain the features with a simulation. To do this, we set up a linear elasticity 3D model in the software COMSOL Multiphysics. In short, COMSOL can solve problems that are governed by partial differential equations using FEM. We employed the COMSOL module 'solid mechanics', which can simulate deformation, stress and strain in solids. With FEM, the problem is solved by dividing up the 3D body into "finite elements". The problem becomes a set of differential equations to be solved for each element, with the requirement that the solution is continuous between elements. We modelled the displacement field in a heterostructure NW from initial mismatch strain, as a linear elasticity problem, as discussed in Chap. 4.1.2. Next, I will discuss some of the practical aspects of implementing the model in COMSOL.

In COMSOL, the geometry of the 3D NW with its segments was set up, and each segment was attributed with its material. Here, the materials are defined by their properties: Density, Young's modulus, and Poisson ratio, which were taken from ref. [46]. The NW is defined to be isotropic, which means that the approximation that its physical properties, such as the ones just listed, do not depend on the direction. The FEM grid was automatically generated by COMSOL and had typical element lengths of about one nanometer. To achieve a converging solution, the 3D body cannot be defined to be anywhere in space, so a boundary condition that one of the ends of the NW was fixed was employed.

Zooming in on a single InP segment in the NW, then we have a InP segment sandwiched between two GaInP segments. We define the initial strain in COMSOL from the lattice constants a_{InP} and a_{InGaP} with Eq. 20. The InP segment has a larger lattice constant than the GaInP segments, so the initial strain is positive. To calculate the lattice constant for GaInP, we used *Vegard's law* used for composite materials:

$$a_{A_{1-x}B_x} = (1 - x)a_A + xa_B \tag{21}$$

where *x* is the amount of material *B* in % in the composite material made up of *A* and *B*.

5.4.1 Diffraction images from simulated displacements

There are a few further steps between the ideal FEM simulations and the strain maps. It can be beneficial to go through each step with ideal simulated data, which makes it easier to discover errors and mistakes. Furthermore, the numerical calculation of the strain maps involves a few approximations. Following the same procedure for the simulated data as the experimental, the same approximations are made equivalently for the experimental and simulated strain maps.

The output from the COMSOL simulation is the displacement field **u**(**r**) at a set of data points, defined by the COMSOL object mesh. This mesh is a non-regular pattern that is unsuitable for the discrete fast Fourier transforms (FFT) needed for the diffraction simulations. Therefore, these data points were interpolated on a regular object grid that was defined to replicate the measurement. The field of view (FOV) in reciprocal space for each measurement point is defined by the number of pixels on the detector that is used for analysis, the detector pixel size, the energy of the X-ray beam, and the distance to the detector. Adding the FOV to each measurement point gives the full measurement grid.

The X-ray beam profile was taken from the ptychographic measurement and extruded to 3D. With a nano-focused probe, the diffraction pattern in the far-field depends on both the probe profile and the object; this is further discussed in paper I. The product of the 3D probe and 3D object was propagated to the far-field with a 3D FFT. Next, we added Poisson noise to replicate the measured data. At this point, we had 3D diffraction patterns that replicated the measured diffraction data, and the strain mapping procedure was performed in the same way as for the measured data.

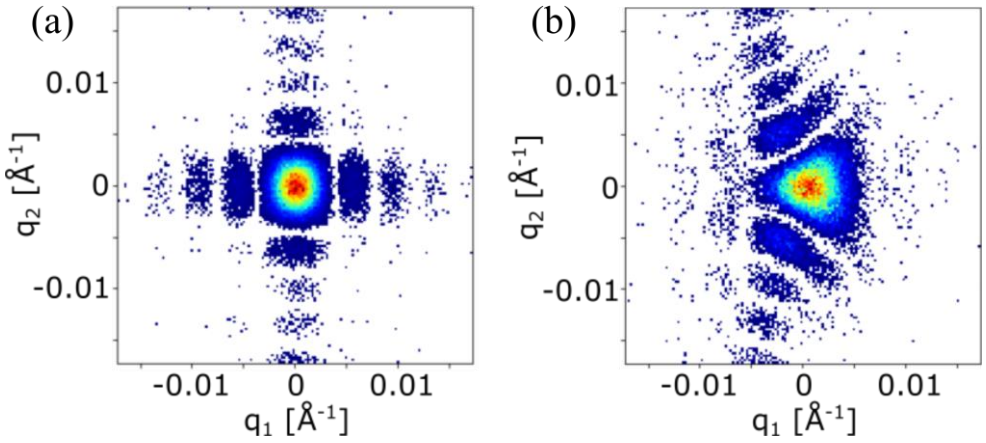

Figure 10 A 2D cut of a simulated Bragg peak from a 2D box. In a) Bragg peak from an unstrained segment b) Bragg peak from a segment strained by lattice mismatch.

The effect of strain on a diffraction pattern is illustrated with a simulation in Fig. 10. In this illustration, the illumination has been simplified to a plane wave. Fig. 7 (a) displays the FFT of a 2D box illustrating how diffraction from an isolated InP segment that is thus unstrained would look. In Fig. 10 (b), is the FFT of a 2D box with strain, illustrating a segment in the NW strained by the lattice mismatch. The diffraction peak becomes bent to an arc shape. This shape is also found in the experimental data, see Fig. 9 (d). The angle of the bending follows the strength of the strain field. For a stronger strain field, the bending angle is increased. The bending direction depends on the sign of the strain field, i.e., if it is tensile or compressive. This is why, in Fig. 9 (d), the InP and InGaP are bent in different directions.

5.5 Results and discussion

Fig. 11 (a) shows the results of the experimental strain mapping, with the InP results (left) and the GaInP results (right). The top maps show the total scattered intensity on the Bragg detector in each measurement point on the 2D grid. The beam is 90 nm, but that is the full width half maximum. The probe has tails away from the centre, which is why we observe some scattered intensity outside the segments. From the axial strain maps, we observe a relative difference in strain, on average, 1.5% between the InP and the GaInP. Furthermore, we can resolve differences within each segment as well

as strain gradients along the NW. Overall, we can observe variations in strain as small as 10^{-4}. In Fig. 11 (b), the corresponding simulated strain maps are displayed.

As GaInP has a smaller lattice constant than InP, we expect the radial strain in the InP segments to be compressive, and therefore the measured axial strain to be tensile (expansive). What we measure is a bit more complex. For the 170 nm segment, we see tensile strain close to the interfaces but also a sign-shift to compressive strain in the centre. That the lattice mismatch is relaxed mostly at the surface is confirmed with the FEM simulations and has also been previously theoretically predicted, as well as a sign-shift to compressive strain in the centre.

The range of strain is larger in the GaInP map, 0.42%, than in the InP map, 0.14%. The larger strain variation in GaInP is most likely due to a gradient in composition, x, with more Ga close to the Au particle. This has been previously reported [47, 48] and is due to conditions in the growing process. From the measured lattice constants and Vigard's law, we calculate that the composition changes from x=19% to x=23%, in agreement with previous scanning XRF measurements [47].

The strain increases with decreasing segment length so that the smallest segment has the same lattice constant as GaInP almost throughout. Since we measured a gradient in Ga composition between the GaInP segments, it is hard to distinguish that effect on the strain difference between InP segments from the changes from segment lengths. Here, we take help from the simulations for the interpretation. We find a similar view of the difference in strain between the InP segments. Since the composition gradient is not included in the simulation, this implies that the difference we see in the measurement is coming from segment lengths.

We observe axial asymmetry in the strain in the InP segments, where the strain minima are shifted to the right of the centre, compared to simulations. Within the GaInP segments, the maximum relative strains are shifted to the left (reversed compared to the overall gradient). In comparison to the simulation, we attribute this to the Ga gradient over the GaInP segments.

The lattice tilts α shows a cross-shaped profile in each segment. The signs and magnitude of α match between the InP and GaInP segments. The result is very similar to the simulated result. We observe no overall gradient in alpha, which means that the NW is straight and not curved in the substrate plane. If it was curved, the simulated map would not be as similar. The beta maps show a change from negative to positive and back to negative, which would correspond to a slight arc shape of the NW, pointing out from the substrate. There are higher insecurities in these maps since it is along the rotation axis; it is less sampled in the measurement.

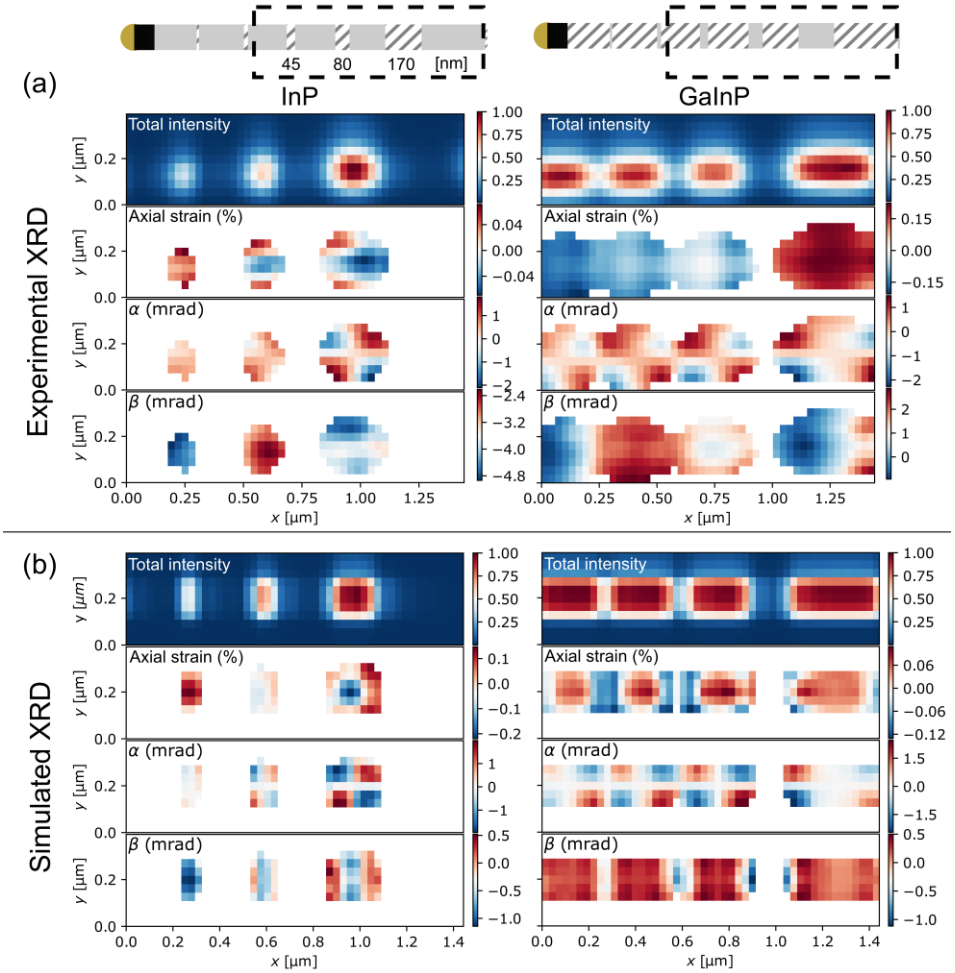

Figure 11 Experimental and simulated strain mapping of a single axial heterostructure with the InP analysis to the left and the GaInP to the right. (a) Experimental strain maps. From top to bottom: total scattered intensity in Bragg, axial strain, in-plane tilt, α, out of plane tilt, β. (b) the corresponding maps for simulated data. Figure from paper I.

6 Multimode X-ray measurements at the NanoMAX beamline

X-rays are non-invasive and highly penetrable, and several complementary techniques can be measured at once. In paper II, we demonstrate a multimode setup at the NanoMAX beamline to investigate compositions, morphology, crystal structure and electrical response of a NW device. With an XRF detector close to the sample, a pixelated detector in Bragg condition and one in transmission, three X-ray techniques are collected in one measurement: XRF, scanning transmission X-ray microscopy (STXM) and scanning XRD. By connecting the NW device to an amperemeter and voltage source, a fourth technique, X-ray beam induced current (XBIC), is included. The setup is tested on a InP NW device. In this chapter, I will briefly explain the function of the device and go through the techniques that were used to investigate it. Then I will summarize the experiment and the results, focusing on the scanning XRD and the resulting strain maps.

6.1 Four complimentary X-ray techniques

While the scanning XRD technique is discussed thoroughly throughout the thesis, the other three techniques deserve a little more discussion. To understand the usefulness of the XBIC, a little background on solar cell nanowire devices is necessary.

The InP NW device is p-i-n doped, which means it is a pn-junction with an extra wide i-region, or *depletion region*. That makes it suitable for use as a solar cell device. When photons are absorbed in the depletion region, an electron-hole pair is created, and the internal electric field of the depletion region drives the hole and electron to opposite directions, resulting in a current in one direction. XBIC is a technique that can measure the response to light in the depletion region by using X-rays as a light source. The number of electron-hole pairs that are created, and where they are created, can be established. Similar techniques exist that use other probes, i.e., electrons and laser light. The advantages with X-rays are that they have higher penetration length, they can be focused, and at a synchrotron beamline there are possibilities to vary the intensity and energy. A thorough description of the use of XBIC as a measure of the electrical qualities of a NW device can be found in ref. [49].

The XRF signal is a spectrum where each peak corresponds to an atomic transition. The energy of the transition is a signature of the element it is originating from. By measuring the XRF signal while scanning the device with a nanofocused beam, the variations in composition can be mapped out as an XRF image, by selecting the peak of interest from the spectrum. If peaks from different emissions overlap, they need to be separated by peak fitting. It is also possible to get the absolute concentrations of elements if the XRF peaks are examined thoroughly [47]. This can both be done using software for XRF peak fitting, such as PyMca.

The STXM signal is the transmitted beam taken after absorption of the sample. Different modes can be extracted from this signal to enhance the contrast. The total transmitted signal is often called the *bright field*, while the deflected beam is called *dark field*. A third contrast mode, the differential phase contrast (DPC), can be found by looking at gradients in the image. The dark field and DPC show gradients in the sample that deflect the beam, such as thickness variation.

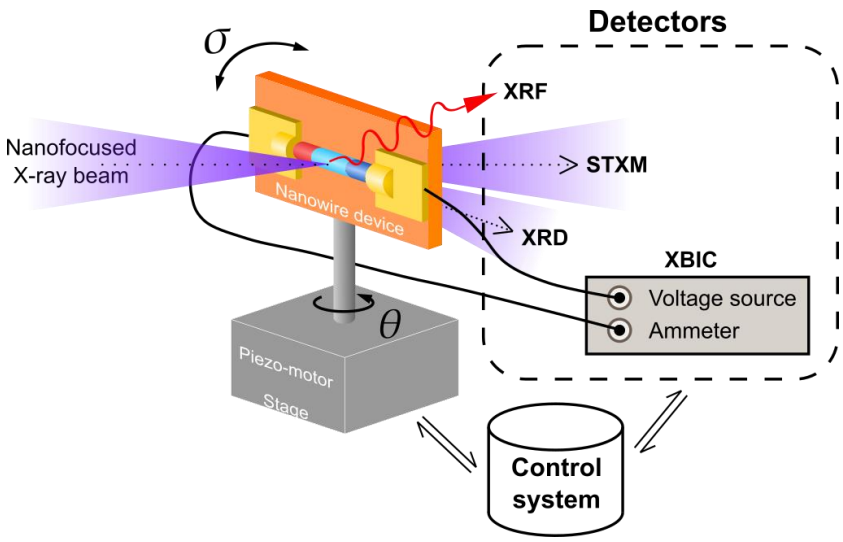

Figure 12 Multimode setup for simultaneously measuring XRF, STXM, scanning XRD and XBIC with a nanofocused probe at the NanoMAX beamline. The sample stage is on a piezo motor that can translate the sample vertically and horizontally. The sample is a contacted InP NW device that is contacted to a voltage source in one end and an ammeter in the other. The voltage source can be used to apply a bias over the device. [Figure from paper II]

6.2 Experimental setup and measurements

This multimode setup was developed at the NanoMAX beamline at MAX IV. The energy of the X-ray beam was 15 keV, and it was focused with a KB-mirror setup to 50 nm. The NW was scanned by moving the sample stage on a 2D grid with 50 nm steps using piezo-electric motors; see the setup in Fig. 12. To reduce the overhead time, the measurement was taken in fly-scanning mode, that is, the detectors were triggered at fixed acquisition time while the *x*-motor was moving continuously. This results in a blurring of the images in *x*, but on the other hand, sample drift due to the settling of the piezo motors is reduced.

For the scanning XRD measurement, another NW was found on the sample and rotated so that the Bragg peak of InP was in line with the XRD detector. We repeated the 2D scanning for 51 angles around the Bragg peak, separated by 0.02 degrees, similar to paper I. The STXM, XRF and XBIC signals were collected simultaneously. In the analysis, the XRF maps were used to compensate for a small drift between the rotations. Next, a 3D reciprocal diffraction was put together for each scanning position. The position of the Bragg peak was found with reciprocal space mapping by calculating the centre of mass of the Bragg peak in each scanning position. A more thorough discussion about strain mapping analysis is discussed in Chapter 5.

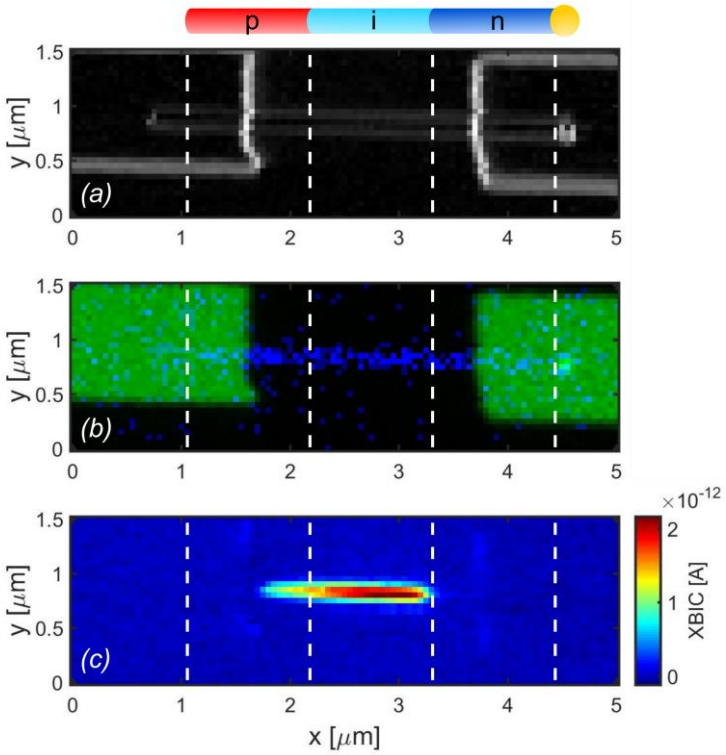

Figure 13 A demonstration of the multimode setup using three techniques. A sketch of the NW is shown on top, and the three regions of the NW are indicated with white dashed lines in each map. (a) STXM data with DPC analysis with the edges of the contacts and the contours of the NW clearly visible. (b) XRF map with the contacts visible in the Au signal (green) and the NW identified with the In signal (blue). (c) XBIC signal. The signal is coming from the depletion region in the p-i-n junction. [Figure from paper II]

6.3 Results and discussion

The STXM, XRF and XBIC signal from a NW can be seen in Fig. 13 with 50 nm resolution. The XBIC signal in Fig. 13 (c) shows a signal originating in the depletion region. The exact origin can be found by looking at the other two maps. In Fig. 13 (a), the contact edges and the NW can be seen, with stronger contrast in the NW edge coming from the gold seed particle. In the XRF map, Fig. 13 (b), the signal from the contacts is coming from gold emission, and the signal from the NW is coming from indium. The position of the XBIC signal can be measured from the gold particle in the XRF map.

The XBIC signal shows the current coming from excitations induced by the X-rays. By measuring the XBIC current, the number of charge carriers generated by the X-ray beam was calculated. The asymmetry in the signal is due to an asymmetry in the doping profile [50].

The scanning XRD measurement was done on a similar NW, see Fig. 14. The contacts are visible in blue and the NW in green in the XRF map, Fig. 14 (a). The summed intensity in each scanning position is shown in Fig. 14 (b), corresponding to a STXM map in Bragg mode. There is a gap in intensity in the left half of the NW since the angular range was not enough to capture the signal in that area due to the bending of the NW explained further below.

The NW is strained in a range of about 0.1%. The NW is not a heterostructure as in the previous chapter but is strained by the contacts so that the lattice is compressed at the edges under the contacts and stretched in the areas in between. Variations in strain as small as 0.01% (10^{-4}) were observed.

With this analysis, we can observe the tilts of the NW, Fig. 14 (d-e), which gives the complete picture of the NW morphology. The tilt β, shows that the NW is bent in an arc pointing up from the substrate, in the area between the contacts. This has been previously shown in simulations to be caused by the contacts holding down the edges [19] and reported from other experiments [21]. A smaller bending is

seen in the substrate plane, α, in Fig. 14 (d). The observation from the tilts, that the contacts have affected the NW lattice, help explain the features in the strain map.

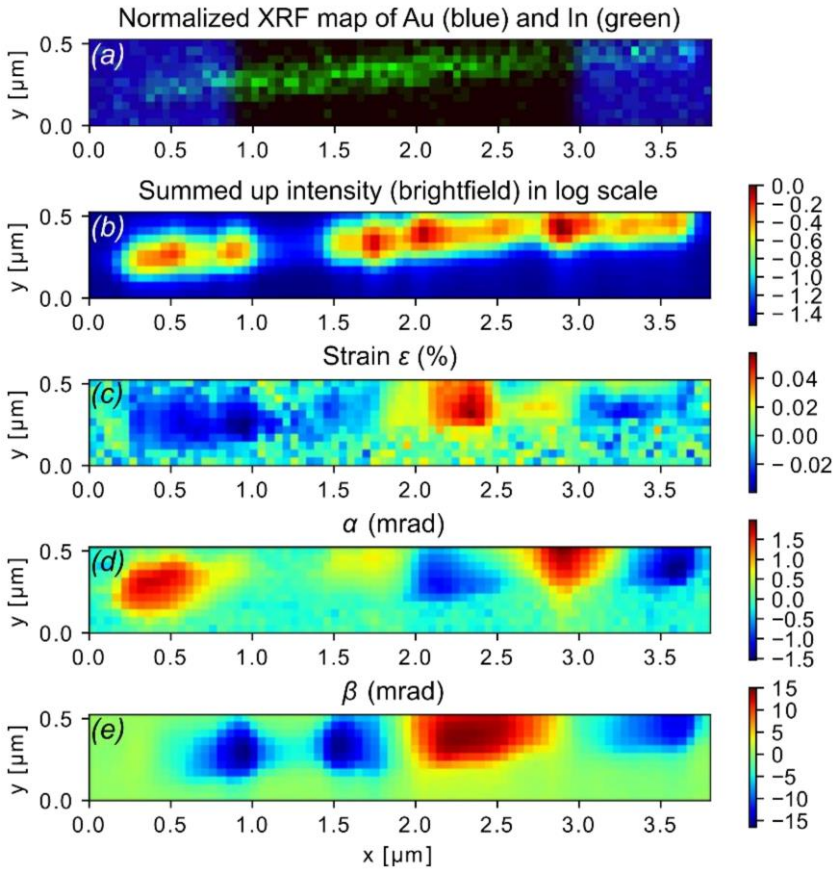

Figure 14 Scanning XRD and XRF from a contacted InP NW, similar to the one in Fig. 12. (a) XRF map with the contacts visible in the Au signal (blue) and the NW in the In signal (green) (b) the summed up intensity in each position on the 2D grid. The gap in intensity between *x* 1.0 and 1.5 µm originates from that the NW was bend and the measurement range was too narrow to fit the complete angular range (c) Strain map of the diffracted InP signal. (d) The crystal lattice tilts around the optical axis, *α*. (e) The lattice tilt around the vertical axis, *β*.

7 Conclusions and outlook

In this thesis, we have used scanning X-ray diffraction to produce high resolution strain maps of nanowire axial heterostructure and a contacted device, performed at the first diffraction limited storage ring, MAX IV. We performed the first scanning diffraction experiment at the NanoMAX beamline as a part of commissioning of the beamline.

In paper I, we obtained strain maps with 90 nm resolution and 10^{-4} relative strain resolution. We saw that the strain distribution changed as a function of heterostructure segment length. The largest segment showed a complex structure that differs significantly from bulk, as it relaxes more at the surface than the center. Furthermore, in paper I, we saw how the model in COMSOL was sufficient to recreate the strain distribution from a lattice mismatch in a heterostructure. When discussing the results, we greatly benefited from making comparisons to the model. The comparison was made more straightforward because we simulated the whole experiment, including using the probe from the experiment and decreasing the resolution to produce the strain maps.

In paper II, we used scanning diffraction as a part of the characterization of a contacted NW device, together with XRF and XBIC. We saw that the contacts strained the NW in an expected way. The setup can be used for any sort of NW device and with applied voltages which enables future devices to be characterized.

There are a lot of parameters to optimize in a scanning X-ray diffraction measurement. A balance between measuring time on one hand and beam damage and sample drift on the other needs to be found. A number of parameters determine the total measurement time: acquisition time, the number of scanning positions, and the number of angles on the rocking curve. In turn, these parameters will depend on energy, the focus size, the flux of the X-ray beam, and the position of the detector. We used a fly-scanning mode which blurs the image but gives a faster and more stable measurement. We chose the detector distance, detector position and the number of angles so that both GaInP and InP Bragg peaks could be sampled in the same measurement.

A straightforward way to improve resolution is to decrease the focus size of the X-ray; the current state of the art is 10 nm or slightly below. The ultimate limitation here is the diffraction limit, which is less than 0.1 nm. As an alternative route, one can make use of the high coherence of a synchrotron beam and get sub-beam resolution with phase retrieval methods. Here, the phase of the diffracted signal is retrieved with iterate algorithms, resulting in sub-beam resolution also resolved in 3D. This was further discussed in chapter 4. To determine whether to go for scanning XRD or coherent methods depends on the demand of resolution, which is weighed against more advanced analysis.

To conclude, we have demonstrated that scanning X-ray diffraction work as a tool to characterize strain in axial nanowire heterostructures. It is a flexible tool that works with a variety of setups and sample environments. We have demonstrated that scanning XRD can be combined with XBIC for strain mapping along with electric characterization. Furthermore, FEM simulations from an elastic model can work as a model for an axial heterostructure.

8 References

1. Haverkort, J.E.M., E.C. Garnett, and E.P.A.M. Bakkers, *Fundamentals of the nanowire solar cell: Optimization of the open circuit voltage.* Applied Physics Reviews, 2018. **5**(3): p. 031106.
2. Otnes, G. and M.T. Borgström, *Towards high efficiency nanowire solar cells.* Nano Today, 2017. **12**: p. 31-45.
3. Wallentin, J., et al., *InP Nanowire Array Solar Cells Achieving 13.8% Efficiency by Exceeding the Ray Optics Limit.* Science, 2013. **339**(6123): p. 1057.
4. Gudiksen, M.S., et al., *Growth of nanowire superlattice structures for nanoscale photonics and electronics.* Nature, 2002. **415**: p. 617.
5. Gibson, S.J., et al., *Tapered InP nanowire arrays for efficient broadband high-speed single-photon detection.* Nature nanotechnology, 2019. **14**(5): p. 473.
6. Barrigón, E., et al., *Synthesis and Applications of III–V Nanowires.* Chemical Reviews, 2019. **119**(15): p. 9170-9220.
7. Motohisa, J., et al., *Characterization of nanowire light-emitting diodes grown by selective-area metal-organic vapor-phase epitaxy.* Nanotechnology, 2019. **30**(13): p. 134002.
8. Memisevic, E., et al., *Individual Defects in InAs/InGaAsSb/GaSb Nanowire Tunnel Field-Effect Transistors Operating below 60 mV/decade.* Nano Letters, 2017. **17**(7): p. 4373-4380.
9. Tomioka, K., M. Yoshimura, and T. Fukui, *A III–V nanowire channel on silicon for high-performance vertical transistors.* Nature, 2012. **488**: p. 189.
10. Jia, C., et al., *Nanowire electronics: From nanoscale to macroscale.* Chemical reviews, 2019. **119**(15): p. 9074-9135.
11. Glas, F., *Critical dimensions for the plastic relaxation of strained axial heterostructures in free-standing nanowires.* Physical Review B, 2006. **74**(12): p. 121302.
12. Otnes, G., et al., *Understanding InP Nanowire Array Solar Cell Performance by Nanoprobe-Enabled Single Nanowire Measurements.* Nano Letters, 2018. **18**(5): p. 3038-3046.
13. Schropp, A., et al., *Hard x-ray scanning microscopy with coherent radiation: Beyond the resolution of conventional x-ray microscopes.* Applied Physics Letters, 2012. **100**(25): p. 253112.
14. Döring, F., et al., *Sub-5 nm hard x-ray point focusing by a combined Kirkpatrick-Baez mirror and multilayer zone plate.* Optics Express, 2013. **21**(16): p. 19311-19323.
15. Schülli, T.U. and S.J. Leake, *X-ray nanobeam diffraction imaging of materials.* Current Opinion in Solid State and Materials Science, 2018.
16. Stankevič, T., et al., *Fast Strain Mapping of Nanowire Light-Emitting Diodes Using Nanofocused X-ray Beams.* ACS Nano, 2015. **9**(7): p. 6978-6984.
17. Biermanns, A., et al., *Structural polytypism and residual strain in GaAs nanowires grown on Si(111) probed by single-nanowire X-ray diffraction.* Journal of Applied Crystallography, 2012. **45**(2): p. 239-244.
18. Keplinger, M., et al., *X-ray diffraction strain analysis of a single axial InAs 1-x Px nanowire segment.* J Synchrotron Radiat, 2015. **22**(1): p. 59-66.
19. Lazarev, S., et al., *Structural Changes in a Single GaN Nanowire under Applied Voltage Bias.* Nano Lett, 2018.
20. Hrauda, N., et al., *X-ray Nanodiffraction on a Single SiGe Quantum Dot inside a Functioning Field-Effect Transistor.* Nano Letters, 2011. **11**(7): p. 2875-2880.
21. Wallentin, J., M. Osterhoff, and T. Salditt, *In Operando X-Ray Nanodiffraction Reveals Electrically Induced Bending and Lattice Contraction in a Single Nanowire Device.* Advanced Materials, 2016. **28**(9): p. 1788-1792.
22. Dzhigaev, D., et al., *Strain mapping inside an individual processed vertical nanowire transistor using scanning X-ray nanodiffraction.* Nanoscale, 2020. **12**(27): p. 14487-14493.

23. Vogt, U., et al. *First x-ray nanoimaging experiments at NanoMAX*. in *SPIE Optical Engineering + Applications*. 2017. SPIE.
24. Johansson, U., et al., *NanoMAX: the hard X-ray nanoprobe beamline at the MAX IV Laboratory.* Journal of Synchrotron Radiation, 2021. **28**(6).
25. Hermanns, C.F., *X-ray absorption studies of metalloporphyrin molecules on surfaces: Electronic interactions, magnetic coupling, and chemical switches*. 2013.
26. Hubbell, J.H., H.A. Gimm, and I. O/verbo/, *Pair, triplet, and total atomic cross sections (and mass attenuation coefficients) for 1 MeV-100 GeV photons in elements Z= 1 to 100.* Journal of physical and chemical reference data, 1980. **9**(4): p. 1023-1148.
27. Kittel, C., P. McEuen, and P. McEuen, *Introduction to solid state physics*. Vol. 8. 1996: Wiley New York.
28. Als-Nielsen, J. and D. McMorrow, *Elements of modern X-ray physics*. 2011: John Wiley & Sons.
29. Kirkpatrick, P. and A.V. Baez, *Formation of optical images by X-rays.* JOSA, 1948. **38**(9): p. 766-774.
30. Paganin, D., *Coherent X-ray optics*. 2006: Oxford University Press on Demand.
31. Kriegner, D., et al., *Structural investigation of GaInP nanowires using X-ray diffraction.* Thin Solid Films, 2013. **543**: p. 100-105.
32. Mandl, B., et al., *Au-free epitaxial growth of InAs nanowires.* Nano letters, 2006. **6**(8): p. 1817-1821.
33. Chahine, G.A., et al., *Imaging of strain and lattice orientation by quick scanning X-ray microscopy combined with three-dimensional reciprocal space mapping.* Journal of Applied Crystallography, 2014. **47**(2): p. 762-769.
34. Spolenak, R., et al., *Local plasticity of Al thin films as revealed by X-ray microdiffraction.* Physical review letters, 2003. **90**(9): p. 096102.
35. Schäfer, N., et al., *Microstrain distributions in polycrystalline thin films measured by X-ray microdiffraction.* Journal of Applied Crystallography, 2016. **49**(2): p. 632-635.
36. Marçal, L.A., et al., *In situ imaging of ferroelastic domain dynamics in CsPbBr3 perovskite nanowires by nanofocused scanning x-ray diffraction.* ACS nano, 2020. **14**(11): p. 15973-15982.
37. Krause, T., et al., *Nanofocus x-ray diffraction and cathodoluminescence investigations into individual core–shell (In,Ga)N/GaN rod light-emitting diodes.* Nanotechnology, 2016. **27**(32): p. 325707.
38. Eriksson, M., J.F. van der Veen, and C. Quitmann, *Diffraction-limited storage rings–a window to the science of tomorrow.* Journal of synchrotron radiation, 2014. **21**(5): p. 837-842.
39. Fienup, J.R., *Phase retrieval algorithms: a comparison.* Applied optics, 1982. **21**(15): p. 2758-2769.
40. Sayre, D., *Some implications of a theorem due to Shannon.* Acta Crystallographica, 1952. **5**(6): p. 843-843.
41. Hill, M.O., Nano Lett., 2018. **18**: p. 811.
42. Godard, P., et al., *Three-dimensional high-resolution quantitative microscopy of extended crystals.* Nature Communications, 2011. **2**: p. 568.
43. Hruszkewycz, S.O., et al., *High-resolution three-dimensional structural microscopy by single-angle Bragg ptychography.* Nat Mater, 2017. **16**(2): p. 244-251.
44. Pateras, A.I., et al., *Nondestructive three-dimensional imaging of crystal strain and rotations in an extended bonded semiconductor heterostructure.* Physical Review B, 2015. **92**(20): p. 205305.
45. Newton, M.C., et al., *Three-dimensional imaging of strain in a single ZnO nanorod.* Nature Materials, 2010. **9**(2): p. 120-124.
46. Ioffe. *Ioffe Institute Physical Properties of Semiconductors Electronic Archive*. May, 2017]; Available from: http://www.ioffe.ru/SVA/NSM/Semicond/index.html.
47. Troian, A., et al., *Nanobeam X-ray Fluorescence Dopant Mapping Reveals Dynamics of in Situ Zn-Doping in Nanowires.* Nano Letters, 2018. **18**(10): p. 6461-6468.
48. Otnes, G., et al., *In x Ga1–x P Nanowire Growth Dynamics Strongly Affected by Doping Using Diethylzinc.* Nano letters, 2017. **17**(2): p. 702-707.
49. Chayanun, L., *Nanowire devices for X-ray detection*. 2020, Lund University.
50. Chayanun, L., et al., *Nanoscale mapping of carrier collection in single nanowire solar cells using X-ray beam induced current.* Journal of Synchrotron Radiation, 2019. **26**(1).

Paper I

Research Article

Nano Research
2020, 13(9): 2460–2468

ISSN 1998-0124 CN 11-5974/O4
https://doi.org/10.1007/s12274-020-2878-6

High resolution strain mapping of a single axially heterostructured nanowire using scanning X-ray diffraction

Susanna Hammarberg[1] (✉), Vilgailė Dagytė[2], Lert Chayanun[1], Megan O. Hill[3], Alexander Wyke[1], Alexander Björling[4], Ulf Johansson[4], Sebastian Kalbfleisch[4], Magnus Heurlin[2], Lincoln J. Lauhon[3], Magnus T. Borgström[2], and Jesper Wallentin[1]

[1] *Synchrotron Radiation Research and NanoLund, Lund University, Box 118, Lund 221 00, Sweden*
[2] *Solid State Physics and NanoLund, Lund University, Box 118, Lund 221 00, Sweden*
[3] *Department of Materials Science and Engineering, Northwestern University, Evanston, Illinois 60208, USA*
[4] *MAX IV Laboratory, Lund University, Box 118, Lund 221 00, Sweden*

© The author(s) 2020

Received: 27 March 2020 / **Revised:** 12 May 2020 / **Accepted:** 13 May 2020

ABSTRACT

Axially heterostructured nanowires are a promising platform for next generation electronic and optoelectronic devices. Reports based on theoretical modeling have predicted more complex strain distributions and increased critical layer thicknesses than in thin films, due to lateral strain relaxation at the surface, but the understanding of the growth and strain distributions in these complex structures is hampered by the lack of high-resolution characterization techniques. Here, we demonstrate strain mapping of an axially segmented GaInP-InP 190 nm diameter nanowire heterostructure using scanning X-ray diffraction. We systematically investigate the strain distribution and lattice tilt in three different segment lengths from 45 to 170 nm, obtaining strain maps with about 10^{-4} relative strain sensitivity. The experiments were performed using the 90 nm diameter nanofocus at the NanoMAX beamline, taking advantage of the high coherent flux from the first diffraction limited storage ring MAX IV. The experimental results are in good agreement with a full simulation of the experiment based on a three-dimensional (3D) finite element model. The largest segments show a complex profile, where the lateral strain relaxation at the surface leads to a dome-shaped strain distribution from the mismatched interfaces, and a change from tensile to compressive strain within a single segment. The lattice tilt maps show a cross-shaped profile with excellent qualitative and quantitative agreement with the simulations. In contrast, the shortest measured InP segment is almost fully adapted to the surrounding GaInP segments.

KEYWORDS

strain mapping, nanowire, heterostructure, X-ray diffraction (XRD), MAX IV, finite element modeling

1 Introduction

Semiconductor heterostructures are crucial building blocks for most modern electronic and optoelectronic devices. As such, extensive research has been devoted to creating tailorable, pristine interfaces between semiconductor thin films. However, this has been limited to low lattice mismatch materials, as large interfacial strain can lead to defect formation and device degradation. Nanowire heterostructures on the other hand have allowed for the creation of new heterostructures, given their high strain tolerance. Nanowires are a class of one-dimensional semiconductor nanostructures that are being developed for electronics [1–3], photovoltaics [4–6], detectors [7], and light emitting devices [8–11], as well as studies of quantum physics [12–16]. In addition to new flexibility in heterostructure material combinations compared with bulk material, the small dimensions of nanowires also result in reduced material usage and high scalability. Nanowire synthesis also has more degrees of freedom than traditional thin film growth, allowing controlled heterostructure formation both axially [17] and radially [18]. Heterostructures in the axial direction are particularly interesting because they can modify the band structure along the natural carrier transport direction, and such nanowires are being explored both for fundamental physics [19] as well as for devices such as multijunction solar cells [20, 21], tunnel diodes [22], tunneling field effect transistors [1], and lasers [23].

Given the presence of lattice mismatched interfaces, it is critical to understand the strain state at nanowire junctions, because the strain can affect the bandgap and the charge carrier mobility as well as induce piezoelectric fields. Furthermore, while the growth of lattice mismatched heterostructures is quite well understood in epitaxial films, nanowire heterostructures are more complex. In thin films, defects form when the layer exceeds a critical thickness, which is generally problematic since they form carrier recombination and scattering centers. Theoretical studies have predicted that the strain at the interface of an axially heterostructured nanowire could be partially accommodated by lateral expansion or compression via the free surfaces [24–26], which means that segments with larger lattice mismatch than predicted for thin films could be grown without defect formation. Simulations based on finite element modelling (FEM) have predicted dome-shaped strain

Address correspondence to susanna.hammarberg@sljus.lu.se

distributions at the interface, with maximum strain at the radial centre of the nanowire [25, 27]. This three-dimensional (3D) strain relaxation becomes comparatively more important in thinner nanowires, and for a given misfit, theoretical calculations predict a critical radius below which infinitely thick layers can be grown defect free [24–26]. However, the theoretical models typically ignore experimentally observed complexities such as nanowire bending [28], phase segregation [29] and interdiffusion [30]. Therefore, quantitative high-resolution strain measurements, combined with theoretical calculations, are vital for fully understanding axial nanowire heterostructures.

Experimental characterization of the strain distribution in axial nanowire heterostructures is challenging, due to the simultaneous requirements of high strain sensitivity and spatial resolution. Transmission electron microscopy (TEM) offers excellent spatial resolution but limited strain sensitivity, and it has therefore been used for studies of axial heterostructures with quite large mismatches [30, 31]. The strong interaction of electron probes with matter also limits TEM to studies of relatively thin nanowires. In comparison, the strain sensitivity of X-ray diffraction (XRD) is excellent, typically significantly better than TEM, and the long absorption length of hard X-rays allows studies of large crystals in a non-destructive manner. Traditionally, XRD has had limited real space resolution due to the difficulty in making high-quality X-ray optics, but development in focusing techniques has given the opportunity to focus a highly coherent hard X-ray beam down to the nanoscale [32, 33]. These improvements have enabled diffraction imaging of single nanocrystal structures to study the strain distribution [34–37], detect defects and dislocations [38], as well as complete devices [39] under applied voltage [40, 41]. Strain mapping of axially heterostructured nanowires with high spatial resolution and strain sensitivity has so far not been demonstrated, to the best of our knowledge, partially because such weakly scattering nanocrystals require an intense X-ray nanofocus. However, a new generation of so-called diffraction limited storage rings (DLSR) have been developed, which offer much higher coherent X-ray fluxes [42] than previous synchrotrons.

Here, we demonstrate high-resolution strain mapping of an axially heterostructured $Ga_xIn_{1-x}P$-InP nanowire using the NanoMAX beamline [43] of the MAX IV facility, the first operational DLSR. $Ga_xIn_{1-x}P$ (hereafter referred to as GaInP) is a promising material for photovoltaics and light emitting devices, as its bandgap can be adjusted from the near-infrared region to the middle of the visible spectra by changing the relative amount of Ga and In. We use scanning XRD with a 90 nm beam to obtain two-dimensional (2D) maps of the strain, with about 10^{-4} relative strain sensitivity, as well as the lattice tilt. We probe the strain distribution at different axial layer thicknesses within a single nanowire and find that the segment length strongly affects both the average strain and the strain distribution. The 3D strain profile of the nanowire heterostructure was simulated using FEM and the experimental data was compared with kinematic scattering simulations based on the FEM result and the measured beam profile. The measurements of the GaInP segments and the longest InP segment verify the theoretically predicted strain distributions, where both materials show similar but mirrored dome-shaped strain profiles with both positive and negative strains within the same segment. In contrast, the shortest investigated InP segment is almost fully homogeneous and adapted to the surrounding GaInP lattice. Our results demonstrate that nanofocused XRD has sufficient strain sensitivity and spatial resolution to measure the strain distribution in axially heterostructured nanowires.

2 Experimental

Nanowires consisting of five InP segments of varied length within a GaInP nanowire were grown in the particle assisted growth mode using metal-organic vapor phase epitaxy (Figs. 1(a) and 1(b)). The Au seed particle array was defined

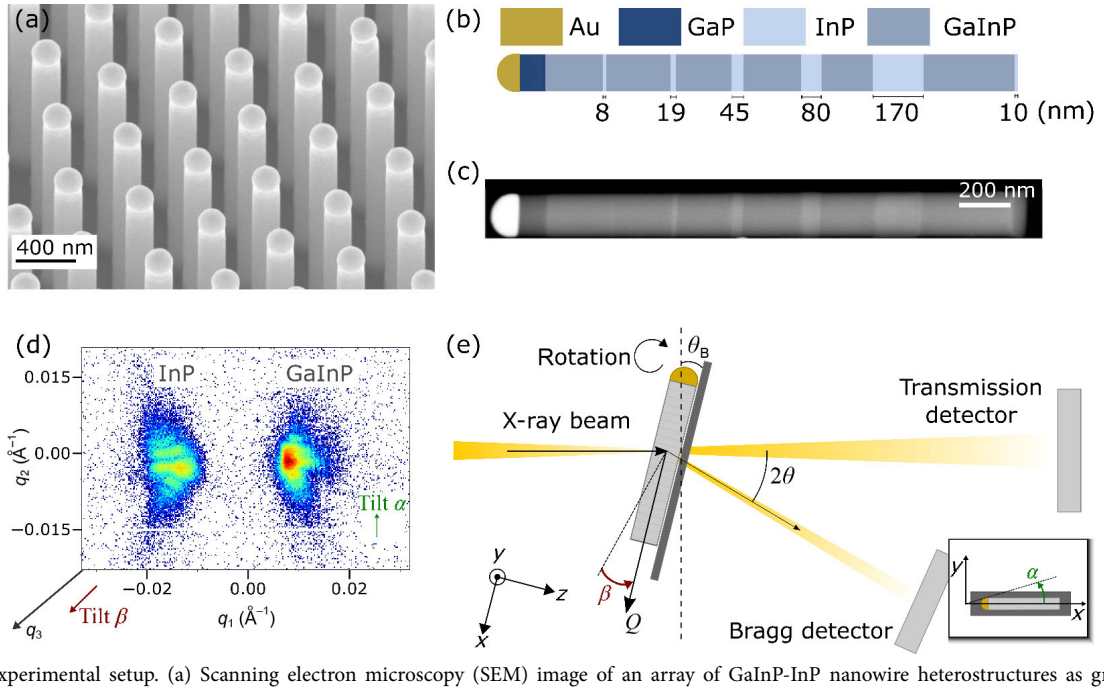

Figure 1 Experimental setup. (a) Scanning electron microscopy (SEM) image of an array of GaInP-InP nanowire heterostructures as grown on the substrate from Au seed particles. The image was taken at a tilt of 30°. (b) Sketch of a single nanowire with approximate InP segment lengths. (c) STEM image of a single nanowire. (d) Example of Bragg diffraction signal from the (111) lattice planes of a single nanowire in the experiment. The signal is the logarithm of the sum of all frames over a rocking curve in a single position on the wire, with the InP peak to the left and the GaInP peak to the right. The detector frames' reciprocal space vectors (q_1, q_2, q_3) directions are indicated. (e) Experimental geometry as viewed from above. The nanowire is lying flat on a Si_3N_4 window. The tilt β is around the same axis as θ. The inset indicates the tilt α, which is a rotation around z.

by nanoimprint lithography, resulting in a hexagonal pattern of Au particles with a pitch of 500 nm [44]. The nanowires show an average radius of about 95 nm, which is slightly above the predicted critical radius for the lattice mismatch [25, 26]. The total length was about 2.2 μm for nanowires from the center of the growth substrate, whereas the nanowire growth rate was higher towards the edges of the substrate. High angle annular dark field scanning transmission electron microscopy (HAADF-STEM) of a single nanowire is shown in Fig. 1(c), where the denser InP segments are brighter, exhibiting a barcode structure. The lengths of each segment, obtained from STEM measurements, were 170, 80, 45, 19, and 8 nm corresponding to segment growth times of 120, 60, 45, 30, and 15 s, respectively. The nanowires grow in the (111)B direction and have a zinc blende crystal structure.

To prepare for nano-XRD, nanowires were mechanically transferred to a Si_3N_4 membrane, lying flat on the surface in random in-plane orientations. We used the Kirkpatrick-Baez (KB) mirror nanofocus at NanoMAX to perform scanning XRD of a single heterostructured nanowire (energy 9.49 keV, flux 10^9 photons/s, focus size 90 nm). The beamline's secondary source aperture slits were adjusted to ensure a coherent illumination incident on the KB-mirrors [45].

We used one 2D detector in transmission to track the real space movement of the sample and for ptychographic probe reconstructions, and a second one for the Bragg diffraction. We collected scanning XRD data sets from the (111) reflection, i.e. with the scattering vector parallel to the nanowire axis, by 2D scanning the sample in focus. A rocking curve was collected by rotating the sample around y in 51 angular steps of 0.02° (see the coordinate system and the scattering geometry as viewed from above in Fig. 1(e)). Between rotations, we tracked and compensated for systematic and unsystematic movements of the nanowire by analyzing the transmission signal, as discussed in the Methods section. We used a fly scanning mode in the horizontal direction to minimize the overhead, by moving the piezo scanner continuously while acquiring 101 frames in a 3 μm range. In the vertical direction, we used a 40 nm step size. The high coherent flux allowed a short acquisition time of 0.12 s per frame, giving a total measurement time of 4 h for the dataset consisting of 96,960 frames. Due to the modest lattice mismatch, we could collect the two peaks of InP and GaInP on the detector simultaneously, see an example of the scattered signal in Fig. 1(d). The complex shape of the Bragg peaks comes from the finite size of the segments and the beam, as well as strain, as discussed further in Section 3.3. For each beam position, we made reciprocal space mapping [46] of the InP and GaInP Bragg peaks and calculated the respective peak positions using the center of mass.

3 Results and discussion

3.1 Strain maps of a nanowire heterostructure

The results from the analysis of the scanning XRD measurements are shown in Fig. 2(a), with the InP to the left and GaInP to the right. Since the two smallest InP segments were out of the measurement range for some of the rotations, the maps include the three largest InP segments and the surrounding GaInP segments only. The upmost maps show the total scattered intensity of the InP and GaInP Bragg peaks in each scanning position. The slightly asymmetric profile of the segments in the maps, with higher intensity above and to the right, comes from a slight asymmetry in the X-ray nanofocusing (Fig. S1(b) in the Electronic Supplementary Material (ESM)). Since the probe profile has tails, no pixel is zero.

The axial strain maps were calculated as the change in lattice constant, a, compared with the mean value in the map, $\langle a \rangle$: $\epsilon_{\text{axial}} = (a - \langle a \rangle)/\langle a \rangle$. We used the high intensity pixels in the intensity maps to determine which pixels to show in the strain maps, for clarity. The ones with low total intensity in the scattering signal were set to zero. The average relative difference in lattice constant between the InP and GaInP maps is 1.5%. The total range of measured strain is about 0.14% and 0.42% for the InP and GaInP segments, respectively. We can observe strain variations of less than 0.01%, i.e. 10^{-4}, highlighting the excellent strain sensitivity of XRD.

From the observed mismatch between InP and GaInP and Vegard's law, we calculated the average Ga content in the $Ga_xIn_{1-x}P$ segments to be x = 21%, assuming no average strain in the GaInP. In comparison, point measurements from Energy-dispersive X-ray spectroscopy (EDS) of a different nanowire showed a Ga composition of x = 36%. From ptychography we obtained a high-resolution map (Fig. S1(a) in the ESM) of the nanowire and note that it is slightly longer, 2.5 μm, compared with the one investigated by STEM, 2.1 μm. This suggests that the nanowire in the XRD maps originated closer to the sample edge, which has a slightly higher growth rate and higher In fraction due to edge effects.

The length of the InP segments has a strong effect on the measured strain, both the average values and the distributions. The InP segments are compressively stressed by the GaInP segments in the radial direction, which intuitively should lead to an expansion in the axial direction that we probe. However, our measurements show a significantly more complex strain distribution. In the two largest InP segments, we indeed observe a lattice expansion (in the axial dimension) towards the surface, but away from the surface the strain is compressive, in particular in the center. In contrast, the 45 nm segment only shows a slight decrease from the center to the surface. The average strain is −0.01%, 0.00% and 0.04% in the 170, 80, and 45 nm InP segments, respectively. The observed strain variation within those respective segments is about 0.12%, 0.10% and 0.04%. Note that such small variations would be very challenging to quantify with TEM.

Comparing the GaInP segments with each other, we observe an overall gradient from high to low lattice constant towards the seed particle. This is most likely due to a gradient in the composition of the $Ga_xIn_{1-x}P$ alloy, as previously observed [47, 48]. As a consequence of the growth process, where the In is supplied primarily via surface diffusion, the supply of In decreases the longer the nanowire becomes. Hence, there is a slight gradient in composition such that there is more Ga close to the seed particle than close to the substrate. Therefore, the GaInP lattice and the mismatch to InP become larger along the growth direction, that is, closer to the seed particle. The composition can be calculated from the lattice constant as shown in Fig. S2 in the ESM. We find that the composition changes from x = 19% to x = 23% between the four segments, implying a gradient of about 3% per μm. This is in good agreement with measurements of similar nanowires using scanning X-ray fluorescence [47]. Compositional analysis with EDS line scans also shows a sharper change in Ga and In composition when switching from $Ga_xIn_{1-x}P$ to InP than vice versa (Fig. S3 in the ESM).

The strain is also not symmetric within the GaInP segments, where the maximum relative strain is shifted to the left, closer to the seed particle. Thus, within the segments the trend is reversed compared with the overall gradient. An axial asymmetry in strain is also seen in the InP segments, where the strain minima are shifted slightly to the right of the center.

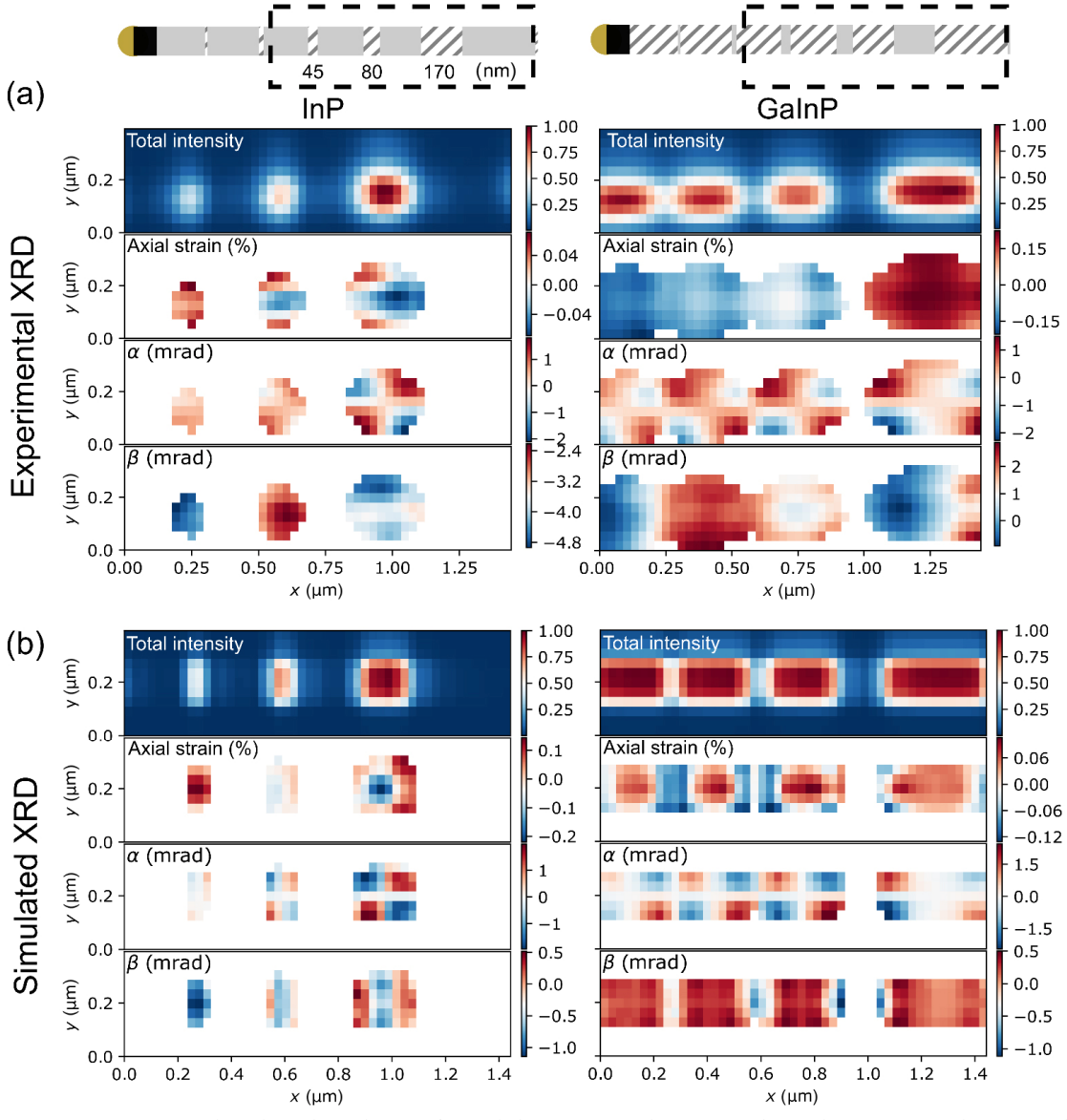

Figure 2 Scanning XRD experimental results and simulations of a single heterostructured nanowire. The pixel sizes are 30 and 40 nm in the x and y directions, respectively. The InP measurements and simulations are shown in the left column, and the GaInP ones in the right column. (a) Experimental results: total scattered intensity in Bragg, axial strain, tilt around z, α, tilt around y, β. (b) The corresponding maps from simulated diffraction.

In addition to strain, scanning XRD is very sensitive to small variations in local lattice tilt [28, 49]. From our reciprocal space mapping, we calculate the lattice tilt in two directions: The tilt around z, α and the tilt around y, β, see Fig. 1(e). We observe a cross-shaped profile of α in the largest InP segments, with the strongest tilt at the corners. Following the interface edge or the nanowire surface, the tilt decreases to zero at the center and then changes sign towards the opposite edge. The sensitivity to this tilt is better than 0.1 mrad. A matching tilt distribution is found in the GaInP segments, with the same magnitude but with the sign flipped. Note that we do not find an overall gradient of α, which would suggest bending of the nanowire in the sample plane.

The distribution of the tilt around y, β, is more difficult to analyze. In our measurement geometry, we are very sensitive to tilt around z, α, since it is directly coupled to the vertical position of the Bragg peak on the detector, but we are less sensitive to β as it relies on sampling with the rotation. There seems to be a general gradient in the InP and GaInP segments for the β tilt, changing along the axis from negative to positive back to negative again. Such a gradient is consistent with an arch shape of the nanowire, possibly due to adhesion to the substrate. The tilt maps could be used to reconstruct the shape of the nanowire in 3D [28], but this is out of the scope of the present work.

3.2 FEM simulations of strain

To understand the asymmetries in the strain maps and to confirm the dome shaped strain profiles seen in the tilt maps, we performed a full simulation of the sample and the experiment starting with a 3D FEM strain simulation using the software COMSOL Multiphysics. We used the average measured value for the lattice mismatch, 1.5%, as the initial strain applied to the InP segments (Fig. 3), without any composition gradient or bending of the wire. In Figs. 3(a)–3(d), we show central slices of the 3D simulation, which has radial symmetry, showing the radial (Figs. 3(a) and 3(c)) and axial (Figs. 3(b) and 3(d)) strain components. The axial component is the one that is measured in our experiment. Near the segment interfaces, the InP crystal, which has the larger lattice constant, is radially compressively strained (shown in blue) while the GaInP is tensile strained (shown in red), see Fig. 3(a). The strain distributions

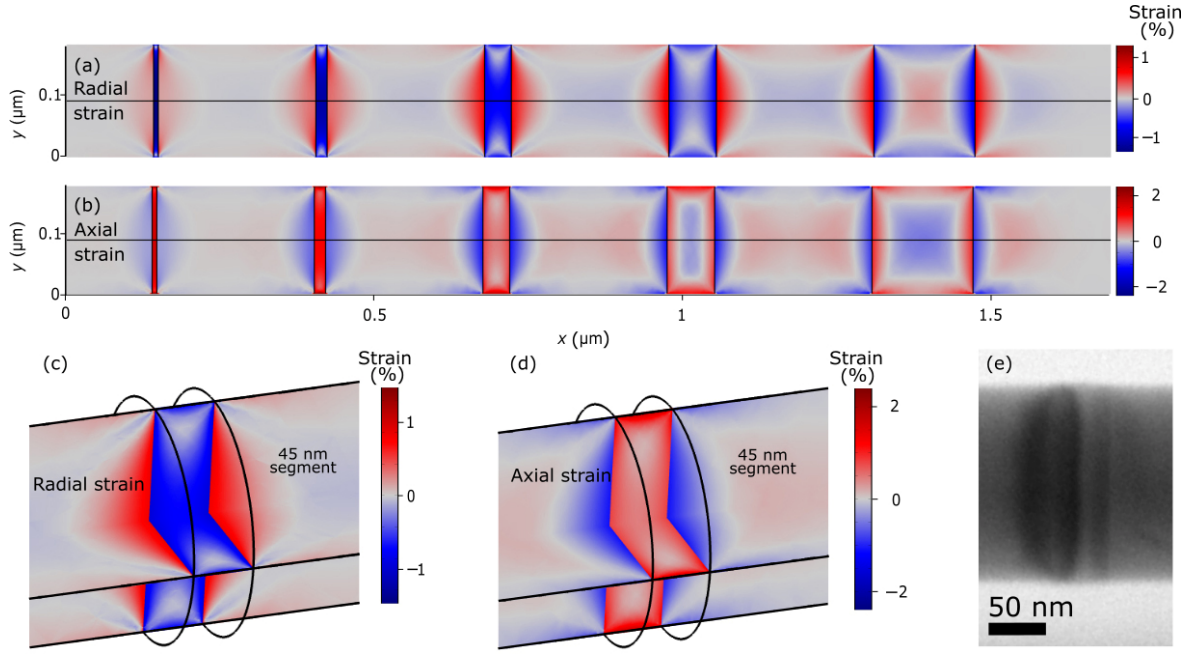

Figure 3 (a)–(d) 3D FEM simulations of elastic strain caused by a lattice mismatch of 1.5% between the segments. (a) Strain along the radial dimension in a central slice of the nanowire. (b) Strain in the axial dimension of the nanowire. (c) Strain in the radial dimension; a two-cut plot of the 45 nm segment. (d) Strain in the axial dimension of the nanowire; a two-cut plot of the 45 nm segment. All the strain results are radially symmetric. (e) STEM aligned in a <112> direction of a 45 nm segment.

form dome shapes at the segment interfaces, qualitatively in line with previous simulations [25, 27]. As expected, the crystal expands in the axial direction where it compresses radially, as shown in Fig. 3(b). The magnitude of the strain is about twice as large in the axial dimension, again in agreement with previously reported simulations [27].

A closer view of the 45 nm segment is seen in Figs. 3(c) and 3(d). As a comparison, we show STEM of a 45 nm segment in a nanowire from the same sample in Fig. 3(e). The strain gives rise to contrast due to a Moiré effect, showing a dome shaped profile in excellent qualitative agreement with our FEM simulations. Quantifying the strain from such a STEM image is challenging, however. The STEM also shows that the InP segment has a slightly larger radius, about 2–4 nm more than the surrounding GaInP segments, something that is not resolved in the XRD strain maps. The FEM simulations predict that the lateral strain relaxation leads to a maximum radial displacement of 1.3 nm. Note that there could be a slight radial growth on the InP segment as well, despite the use of *in situ* HCl etching during growth [50], which is not included in the simulations.

3.3 Simulated scanning XRD

The FEM simulations generate the 3D strain and the displacement field, $u(\boldsymbol{r})$, where $\boldsymbol{r}$ is the real space coordinate, with very high real-space resolution. The axial strain component cannot be directly compared with the experimental strain maps, since in the measurement the axial strain is convoluted with the footprint of the beam. The beam creates an averaging effect that is complicated by the complex profile. Therefore, we made a full simulation of the scanning XRD experiment. For each beam position j, we calculated the exit wave Ψ_j using the Bragg vector $\boldsymbol{G}_{hkl}$ ($|\boldsymbol{G}_{111}| = 1.85$ Å^{-1} for InP and $|\boldsymbol{G}_{111}| = 1.92$ Å^{-1} for $Ga_xIn_{1-x}P$ with x = 21%) and the probe function $P(\boldsymbol{r})$ as [51, 52]

$$\Psi_j = |\rho_j(\boldsymbol{r})|\, e^{i\boldsymbol{G}_{hkl}\cdot\boldsymbol{u}_j(\boldsymbol{r})} P(\boldsymbol{r})$$

The electron density in a single position, $\rho_j(\boldsymbol{r})$ was represented as a binary shape function. The probe profile at focus, $P(\boldsymbol{r})$, was reconstructed from a ptychographic measurement on a Siemens star test sample (Fig. S1(b) in the ESM). Next, the exit wave was propagated to the far field with a Fourier transform, and the intensity on the Bragg detector in one probe position was calculated as $I_j = |\mathcal{F}(\Psi_j)|^2$.

We show a comparison of an experimental and a simulated Bragg peak in Fig. 4, with the three central cuts when the beam is centered on the 170 nm InP segment. Qualitatively, the simulated Bragg peaks show many similarities with the measured ones. The shape of the Bragg peak is largely determined by the Fourier transform of the shape function of the segment. The cuts perpendicular to q_x and q_y (left and right), show the Fourier transform of the square dimensions of the segment, but the strain gradients curve the shape of the fringes. Correspondingly, the cut perpendicular to q_z (middle) shows the Fourier transform of the circular dimension. To better illustrate the appearance of the 3D Bragg peak and how it is affected by strain, we also show an idealized simulation with a high-flux plane wave probe and smaller pixels in Fig. S4 in the ESM.

The final step in the simulation is to make a center of mass analysis of the Bragg peaks at each position, just like the measured data is treated. The simulated intensity, strain and tilt maps are shown together with the measured ones in Fig. 2(b). Overall, we find excellent qualitative agreement between the simulated and measured strain and tilt maps. In the following, we will discuss similarities and differences between the simulations and measurements in detail.

3.4 Discussion

In the large InP and GaInP segments, both the simulation and the measurements show that the strain in the central parts of the segments changes sign compared with the edges. For instance, the largest InP segment shows an intuitively expected tensile radial strain near the mismatched heterointerfaces, but also a slight compressive strain in the center. With decreasing

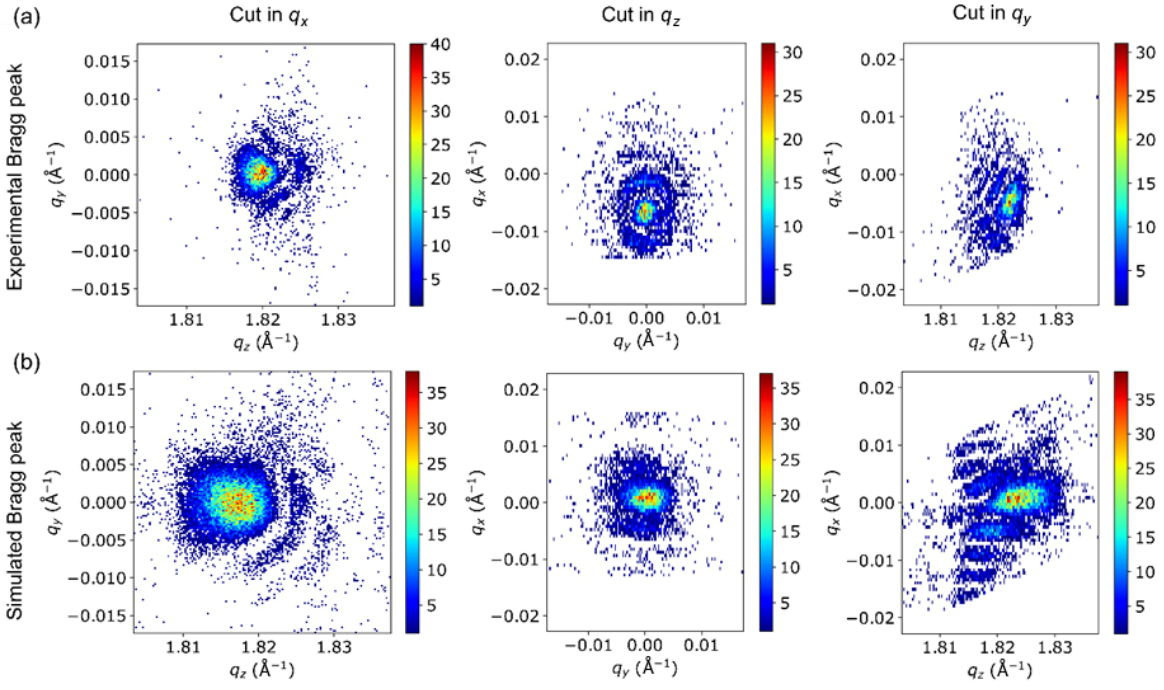

Figure 4 Three central cuts of diffraction from the 170 nm InP segment presented in an orthogonal system. (a) Measured scattering with an acquisition time of 0.12 s for each frame. (b) Simulated scattering calculated from the displacement field from the FEM model (Fig. 3(b)) and the experimental probe as reconstructed from ptychography (Fig. S1(b) in the ESM).

segment length, the strain in the InP segments increases, and for the two shortest InP segments, almost the entire segments have the same lattice constant as GaInP. Comparing the InP segments with each other, the trend is that in the radial direction the lattice in the shorter segments adapts more to the surrounding GaInP crystal.

Comparing the GaInP segments with the largest InP segment, we find a similar but inverted strain distribution in both the simulations and the measurements. Since the GaInP simulations did not include the axial gradient in the Ga composition, the strain profiles in the different segments are similar to each other.

The simulated lattice tilt, α, shows excellent quantitative and qualitative agreement with the measurements. Evidently, the sign shift comes from the dome-shaped strain profile, which means that the crystal is tilted in the opposite direction in each half across the nanowire. This can be seen in the measured and simulated XRD in Fig. 2(a) and 2(b), respectively. The tilt is not affected by the $Ga_xIn_{1-x}P$ composition gradient. The tilt around y, β, in the measurements is dominated by an overall arch shaped bending of the nanowire, which is not included in the simulations.

While the simulations are qualitatively similar to the measurements, the quantitative comparison is less consistent. The simulated strain in the InP segments is about twice as large in the simulations as in the measurement. This could indicate that dislocations, which are not included in the FEM simulations, may have formed in the measured nanowire as a result of the lattice mismatch, since dislocations would reduce the strain. However, the tilt around z, α, is only marginally smaller in the measurements, which should not be possible with a partially relaxed strain. Instead, the difference in absolute strain could be due to limitations in the spatial resolution. The convolution of the 90 nm probe and the FEM modeled nanowire creates an average that serves to reduce the extreme values in the FEM model quite significantly. The intensity maps in the simulated XRD show segment edges with sharper profiles than in the measurements, which, together with the observation that the central structures in the simulated diffraction patterns are slightly larger than the measured ones, indicates the probe was slightly larger than anticipated in the experiment. A larger probe would increase the averaging effect and hence reduce the strain range. Possibly, the nanowire was slightly out of focus. The most extreme strain values could be further blurred by imperfections in beam intensity and the scanning and rotation motors. Note that the measurement of the α tilt, which shows a much better agreement, relies only on the vertical center of mass on the detector, and is independent of the rotation motor and intensity fluctuations. In this sense, α in scanning XRD is similar to differential phase contrast in scanning transmission X-ray microscopy (STXM) [53].

4 Conclusions

To conclude, we have demonstrated high-resolution strain mapping of an axial nanowire heterostructured using scanning X-ray diffraction. This was performed at the first DLSR, MAX IV, where we obtained 2D strain maps with about 10^{-4} relative strain resolution. Several assumptions were made for the FEM model, such as perfectly sharp heterojunctions, no strain accommodation via defects, and no bending. High-resolution strain measurements were necessary to test these assumptions, which have previously been used in theoretical reports. The strain maps and the complementing simulations show how the strain relaxes at the surface of the nanowire, as previously theoretically predicted. We find that the InP segment length has profound quantitative and qualitative effects on the strain distribution. The largest segments show a complex 3D variation with both compressive and tensile strain, differing strongly from thin film growth, while the shortest measured InP segment is almost fully adapted to the GaInP lattice. The different strain profiles can have a strong effect on the electronic and optical properties of the InP segments. The positively (tensile) strained regions should have a reduced local band gap, which for instance

leads to a localization of optically excited charge carriers. In the two longest InP segments, the most positively axially strained region is found in the center, while in the 40 nm segment this region forms a ring around the center. Our diffraction simulations show how the averaging of the probe changes the quantification of strain from a FEM model, highlighting the importance of simulating the experiment with a realistic model of the X-ray focus to be able to compare with measurements. The results demonstrate that nano-XRD can reach sufficient spatial resolution to quantitatively map the strain field in heterostructured nanowires.

Further improvements in spatial resolution should also lead to enhanced sensitivity to spatial variations in strain. The most straightforward strategy to improve the spatial resolution is to develop the X-ray optics, where the state of the art currently reaches around and slightly below 10 nm [33, 54]. An alternative approach is to take advantage of the coherence of the X-rays and use phase retrieval methods [51, 55, 56] to achieve sub-beam spatial resolution. The present study was one of the first at the NanoMAX beamline, which can currently deliver about 10 times more coherent flux than at the time of the present experiment [57], making it an ideal system for coherent Bragg methods.

5 Methods

5.1 Growth

The Au seed particle array was defined on a 2" InP (111)B wafer by nanoimprint lithography, reactive ion etching, metal evaporation, and lift-off, resulting in a hexagonal pattern of Au particles with a pitch of 500 nm [44]. The imprinted InP wafer was cleaved into smaller samples used for growth.

The nanowires were grown in a low pressure (100 mbar) metal-organic vapor phase epitaxy system (Aixtron 200/4) with a total flow of 13 L/min and H_2 as the carrier gas. In order to improve pattern preservation, a pre-anneal nucleation step [44] was performed at 280 °C for 1 min with molar fractions of trimethylindium (TMIn) of $\chi_{TMIn} = 8.9 \times 10^{-5}$ and phosphine (PH_3) of $\chi_{PH3} = 6.9 \times 10^{-3}$. Then the sample was annealed for 10 min at 550 °C under $\chi_{PH3} = 3.5 \times 10^{-2}$ to desorb surface oxides. After annealing, the chamber was cooled to 440 °C. The growth was initiated with a InP nucleation step by adjusting PH_3 to $\chi_{PH3} = 6.9 \times 10^{-3}$ and introducing TMIn with $\chi_{TMIn} = 8.9 \times 10^{-5}$. After 15 s, HCl was introduced at a molar fraction of $\chi_{HCl} = 4.6 \times 10^{-5}$ to eliminate radial growth [50, 58]. After a total of 60 s InP growth, 4 min of InGaP growth was carried out by introducing trimethylgallium (TMGa) at a molar fraction of $\chi_{TMGa} = 1.4 \times 10^{-3}$ and by switching the other precursors to $\chi_{TMIn} = 2.7 \times 10^{-5}$, $\chi_{PH3} = 5.4 \times 10^{-3}$, and $\chi_{HCl} = 5.4 \times 10^{-5}$. After this, a barcode sequence was grown by alternating between InP, $\chi_{TMIn} = 5.4 \times 10^{-5}$, and InGaP, $\chi_{TMIn} = 2.7 \times 10^{-5}$ and $\chi_{TMGa} = 1.4 \times 10^{-3}$. PH_3 and HCl were kept constant as in the previous step. The 10 segments were grown each for 2 min, 2 min 50 s, 1 min, 3 min, 45 s, 3 min 10 s, 30 s, 3 min 20 s, 15 s, and 3 min 41 s, respectively. After the barcode sequence, TMIn was switched off for 2 min, while keeping PH_3, HCl, and TMGa unchanged. Finally, the flows of TMGa and HCl were switched off and the chamber was cooled to 300 °C under a PH_3/H_2 gas mixture.

5.2 TEM

For TEM measurements a JEOL 3000F was used. The nanowires were transferred to a lacey carbon copper grid by gently rubbing it on the growth substrate.

5.3 Nano-XRD

The nanowire sample holder was mounted in the nanofocus on top of a piezoelectric scanning stage. The Si_3N_4 window was located with transmission and X-ray fluorescence signal, which also showed contrast for single nanowires. Single nanowires were aligned horizontally using ptychography in the forward direction.

In transmission, we used a Pilatus 100K detector with 172 μm pixel size placed 4.2 m downstream of the nanofocus. Simultaneously, a Merlin detector with pixel size 55 μm was used in Bragg geometry 1.15 m from the nanofocus. Furthermore, the fluorescence signal was collected with an Amptek silicon drift detector close to the sample.

The transmission signal was used to track real space movements during the experiment, with STXM and ptychography. In a rocking curve, we saw systematic and unsystematic movements of the sample (see Fig. S5 in the ESM). To correct for these movements, we used maps of the summed Bragg intensity. We defined a small regular grid and connected each Bragg diffraction image to the correct position in real space (see Fig. S6 in the ESM for comparison).

The 3D Bragg peaks were sampled in the skewed reciprocal coordinate system (q_1, q_2, q_3), so the data was first converted to a Cartesian coordinate system to facilitate analysis. Then, the two centers of mass of the Bragg peaks were calculated for each scan point, giving their positions in reciprocal space. From these positions, we calculated the length of the scattering vector $\boldsymbol{Q}$ and the resulting local lattice constant, a, as well as the two lattice tilts.

The absolute values of the lattice constants were estimated from a calibration of the 2θ angle (the position of the Bragg detector) in the setup. By comparing the measured a_{InP} to the literature value $a_{InP} = 5.8687$ Å, we corrected a_{GaInP} with the same systematic error.

The beam profile was found from ptychographic reconstructions in the forward direction, on a Siemens star test sample, at the beginning and end of the beamtime (Fig. S1(b) in the ESM).

We observed no decay in the scattered signal over the measurement time, indicating insignificant beam damage to the wires.

5.4 Simulations

FEM simulation were performed using an isotropic linear elasticity model in the simulation software COMSOL Multiphysics. We used bulk literature values for the material parameters. For $Ga_xIn_{1-x}P$, we used interpolated values, assuming $x = 21\%$. The nanowire stub of InP of 10 nm was included in the COMSOL model but not shown in the figures. The end of the stub was constrained to be fixed in the simulation. The 2D probe profile was reconstructed from ptychography and normalized to a total intensity of 10^9 to match the experimental flux, then propagated to 3D. Then we applied a Poisson noise to the intensity with the rate parameter ($\lambda = 2$ to 25) adjusted to match the measured data.

Acknowledgements

We acknowledge the excellent support from the staff at the MAX IV Laboratory, in particular Gerardina Carbone for the preparations at the NanoMAX beamline. The MAX IV Laboratory receives funding through the Swedish Research Council under grant no 2013-02235. This research was funded by the Röntgen-Ångström Cluster, NanoLund, Marie Sklodowska Curie Actions, Cofund, Project INCA 600398, and the Swedish

Research Council grant number 2015-00331. L. J. L. and M. O. H. acknowledge support of NSF DMR 1611341 and 1905768. M. O. H. acknowledges support of the NSF GRFP and the NSF GROW program.

Funding note: Open access funding provided by Lund University.

Electronic Supplementary Material: Supplementary material (scanning XRD analysis details, compositional analysis with EDS, simulation and experimental details) is available in the online version of this article at https://doi.org/10.1007/s12274-020-2878-6.

Open Access This article is licensed under a Creative Commons Attribution 4.0 International License, which permits use, sharing, adaptation, distribution and reproduction in any medium or format, as long as you give appropriate credit to the original author(s) and the source, provide a link to the Creative Commons licence, and indicate if changes were made.

The images or other third party material in this article are included in the article's Creative Commons licence, unless indicated otherwise in a credit line to the material. If material is not included in the article's Creative Commons licence and your intended use is not permitted by statutory regulation or exceeds the permitted use, you will need to obtain permission directly from the copyright holder.

To view a copy of this licence, visit http://creativecommons.org/licenses/by/4.0/.

References

[1] Memisevic, E.; Hellenbrand, M.; Lind, E.; Persson, A. R.; Sant, S.; Schenk, A.; Svensson, J.; Wallenberg, R.; Wernersson, L. E. Individual defects in InAs/InGaAsSb/GaSb nanowire tunnel field-effect transistors operating below 60 mV/decade. *Nano Lett.* **2017**, *17*, 4373–4380.

[2] Tomioka, K.; Yoshimura, M.; Fukui, T. A III–V nanowire channel on silicon for high-performance vertical transistors. *Nature* **2012**, *488*, 189–192.

[3] Jia, C. C.; Lin, Z. Y.; Huang, Y.; Duan, X. F. Nanowire electronics: From nanoscale to macroscale. *Chem. Rev.* **2019**, *119*, 9074–9135.

[4] Haverkort, J. E. M.; Garnett, E. C.; Bakkers, E. P. A. M. Fundamentals of the nanowire solar cell: Optimization of the open circuit voltage. *Appl. Phys. Rev.* **2018**, *5*, 031106.

[5] Otnes, G.; Borgström, M. T. Towards high efficiency nanowire solar cells. *Nano Today* **2017**, *12*, 31–45.

[6] Wallentin, J.; Anttu, N.; Asoli, D.; Huffman, M.; Åberg, I.; Magnusson, M. H.; Siefer, G.; Fuss-Kailuweit, P.; Dimroth, F.; Witzigmann, B. et al. InP nanowire array solar cells achieving 13.8% efficiency by exceeding the ray optics limit. *Science* **2013**, *339*, 1057–1060.

[7] Soci, C.; Zhang, A.; Bao, X. Y.; Kim, H.; Lo, Y.; Wang, D. L. Nanowire photodetectors. *J. Nanosci. Nanotechnol.* **2010**, *10*, 1430–1449.

[8] Gudiksen, M. S.; Lauhon, L. J.; Wang, J. F.; Smith, D. C.; Lieber, C. M. Growth of nanowire superlattice structures for nanoscale photonics and electronics. *Nature* **2002**, *415*, 617–620.

[9] Gibson, S. J.; van Kasteren, B.; Tekcan, B.; Cui, Y. C.; van Dam, D.; Haverkort, J. E.; Bakkers, E. P. A. M.; Reimer, M. E. Tapered InP nanowire arrays for efficient broadband high-speed single-photon detection. *Nat. Nanotechnol.* **2019**, *14*, 473–479.

[10] Barrigón, E.; Heurlin, M.; Bi, Z. X.; Monemar, B.; Samuelson, L. Synthesis and applications of III–V nanowires. *Chem. Rev.* **2019**, *119*, 9170–9220.

[11] Motohisa, J.; Kameda, H.; Sasaki, M.; Tomioka, K. Characterization of nanowire light-emitting diodes grown by selective-area metal-organic vapor-phase epitaxy. *Nanotechnology* **2019**, *30*, 134002.

[12] Corfdir, P.; Marquardt, O.; Lewis, R. B.; Sinito, C.; Ramsteiner, M.; Trampert, A.; Jahn, U.; Geelhaar, L.; Brandt, O.; Fomin, V. M. Excitonic Aharonov–Bohm oscillations in core–shell nanowires. *Adv. Mater.* **2019**, *31*, 1805645.

[13] Mourik, V.; Zuo, K.; Frolov, S. M.; Plissard, S.; Bakkers, E. P. A. M.; Kouwenhoven, L. P. Signatures of Majorana fermions in hybrid superconductor-semiconductor nanowire devices. *Science* **2012**, *336*, 1003–1007.

[14] Zhang, H.; Liu, D. E.; Wimmer, M.; Kouwenhoven, L. P. Next steps of quantum transport in Majorana nanowire devices. *Nat. Commun.* **2019**, *10*, 5128.

[15] Świderski, M.; Zieliński, M. Electric field tuning of excitonic fine-structure splitting in asymmetric InAs/InP nanowire quantum dot molecules. *Phys. Rev. B* **2019**, *100*, 235417.

[16] Haffouz, S.; Zeuner, K. D.; Dalacu, D.; Poole, P. J.; Lapointe, J.; Poitras, D.; Mnaymneh, K.; Wu, X. H.; Couillard, M.; Korkusinski, M. et al. Bright single InAsP quantum dots at telecom wavelengths in position-controlled InP nanowires: The role of the photonic waveguide. *Nano Lett.* **2018**, *18*, 3047–3052.

[17] Björk, M. T.; Ohlsson, B. J.; Sass, T.; Persson, A. I.; Thelander, C.; Magnusson, M. H.; Deppert, K.; Wallenberg, L. R.; Samuelson, L. One-dimensional heterostructures in semiconductor nanowhiskers. *Appl. Phys. Lett.* **2002**, *80*, 1058–1060.

[18] Lauhon, L. J.; Gudiksen, M. S.; Wang, D. L.; Lieber, C. M. Epitaxial core–shell and core–multishell nanowire heterostructures. *Nature* **2002**, *420*, 57–61.

[19] Josefsson, M.; Svilans, A.; Burke, A. M.; Hoffmann, E. A.; Fahlvik, S.; Thelander, C.; Leijnse, M.; Linke, H. A quantum-dot heat engine operating close to the thermodynamic efficiency limits. *Nat. Nanotechnol.* **2018**, *13*, 920–924.

[20] LaPierre, R. R.; Chia, A. C. E.; Gibson, S. J.; Haapamaki, C. M.; Boulanger, J.; Yee, R.; Kuyanov, P.; Zhang, J.; Tajik, N.; Jewell, N. et al. III-V nanowire photovoltaics: Review of design for high efficiency. *Phys. Status Solidi* **2013**, *7*, 815–830.

[21] Yao, M. Q.; Cong, S.; Arab, S.; Huang, N. F.; Povinelli, M. L.; Cronin, S. B.; Dapkus, P. D.; Zhou, C. W. Tandem solar cells using GaAs nanowires on Si: Design, fabrication, and observation of voltage addition. *Nano Lett.* **2015**, *15*, 7217–7224.

[22] Zeng, X. L.; Otnes, G.; Heurlin, M.; Mourão, R. T.; Borgström, M. T. InP/GaInP nanowire tunnel diodes. *Nano Res.* **2018**, *11*, 2523–2531.

[23] Saxena, D.; Mokkapati, S.; Parkinson, P.; Jiang, N.; Gao, Q.; Tan, H. H.; Jagadish, C. Optically pumped room-temperature GaAs nanowire lasers. *Nat. Photonics* **2013**, *7*, 963–968.

[24] Ertekin, E.; Greaney, P. A.; Chrzan, D. C.; Sands, T. D. Equilibrium limits of coherency in strained nanowire heterostructures. *J. Appl. Phys.* **2005**, *97*, 114325.

[25] Ye, H.; Lu, P. F.; Yu, Z. Y.; Song, Y. X.; Wang, D. L.; Wang, S. M. Critical thickness and radius for axial heterostructure nanowires using finite-element method. *Nano Lett.* **2009**, *9*, 1921–1925.

[26] Glas, F. Critical dimensions for the plastic relaxation of strained axial heterostructures in free-standing nanowires. *Phys. Rev. B* **2006**, *74*, 121302.

[27] Glas, F. Strain in nanowires and nanowire heterostructures. *Semicond. Semimet.* **2015**, *93*, 79–123.

[28] Wallentin, J.; Jacobsson, D.; Osterhoff, M.; Borgstrom, M. T.; Salditt, T. Bending and twisting lattice tilt in strained core-shell nanowires revealed by nanofocused X-ray diffraction. *Nano Lett.* **2017**, *17*, 4143–4150.

[29] Sköld, N.; Wagner, J. B.; Karlsson, G.; Hernán, T.; Seifert, W.; Pistol, M. E.; Samuelson, L. Phase segregation in AlInP shells on GaAs nanowires. *Nano Lett.* **2006**, *6*, 2743–2747.

[30] Wen, C. Y.; Reuter, M. C.; Su, D.; Stach, E. A.; Ross, F. M. Strain and stability of ultrathin Ge layers in Si/Ge/Si axial heterojunction nanowires. *Nano Lett.* **2015**, *15*, 1654–1659.

[31] Larsson, M. W.; Wagner, J. B.; Wallin, M.; Håkansson, P.; Fröberg, L. E.; Samuelson, L.; Reine Wallenberg, L. Strain mapping in free-standing heterostructured wurtzite InAs/InP nanowires. *Nanotechnology* **2007**, *18*, 015504.

[32] Schropp, A.; Hoppe, R.; Patommel, J.; Samberg, D.; Seiboth, F.; Stephan, S.; Wellenreuther, G.; Falkenberg, G.; Schroer, C. G. Hard X-ray scanning microscopy with coherent radiation: Beyond the resolution of conventional X-ray microscopes. *Appl. Phys. Lett.* **2012**, *100*, 253112.

[33] Döring, F.; Robisch, A. L.; Eberl, C.; Osterhoff, M.; Ruhlandt, A.; Liese, T.; Schlenkrich, F.; Hoffmann, S.; Bartels, M.; Salditt, T. et al. Sub-5 nm hard X-ray point focusing by a combined Kirkpatrick-Baez mirror and multilayer zone plate. *Opt. Express* **2013**, *21*, 19311–19323.

[34] Schülli, T. U.; Leake, S. J. X-ray nanobeam diffraction imaging of materials. *Curr. Opin. Solid State Mater. Sci.* **2018**, *22*, 188–201.

[35] Stankevič, T.; Hilner, E.; Seiboth, F.; Ciechonski, R.; Vescovi, G.; Kryliouk, O.; Johansson, U.; Samuelson, L.; Wellenreuther, G.; Falkenberg, G. et al. Fast strain mapping of nanowire light-emitting diodes using nanofocused X-ray beams. *ACS Nano* **2015**, *9*, 6978–6984.

[36] Biermanns, A.; Breuer, S.; Davydok, A.; Geelhaar, L.; Pietsch, U. Structural polytypism and residual strain in GaAs nanowires grown on Si(111) probed by single-nanowire X-ray diffraction. *J. Appl. Cryst.* **2012**, *45*, 239–244.

[37] Keplinger, M.; Mandl, B.; Kriegner, D.; Holý, V.; Samuelsson, L.; Bauer, G.; Deppert, K.; Stangl, J. X-ray diffraction strain analysis of a single axial $InAs_{1-x}P_x$ nanowire segment. *J. Synchrotron Radiat.* **2015**, *22*, 59–66.

[38] Jacques, V. L. R.; Carbone, D.; Ghisleni, R.; Thilly, L. Counting dislocations in microcrystals by coherent X-ray diffraction. *Phys. Rev. Lett.* **2013**, *111*, 065503.

[39] Hrauda, N.; Zhang, J. J.; Wintersberger, E.; Etzelstorfer, T.; Mandl, B.; Stangl, J.; Carbone, D.; Holý, V.; Jovanović, V.; Biasotto, C. et al. X-ray nanodiffraction on a single sige quantum dot inside a functioning field-effect transistor. *Nano Lett.* **2011**, *11*, 2875–2880.

[40] Lazarev, S.; Dzhigaev, D.; Bi, Z. X.; Nowzari, A.; Kim, Y. Y.; Rose, M.; Zaluzhnyy, I. A.; Gorobtsov, O. Y.; Zozulya, A. V.; Lenrick, F. et al. Structural changes in a single GaN nanowire under applied voltage bias. *Nano Lett.* **2018**, *18*, 5446–5452.

[41] Wallentin, J.; Osterhoff, M.; Salditt, T. In operando X-ray nano-diffraction reveals electrically induced bending and lattice contraction in a single nanowire device. *Adv. Mater.* **2016**, *28*, 1788–1792.

[42] Eriksson, M.; van der Veen, J. F.; Quitmann, C. Diffraction-limited storage rings—A window to the science of tomorrow. *J. Synchrotron Radiat.* **2014**, *21*, 837–842.

[43] Vogt, U.; Parfeniukas, K.; Stankevič, T.; Kalbfleisch, S.; Liebi, M.; Matej, Z.; Björling, A.; Carbone, G.; Mikkelsen, A.; Johansson, U. First X-ray nanoimaging experiments at nanomax. In *Proceedings of X-Ray Nanoimaging: Instruments and Methods III 2017*, San Diego, USA, 2017; p 7.

[44] Otnes, G.; Heurlin, M.; Graczyk, M.; Wallentin, J.; Jacobsson, D.; Berg, A.; Maximov, I.; Borgström, M. T. Strategies to obtain pattern fidelity in nanowire growth from large-area surfaces patterned using nanoimprint lithography. *Nano Res.* **2016**, *9*, 2852–2861.

[45] Björling, A.; Kalbfleisch, S.; Kahnt, M.; Sala, S.; Parfeniukas, K.; Vogt, U.; Carbone, D.; Johansson, U. Ptychographic characterization of a coherent nanofocused X-ray beam. *Opt. Express* **2020**, *28*, 5069–5076.

[46] Chahine, G. A.; Richard, M. I.; Homs-Regojo, R. A.; Tran-Caliste, T. N.; Carbone, D.; Jaques, V. L. R.; Grifone, R.; Boesecke, P.; Katzer, J.; Costina, I. et al. Imaging of strain and lattice orientation by quick scanning X-ray microscopy combined with three-dimensional reciprocal space mapping. *J. Appl. Cryst.* **2014**, *47*, 762–769.

[47] Troian, A.; Otnes, G.; Zeng, X. L.; Chayanun, L.; Dagytė, V.; Hammarberg, S.; Salomon, D.; Timm, R.; Mikkelsen, A.; Borgström, M. T. et al. Nanobeam X-ray fluorescence dopant mapping reveals dynamics of *in situ* Zn-doping in nanowires. *Nano Lett.* **2018**, *18*, 6461–6468.

[48] Otnes, G.; Heurlin, M.; Zeng, X. L.; Borgström, M. T. $In_xGa_{1-x}P$ nanowire growth dynamics strongly affected by doping using diethylzinc. *Nano Lett.* **2017**, *17*, 702–707.

[49] Etzelstorfer, T.; Süess, M. J.; Schiefler, G. L.; Jacques, V. L. R.; Carbone, D.; Chrastina, D.; Isella, G.; Spolenak, R.; Stangl, J.; Sigg, H. et al. Scanning X-ray strain microscopy of inhomogeneously strained Ge micro-bridges. *J. Synchrotron Radiat.* **2014**, *21*, 111–118.

[50] Borgström, M. T.; Wallentin, J.; Trägårdh, J.; Ramvall, P.; Ek, M.; Wallenberg, L. R.; Samuelson, L.; Deppert, K. *In situ* etching for total control over axial and radial nanowire growth. *Nano Res.* **2010**, *3*, 264–270.

[51] Godard, P.; Carbone, G.; Allain, M.; Mastropietro, F.; Chen, G.; Capello, L.; Diaz, A.; Metzger, T. H.; Stangl, J.; Chamard, V. Three-dimensional high-resolution quantitative microscopy of extended crystals. *Nat. Commun.* **2011**, *2*, 568.

[52] Robinson, I.; Harder, R. Coherent X-ray diffraction imaging of strain at the nanoscale. *Nat. Mater.* **2009**, *8*, 291–298.

[53] Bunk, O.; Bech, M.; Jensen, T. H.; Feidenhans'l, R.; Binderup, T.; Menzel, A.; Pfeiffer, F. Multimodal X-ray scatter imaging. *New J. Phys.* **2009**, *11*, 123016.

[54] Bajt, S.; Prasciolu, M.; Fleckenstein, H.; Domaracký, M.; Chapman, H. N.; Morgan, A. J.; Yefanov, O.; Messerschmidt, M.; Du, Y.; Murray, K. T. et al. X-ray focusing with efficient high-NA multilayer laue lenses. *Light Sci. Appl.* **2018**, *7*, 17162.

[55] Hill, M. O.; Calvo-Almazan, I.; Allain, M.; Holt, M. V.; Ulvestad, A.; Treu, J.; Koblmuller, G.; Huang, C. Y.; Huang, X. J.; Yan, H. F. et al. Measuring three-dimensional strain and structural defects in a single InGaAs nanowire using coherent X-ray multiangle Bragg projection ptychography. *Nano Lett.* **2018**, *18*, 811–819.

[56] Pfeifer, M. A.; Williams, G. J.; Vartanyants, I. A.; Harder, R.; Robinson, I. K. Three-dimensional mapping of a deformation field inside a nanocrystal. *Nature* **2006**, *442*, 63–66.

[57] Björling, A.; Carbone, D.; Sarabia, F. J.; Hammarberg, S.; Feliu, J. M.; Solla-Gullón, J. Coherent Bragg imaging of 60 nm Au nanoparticles under electrochemical control at the nanomax beamline. *J. Synchrotron Radiat.* **2019**, *26*, 1830–1834.

[58] Jacobsson, D.; Persson, J. M.; Kriegner, D.; Etzelstorfer, T.; Wallentin, J.; Wagner, J. B.; Stangl, J.; Samuelson, L.; Deppert, K.; Borgström, M. T. Particle-assisted $Ga_xIn_{1-x}P$ nanowire growth for designed bandgap structures. *Nanotechnology* **2012**, *23*, 245601.

Paper II

crystals

MDPI

Article

Combining Nanofocused X-Rays with Electrical Measurements at the NanoMAX Beamline

Lert Chayanun [1,*], Susanna Hammarberg [1], Hanna Dierks [1], Gaute Otnes [2], Alexander Björling [3], Magnus T Borgström [2] and Jesper Wallentin [1]

1 Synchrotron radiation research and NanoLund, Lund University, Lund 22100, Sweden
2 Solid state physics and NanoLund, Lund University, Lund 22100, Sweden
3 MAX IV laboratory, Lund University, Lund 22100, Sweden
* Correspondence: lert.chayanun@sljus.lu.se; Tel.: +46-76-774-2623

Received: 3 July 2019; Accepted: 15 August 2019; Published: 20 August 2019

Abstract: The advent of nanofocused X-ray beams has allowed the study of single nanocrystals and complete nanoscale devices in a nondestructive manner, using techniques such as scanning transmission X-ray microscopy (STXM), X-ray fluorescence (XRF) and X-ray diffraction (XRD). Further insight into semiconductor devices can be achieved by combining these techniques with simultaneous electrical measurements. Here, we present a system for electrical biasing and current measurement of single nanostructure devices, which has been developed for the NanoMAX beamline at the fourth-generation synchrotron, MAX IV, Sweden. The system was tested on single InP nanowire devices. The mechanical stability was sufficient to collect scanning XRD and XRF maps with a 50 nm diameter focus. The dark noise of the current measurement system was about 3 fA, which allowed fly scan measurements of X-ray beam induced current (XBIC) in single nanowire devices.

Keywords: X-ray beam induced current (XBIC); scanning X-ray diffraction (XRD); nanowire

1. Introduction

X-rays have a long penetration depth compared with electron and optical beams [1], and modern X-ray optics can provide nanofocusing at the range of tens of nanometers [2,3]. This development has made it possible to investigate complete single semiconductor nanostructures [4–11]. By combining the nanofocused X-ray probe with an applied electrical bias as well as electrical current detection, nanodevices can be investigated in more or less realistic operational conditions. In such investigations, the X-rays can be used as a pump, that is, as excitation source with the electrical measurements as a probe, or vice versa.

As an excitation source, X-rays can be used to locally excite charge carriers in semiconductor materials, and if an electrical current is measured, the technique is called X-ray beam induced current (XBIC). The excitation process is similar to that achieved using visible light and electron beams, and XBIC is therefore similar to scanning photocurrent microscopy (SPCM) [12] and electron beam induced current (EBIC) [13]. X-rays have the benefits of a smaller focused beam than laser light and a longer penetration depth than electron beams. Therefore, XBIC could help developing the next-generation nanometer scale electronic devices.

Conversely, an electrical bias can be applied on a nanodevice, with X-rays as a probe. In particular, X-ray diffraction (XRD) can be used to quantify electric-field induced changes in single nanodevices [14–17]. XRD is in principle able to characterize any changes that couple to the crystal lattice, such a piezoelectricity and heating. While the spatial resolution of regular scanning XRD is limited by the focus size, phase retrieval techniques can overcome this limitation [18,19].

In this article, we will describe a system for combining electrical bias and measurements with nanofocused X-ray methods. The setup has been implemented and tested at the NanoMAX beamline [20] at the new synchrotron source, MAX IV, in Lund, Sweden [21], but it can easily be moved to other synchrotrons. To shed light on the detected electrical signal from the studied devices, the internal noise of this measurement system was studied. We also demonstrate multimode imaging using simultaneous STXM, XRF, XBIC, and scanning XRD from single nanowire devices.

The devices we have studied are based on semiconductor nanowires, but the system is applicable to other nanostructured semiconductor devices. Semiconductor nanowires have been studied for decades due to their promising properties that could overcome limitations in devices based on bulk materials in terms of efficiency, cost and performance. For instance, nanowires have been developed for transistors [22], light emitting diodes (LED), lasers, and solar cells [23].

In STXM, the attenuated and scattered X-rays from the sample are collected while the sample is scanned through a focused X-ray beam. Several imaging contrast modes can be extracted from the transmitted beam, such as absorption contrast from the bright field, the deflected beam in the dark field, and the differential phase contrast (DPC) [24]. The spatial resolution of this imaging technique is limited to the size of the X-ray beam. By overlapping the beam while scanning the sample and having the detector in the far-field region, phase retrieval techniques such as ptychography can be employed to overcome the resolution limit of the focus size [25]. Although ptychography is out of the scope of this article, the described system is fully compatible with this method.

The XBIC signal is generated upon X-ray absorption at the atomic level which as a result excites an inner core electron of an atom as a photoelectron leaving behind a vacant state, called a core hole. A relaxation of higher states, to fill up this vacant state, will emit the excess energy in the form of another X-ray photon called X-ray fluorescence (XRF) emission or an excitation of an Auger electron. In case of semiconductor materials, this secondary electrons and photons can excite further electrons in a cascade process. Eventually, the excited charges will be thermalized to the band edge of the semiconductor. At this point, the charge carriers at the band edge can be collected through the well-known semiconductor carrier transport and recombination processes [26–28].

Unlike scanning XRD, which has been frequently used to study nanowires [15,17,19,29–35], there have only been a few examples of nanowire devices studied using XBIC [8,9,11,36]. XBIC has been employed for studying solar cells since the early 2000s [37,38], when it was mostly used to examine grain boundaries and precipitated metal in polycrystalline silicon for solar cells at micrometer resolution [39–41]. With the recent development of nanofocused X-ray beams [2,3], XBIC has lately been used to study planar solar cells, made of materials such as $Cu(In_{(1-x)}Ga_x)Se_2$ (CIGS), or perovskites, both at nanoscale resolution [42,43].

2. Methods

A photograph of the installed sample holder and a schematic of the experimental setup are shown in Figure 1a,b, respectively. There are specific requirements for a system for combining electrical bias and measurements with nanofocused X-ray techniques. Nanofocusing beamlines such as NanoMAX put some physical constraints on the sample holder. The optics have short focal lengths, which limits the available space. At NanoMAX, the useful working distance is on the order of cm, as shown in Figure 1a, and emerging sub-10 nm focusing optics often have focal depths of about 1 mm [44,45]. Since the sample holder is mounted on a high-precision piezo-motor stage, it needs to be lightweight, as well as mechanically stable and free from induced vibrations. The sample holder must have a hole that transmits both the direct beam, for STXM, and Bragg diffraction, for XRD. The sample holder needs to be able to scale the electrical connections from the electronics to the devices and it must be easy to change the sample as well as the active device on the sample. Finally, to be able to measure the electrical current in single nanodevices, the noise must be minimized.

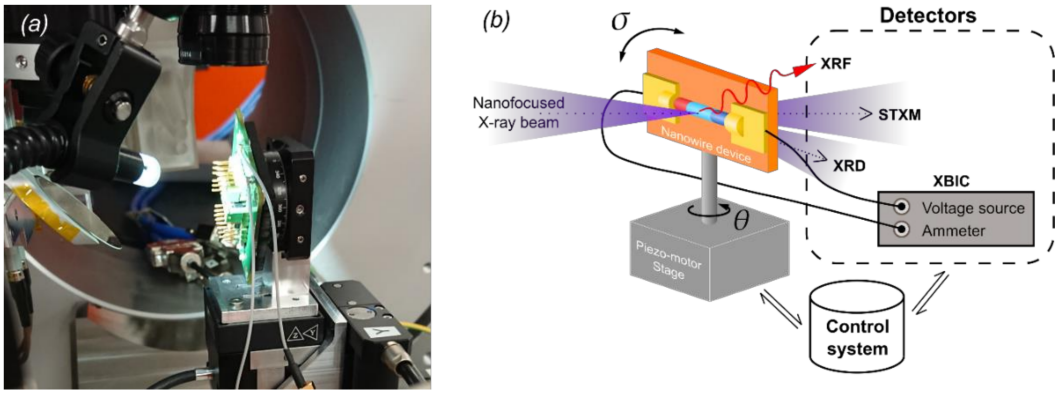

Figure 1. (**a**) Photograph of the installed sample holder on the piezo-motor stage at the NanoMAX beamline. A secured sample on the sample holder is installed on the piezo-motor stage. The tilted mirror to the left of the sample is the 45-degree mirror for the downstream optical microscope used to locate a particular nanowire device on the sample. (**b**) Schematic of the experimental setup at the end-station of NanoMAX. The sample was mounted on the piezo-motor stage, which can be moved in three dimensions and rotated about the vertical axis with the angle θ. Four measurement modes, X-ray fluorescence (XRF), Scanning transmission X-ray microscopy (STXM), X-ray diffraction (XRD), and X-ray beam induced current (XBIC), are available with this setup at NanoMAX. All the detectors as well as the piezo-motor stage are managed by the control-system.

The sample holder for the measurement, fulfilling the aforementioned requirements, is shown in Figure 2a. This sample holder consists of two main parts. First, there is a printed circuit board (PCB), which has a 16-pin chip socket, vertical pin connectors, and U.FL coaxial terminals (Figure 2b). The chip socket uses the well-established DIP format. Each sample chip is mounted and wire bonded to a DIP chip carrier, the white part in Figure 2b, before the experiment. The standard format makes it easy to change samples and to investigate different types of devices. Each slot of the chip socket is directly connected to a pin in a set of three vertical pins, where the two other pins are connected to different U.FL coaxial terminals on the circuit board (Figure S2b in Supplementary Materials). The active device on the chip is selected by connecting these pins. Each device is normally connected with two connections, although up to four can be used (e.g., for transistor gates). Each pin is connected to the voltage supply source on one end and the amperemeter on the other end, with U.FL coaxial connectors (gray cable in Figure 1a). This mini-coaxial connector, which allows a coaxial connection all the way from the PCB to the electronics, replaced pin connectors used in our previous sample holder design (Figure S2a). Please note that each U.FL connection is available on opposite sides of the PCB, since space constraints often makes one side impossible to reach.

The second part of the sample holder is the rotation mount (*Thorlabs CRM1/M*, Figure 2a) to which the circuit board is mounted. This allows the sample to be rotated around the optical axis with angle σ, such that the nanowire device can be manually aligned in vertical or horizontal, as shown in Figure 1b. This makes it easy to make one-dimensional scans along the nanowire axis. For XRD experiments, the manual rotation makes it possible to align the scattering plane in a favorable direction, without needing an extra goniometer rotation axis. The rotation mount is attached to an aluminum adapter plate, which is custom made to fit the top of the piezo motor.

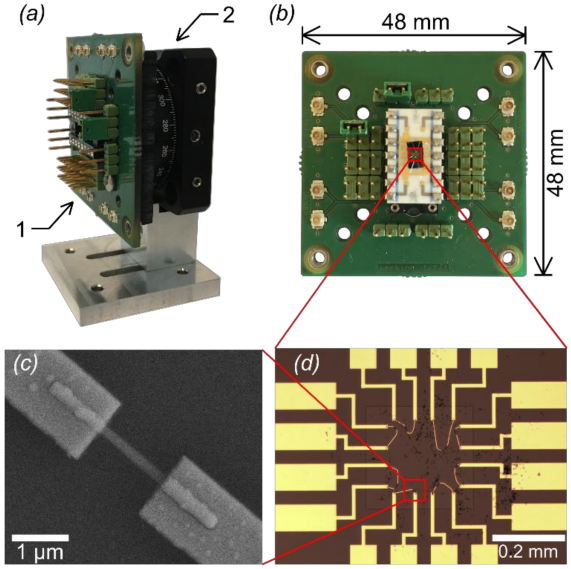

Figure 2. Nanowire device on the chip carrier and sample holder (**a**) The two main components of the sample holder are (1) the circuit board (green) and (2) the rotational mount (black). (**b**) The front side of the circuit board mounted with the 10 × 18 mm 14-pin chip carrier which has the nanowire device on the top. The circuit board consists of a 16-pin chip socket, vertical pins and U.FL terminals. This circuit board size is 48 × 48 mm. This side faces upstream towards the X-ray beam. Each slot of the chip socket is connected to a pin in a set of three vertical pins. By selecting pins, a particular nanowire device can be connected to the external equipment. (**c**) SEM image of the contacted single nanowire device. (**d**) Microscope image of eight nanowire devices on a SiN membrane window, seen as a lighter square in the center, surrounded by Au bonding pads which was attached on the chip carrier in (**b**).

For the electrical bias and current measurements, we integrated the amperemeter, *Keysight B2985A*, into the control system. This amperemeter has a built-in voltage source and is used to collect the XBIC signal from the sample.

The X-rays in the experiment were generated by MAX IV (Lund, Sweden), which is the first fourth-generation synchrotron radiation source [21]. The NanoMAX beamline [20] uses a Kirkpatrick-Baez (KB) mirror pair to focus the X-rays down to about 50 nm. In this experiment, the energy of the beam was 15 keV. The sample holder was mounted on a piezo-motor stage, which can be scanned in all three directions. The two-axis goniometer can rotate the sample for X-ray diffraction experiments (Figure 1b). The available detectors at the end-station for this experiment were (1) *Pilatus 100K* for the transmission beam (2) *Merlin quad*, 2 × 2 Medipix chip, mounted on the robot arm for the Bragg diffraction, and (3) *Amptek XR-100 silicon drift detector* for the XRF emission from the sample (Figure 1b). All these components at the end station are operated by the TANGO-based control system [46].

Scanning measurements are traditionally performed step-by-step, allowing the motors to stop at each position before the data acquisition. With the high flux at beamlines such as NanoMAX, acquisition times of only 10–100 ms are typically necessary. The measurement time in a step scan is then dominated by an overhead from starting, stopping, and reading out the motor positions. To reduce this overhead, the control system at NanoMAX can employ "fly-scan", where the sample is continuously moving. This is not only much more efficient, but can lead to less sample drift and therefore, somewhat counter-intuitively, improved spatial resolution. While the stage motor is sweeping in the fast scan direction, the photon detectors are triggered by the control system [46]. In a typical step-by-step scan, the collected XBIC signal is read out with every step, but this is too slow for the fly-scan measurements. Instead, we connected the analog voltage output of the amperemeter to a voltage to frequency converter, which in turn was connected to the control system.

The tested nanodevice was a horizontal contacted single nanowire device with a *p-i-n* doped InP nanowire (Figure 2c,d). A similar type of nanowires has been developed for the next generation solar

cells [23], which have already been thoroughly studied using nano-XBIC and XRF in our previous works [10,11]. These nanowire devices were fabricated on a 0.25 × 0.25 mm Si_3N_4 membrane window on a 3 × 5 mm Si chip from *Silson* (Southam, Warwickshire, England). The chip was glued and wire bonded to a 10 × 18 mm 14-pin DIP chip carrier and secured on the sample holder as shown in Figure 2b. More details regarding the nanowire device can be found in the supporting information.

3. Results and Discussion

First, we investigated the internal electrical noise by measuring the background current of the nanowire device without an X-ray beam under dark conditions [47]. No applied bias was used. Three measured current ranges of the amperemeter were tested, namely 2 pA, 20 pA, and 200 pA. We expected that the operation of the piezo motors in the sample stage could induce noise during the measurement. Therefore, the experiment was done with and without moving piezo motors.

Figure 3 displays some of the results from the internal noise of the XBIC measurement system. The current in the nanowire device as a function of time, without moving the piezo motor, is displayed in Figure 3a for each of the three used current ranges of the amperemeter. The offsets between each measurement at different current ranges were affected by the accuracy of the amperemeter as mentioned in the data sheet of the equipment. We plotted these measurements as histograms, as shown in Figure 3b, and used the standard deviation (SD) to estimate the noise level. Figure 3b is a comparison of the new and the old sample holder with the U.FL coaxial terminal and pin terminal, respectively. The extracted SDs at different tested conditions are plotted in Figure 3c.

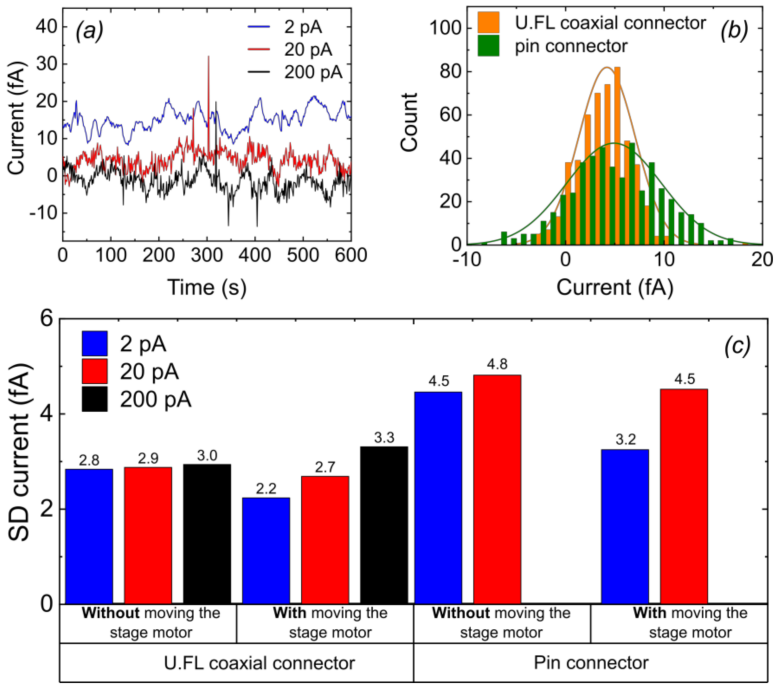

Figure 3. Internal noise of the XBIC measurement system. (**a**) The current through the nanowire device measured at 2 pA (blue trace), 20 pA (red trace) and 200 pA (black trace) current range of the amperemeter as a function of time. (**b**) The same measured current as (**a**) with a different sample holder design, that is, with U.FL connector (orange) and pin connector (green) as a terminal, plotted as a histogram exhibiting a normal distribution with fitting curve. These measurements were done at a 20 pA current range. (**c**) The standard deviation (SD) of the measured current at different measurement conditions.

The noise level calculated from the SD of the measurement indicated that there was only ~2% difference between each measurement range as represented in Figure 3c. With the operating stage motor, the measured spread in noise levels increased. However, none of these shifts could be considered statistically significant.

When we compared the old design of sample holder with the pin terminals, the SD of the old sample holder was consistently about ~35% higher at every measurement condition (Figure 3b,c). Apart from the improved noise level, measured data points with a non-repeatable spike (Figure S3), which occurred frequently using the old design in our previous XBIC experiment [9], were also reduced.

Finally, we investigated the effect of ambient room light, which resulted in a substantial photocurrent of around 25 fA (Figure S4). The noise level only changed marginally. Please note that applying light for the inline microscope leads to strong photocurrents (not shown), comparable in magnitude to the XBIC signal.

From these results, we can state that the dark noise in the measurement system is only about 3 fA, that is ~2×10^4 electrons per second, at these conditions. Please note that we did not employ any X-ray chopper, or any electrical shielding of the PCB. We did not observe any increase in noise from scanning with the piezo motors. The small device size, with an active depletion region volume of less than one μm^3, is probably a main reason for these very low noise levels.

Next, we demonstrate a two-dimensional fly-scan simultaneously mapping STXM, XRF, and XBIC of the nanowire device in Figure 4. The edge of the nanowire device distinguishing the nanowire from the metal contact can be seen from the DPC image of the detected STXM in Figure 4a. The DPC image is calculated as the radial magnitude of the vertical and horizontal DPCs. The XRF map in Figure 4b shows the relatively weak In L signal from the InP nanowire and the stronger Au L emission from the metal contacts. We can also observe the nanowire's Au seed particle beneath the metal contact (Figure 4a,b). Finally, the XBIC map is shown in Figure 4c.

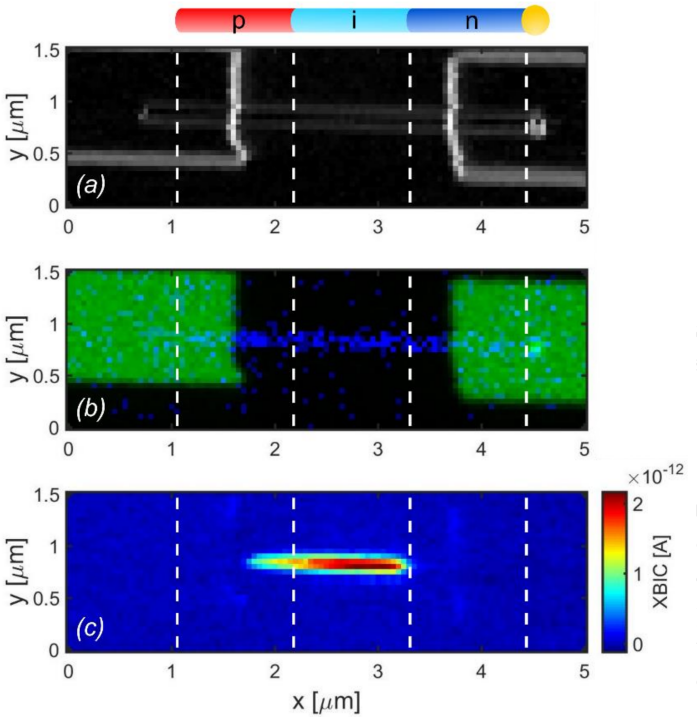

Figure 4. Multimodal imaging of a nanowire device. (**a**) Differential phase contrast (DPC) image of STXM showing the edges of the nanowire and metal contacts. (**b**) Material composition of the nanowire device, where the blue area and the green area are from XRF emission of In and Au atoms, respectively. (**c**) Color map of the XBIC signal from the nanowire device. The step length of this scan is 50 nm in both x- and y-direction with an acquisition time of 0.1 s and a latency time of 0.01 s for this fly-scan measurement. Dashed lines in these figures indicate the nominal position of each segment with the length of 1.1 μm using the Au particle observed in (**a**) and (**b**) as a reference position. Due to variations in the nanowire growth process, the actual length of this nanowire was slightly longer than the nominal one.

The XBIC map in Figure 4c sheds light on the underlying carrier collection mechanism of the nanowire device [11,48]. The signal is generated in the middle segment, approximately corresponding to the depletion region of the solar cell. After excitation, the electrons need an electric field to generate a net current, and such a field is only present in the depletion region. The signal is also affected by carrier recombination, which will be affected by doping, surface states and other recombination centers. This makes XBIC a versatile tool for investigating carrier dynamics and carrier collection in nanostructures.

With the information from the XRF map, we could investigate the material composition and doping concentration within nanowires as demonstrated by Johannes et al. [8] and Troian et al. [10]. The asymmetry of the XBIC profile in this map, with a long gradient at the left slope and a sharp one at the right slope, could be explained using the XRF map of the doping concentration as discussed in our previous work [11]. However, scanning XRF with sufficient sensitivity to measure the doping concentration requires a very high photon flux, which could affect the charge collection of the nanowire device monitored with XBIC or even damage the device. Therefore, the X-ray photon flux in this experiment was attenuated to be $\Phi \approx 5.7 \times 10^8$ s^{-1}, which is equivalent to the excitation level of 1 sun illumination as discussed in our previous work [11,49].

The yield of the photogenerated charges, η, contributing to the XBIC signal is the ratio between the X-ray photon energy and the ionization energy of the semiconductor, $\eta = E/\varepsilon$ [50]. With the X-ray energy in the order of keV, η can be several thousand in the XBIC process. The absorbed X-ray photon flux of the material at thickness, z, is quantified by the X-ray absorption probability, p_{abs}, which is the ratio between the absorbed and the incident X-ray photon flux. The absorption probability can be calculated from Beer–Lambert's law with knowledge of the X-ray absorption coefficient. This means that p_{abs} depends on the material composition and geometry as well as the X-ray energy. With these parameters, η and p_{abs}, the theoretical maximum XBIC signal can be calculated by $I_{XBIC} = q\eta p_{abs}\Phi$, where q is the charge constant and Φ is the incident X-ray photon flux. In this experiment, the yield of the photogenerated charges, η, and the X-ray absorption probability, p_{abs}, of the *p-i-n* doped InP nanowire were calculated to be $\eta = 3.5 \times 10^3$ and $p_{abs} = 0.003$, respectively. With the X-ray photon flux of $\Phi \approx 5.7 \times 10^8$ s^{-1}, the theoretical maximum XBIC signal is $I_{XBIC} = 9.7 \times 10^{-10}$ A. In contrast, the maximum measured XBIC from the nanowire device was 2.46×10^{-12} A. The difference between the measurement and the calculation is due to the high escape probability for secondary electrons and photons in these nanostructures [11,48].

Despite these losses, the XBIC signal was about three orders of magnitude higher than the dark current of the nanowire device and the internal noise of the measurement system. In fact, the XBIC showed the strongest contrast of all modes and was used for the sample alignment. Nonetheless, it is important to have enough latency time for the amperemeter to stabilize, since otherwise the measurement result is affected by the frequency of the triggering period (Figure S5). There is a slight distortion of the image, seen as a bent vertical edge of the metal contact, which is caused by drift in the scanning stage.

The scanning XRD results of a second device on the same chip are shown in Figure 5. Prior to the scanning XRD measurement, the nanowire device was aligned at the center of rotation of the motor stage. However, we still observed non-systematic real-space movement of the sample between different rotations in the XRF maps (Figure 5a). The XRF maps were then used to correct the position of the sample for each rotation angle, θ, before the reciprocal space mapping. The X-ray photon flux was increased to $\Phi \approx 1.4{\times}10^9$ s^{-1} for this measurement in order to get the Bragg diffraction with a considerable intensity. The total intensity of the Bragg diffraction is displayed in Figure 5b. A low-intensity region is observed around $x = 1.2$ µm, which is due to the very large tilt (bending) which put the nanowire lattice out of the angular range.

Reciprocal space mapping using the center of mass of the Bragg peak was used to generate a strain map (Figure 5c) as well as two tilt maps (Figure 5d,e), where α and β correspond to the tilt around the optical axis and the tilt around the vertical axis, respectively. The nanowire is strained, presumably due to stress from the metal contacts. The total range of the strain variation is about 0.1%, but we

can distinguish variations on the order of 0.01% (10^{-4}). The minimum strain variation that could be resolved in such a measurement is not trivial to quantify, but similar investigations have imaged strain variation of less than 10^{-5} [51]. Please note that the strain here (i.e., the change on average lattice plane distance) can also be affected by the doping profile and stacking faults.

The strong tilts are due to bending of the nanowire, which is induced by the metal contacts on both ends of the nanowire [15,17]. The shape of the nanowire can be reconstructed using a line integral [52], although such an analysis is outside of the scope of the present article. The nanowire here bends out in an arch above the substrate, similar to devices previously reported [15].

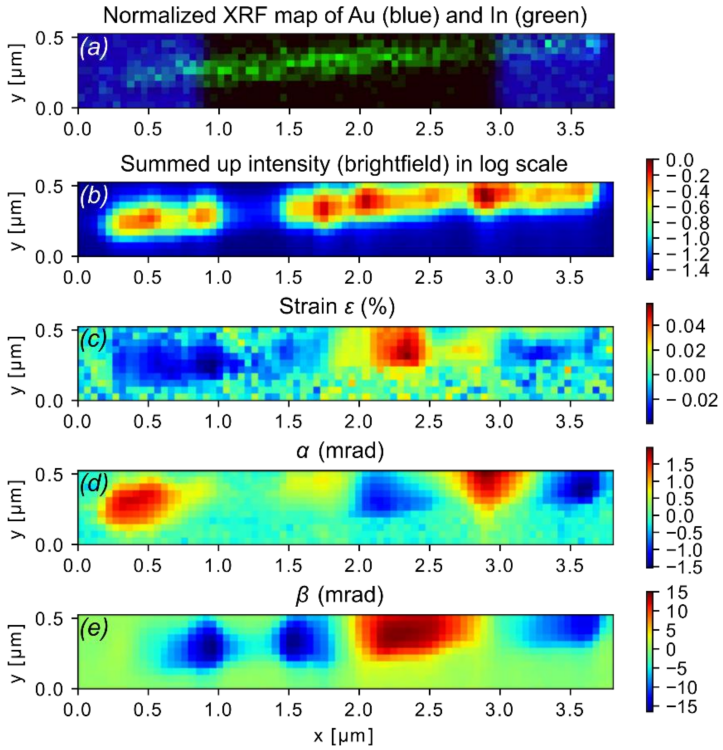

Figure 5. Scanning XRD of a single nanowire device (similar but not identical to the device in Figure 4): (**a**) XRF map, showing Au (blue) and In (green), (**b**) total intensity of the Bragg peaks (**c**) strain, in %, (**d**) lattice tilt around the optical axis, (**e**) lattice tilt around the vertical axis.

4. Conclusions

We have presented a system for combining nanofocused X-rays with electrical measurements at the NanoMAX beamline. The current from the tested sample can be directly collected, due to the low noise (~3 fA) which allows operando experiments simultaneously combining STXM, XRF, scanning XRD, and XBIC. In this way, information about morphology, elemental composition, crystal structure, and charge collection can be correlated. The system expands the capability of NanoMAX, by adding a new contrast mode, XBIC, that can be used to investigate carrier collection and carrier dynamics in nanostructured devices. Furthermore, it opens up the possibility to combine the established techniques at NanoMAX with an electric bias. For instance, it would be possible to study the strain and the shape of the nanowire as function of applied electric bias [15]. While we have demonstrated the system for a particular system, single nanowires, it should be useful for any devices where electrical bias or current collection is used, for instance transistors, batteries, light emitting diodes, or electrochemical devices.

Supplementary Materials: The following are available online at http://www.mdpi.com/2073-4352/9/8/432/s1, Figure S1: An image of horizontal contacted single nanowire device, Figure S2: An old designed sample holder and a schematic diagram of the circuit board, Figure S3: Internal noise of the measurement system using the old designed sample holder, Figure S4: Comparison noises with and without an ambient light, Figure S5: XBIC map using "fly-scan" with too short latency time.

Author Contributions: Conceptualization, J.W. and L.C.; methodology, J.W., A.B. and L.C.; software, J.W., S.H. and L.C.; validation, J.W. and A.B.; formal analysis, L.C. and S.H.; investigation, J.W., S.H., L.C. and H.D.; resources, A.B., G.O. and M.T.B.; data curation, L.C.; writing—original draft preparation, L.C..; writing—review and editing, J.W.; visualization, L.C.; supervision, J.W.; project administration, J.W.; funding acquisition, J.W.

Funding: This research was funded by the Röntgen-Ångström Cluster, NanoLund, Marie Sklodowska Curie Actions, Cofund, Project INCA 600398, and the Swedish Research Council grant number 2015-00331.

Acknowledgments: The support from the beamline staff is greatly acknowledged. The MAX IV Laboratory receives funding through the Swedish Research Council under grant no 2013-02235.

Conflicts of Interest: The authors declare no conflict of interest.

References

1. Stuckelberger, M.; West, B.; Husein, S.; Guthrey, H.; Al-Jassim, M.; Chakraborty, R.; Buonassisi, T.; Maser, J.M.; Lai, B.; Stripe, B. Latest developments in the x-ray-*based* characterization of thin-film solar cells. In Proceedings of the Photovoltaic Specialist Conference (PVSC), New Orleans, LA, USA, 14–19 June 2015; pp. 1–6.
2. Mimura, H.; Handa, S.; Kimura, T.; Yumoto, H.; Yamakawa, D.; Yokoyama, H.; Matsuyama, S.; Inagaki, K.; Yamamura, K.; Sano, Y.; et al. Breaking the 10-nm barrier in hard-X-ray focusing. *Nat. Phys.* **2010**, *6*, 122–125. [CrossRef]
3. Döring, F.; Robisch, A.L.; Eberl, C.; Osterhoff, M.; Ruhlandt, A.; Liese, T.; Schlenkrich, F.; Hoffmann, S.; Bartels, M.; Salditt, T.; et al. Sub-5 nm hard x-ray point focusing by a combined Kirkpatrick-Baez mirror and multilayer zone plate. *Opt. Express* **2013**, *21*, 19311–19323.
4. Holt, M.; Harder, R.; Winarski, R.; Rose, V. Nanoscale Hard X-Ray Microscopy Methods for Materials Studies. *Annu. Rev. Mater. Res.* **2013**, *43*, 183–211. [CrossRef]
5. Etzelstorfer, T.; Sueess, M.J.; Schiefler, G.L.; Jacques, V.L.; Carbone, D.; Chrastina, D.; Isella, G.; Spolenak, R.; Stangl, J.; Sigg, H. Scanning X-ray strain microscopy of inhomogeneously strained Ge micro-bridges. *J. Synchrotron Radiat.* **2014**, *21*, 111–118. [CrossRef]
6. Ulvestad, A.; Singer, A.; Cho, H.-M.; Clark, J.N.; Harder, R.; Maser, J.; Meng, Y.S.; Shpyrko, O.G. Single Particle Nanomechanics in Operando Batteries via Lensless Strain Mapping. *Nano Lett.* **2014**, *14*, 5123–5127. [CrossRef]
7. Davtyan, A.; Lehmann, S.; Kriegner, D.; Zamani, R.R.; Dick, K.A.; Bahrami, D.; Al-Hassan, A.; Leake, S.J.; Pietsch, U.; Holý, V. Characterization of individual stacking faults in a wurtzite GaAs nanowire by nanobeam X-ray diffraction. *J. Synchrotron Radiat.* **2017**, *24*, 981–990. [CrossRef]
8. Johannes, A.; Salomon, D.; Martinez-Criado, G.; Glaser, M.; Lugstein, A.; Ronning, C. In operando x-ray imaging of nanoscale devices: Composition, valence, and internal electrical fields. *Sci. Adv.* **2017**, *3*, eaao4044. [CrossRef]
9. Chayanun, L.; Dagytė, V.; Troian, A.; Salomon, D.; Borgström, M.T.; Wallentin, J. Spectrally resolved x-ray beam induced current in a single InGaP nanowire. *Nanotechnology* **2018**, *29*, 454001. [CrossRef]
10. Troian, A.; Otnes, G.; Zeng, X.; Chayanun, L.; Dagytė, V.; Hammarberg, S.; Salomon, D.; Timm, R.; Mikkelsen, A.; Borgström, M.T.; et al. Nanobeam X-ray Fluorescence Dopant Mapping Reveals Dynamics of in Situ Zn-Doping in Nanowires. *Nano Lett.* **2018**, *18*, 6461–6468. [CrossRef]
11. Chayanun, L.; Otnes, G.; Troian, A.; Hammarberg, S.; Salomon, D.; Borgström, M.T.; Wallentin, J. Nanoscale mapping of carrier collection in single nanowire solar cells using X-ray beam induced current. *J. Synchrotron Radiat.* **2019**, *26*, 102–108. [CrossRef]
12. Ahn, Y.H.; Tsen, A.W.; Kim, B.; Park, Y.W.; Park, J. Photocurrent Imaging of p−n Junctions in Ambipolar Carbon Nanotube Transistors. *Nano Lett.* **2007**, *7*, 3320–3323. [CrossRef] [PubMed]
13. Hanoka, J.I. Electron-beam-induced current characterization of polycrystalline silicon solar cells. *Sol. Cells* **1980**, *1*, 123–139. [CrossRef]
14. Ulvestad, A.; Singer, A.; Clark, J.N.; Cho, H.M.; Kim, J.W.; Harder, R.; Maser, J.; Meng, Y.S.; Shpyrko, O.G. Topological defect dynamics in operando battery nanoparticles. *Science* **2015**, *348*, 1344–1347. [CrossRef] [PubMed]
15. Wallentin, J.; Osterhoff, M.; Salditt, T. In Operando X-Ray Nanodiffraction Reveals Electrically Induced Bending and Lattice Contraction in a Single Nanowire Device. *Adv. Mater.* **2016**, *28*, 1788–1792. [CrossRef] [PubMed]

16. Karpov, D.; Liu, Z.; Rolo, T.d.S.; Harder, R.; Balachandran, P.V.; Xue, D.; Lookman, T.; Fohtung, E. Three-dimensional imaging of vortex structure in a ferroelectric nanoparticle driven by an electric field. *Nat. Commun.* **2017**, *8*, 280. [CrossRef]
17. Lazarev, S.; Dzhigaev, D.; Bi, Z.; Nowzari, A.; Kim, Y.Y.; Rose, M.; Zaluzhnyy, I.A.; Gorobtsov, O.Y.; Zozulya, A.V.; Lenrick, F.; et al. Structural Changes in a Single GaN Nanowire under Applied Voltage Bias. *Nano Lett.* **2018**, *18*, 5446–5452. [CrossRef]
18. Godard, P.; Carbone, G.; Allain, M.; Mastropietro, F.; Chen, G.; Capello, L.; Diaz, A.; Metzger, T.H.; Stangl, J.; Chamard, V. Three-dimensional high-resolution quantitative microscopy of extended crystals. *Nat. Commun.* **2011**, *2*, 568. [CrossRef]
19. Hill, M.O.; Calvo-Almazan, I.; Allain, M.; Holt, M.V.; Ulvestad, A.; Treu, J.; Koblmüller, G.; Huang, C.; Huang, X.; Yan, H.; et al. Measuring Three-Dimensional Strain and Structural Defects in a Single InGaAs Nanowire Using Coherent X-ray Multiangle Bragg Projection Ptychography. *Nano Lett.* **2018**, *18*, 811–819. [CrossRef]
20. Johansson, U.; Vogt, U.; Mikkelsen, A. NanoMAX: A hard x-ray nanoprobe beamline at MAX IV. *SPIE* **2013**, *8851*, 88510L.
21. Eriksson, M.; Malmgren, L.; Al-Dmour, E.; Thorin, S.; Johansson, M.; Leemann, S.; Andersson, Å; Tavares, P. Commissioning of the MAX IV light source. In Proceedings of the IPAC 2016, Busan, Korea, 8–13 May 2016.
22. Memisevic, E.; Hellenbrand, M.; Lind, E.; Persson, A.R.; Sant, S.; Schenk, A.; Svensson, J.; Wallenberg, R.; Wernersson, L.-E. Individual Defects in InAs/InGaAsSb/GaSb Nanowire Tunnel Field-Effect Transistors Operating below 60 mV/decade. *Nano Lett.* **2017**, *17*, 4373–4380. [CrossRef]
23. Otnes, G.; Barrigón, E.; Sundvall, C.; Svensson, K.E.; Heurlin, M.; Siefer, G.; Samuelson, L.; Åberg, I.; Borgström, M.T. Understanding InP Nanowire Array Solar Cell Performance by Nanoprobe-Enabled Single Nanowire Measurements. *Nano Lett.* **2018**, *18*, 3038–3046. [CrossRef] [PubMed]
24. Bunk, O.; Bech, M.; Jensen, T.H.; Feidenhans'l, R.; Binderup, T.; Menzel, A.; Pfeiffer, F. Multimodal x-ray scatter imaging. *New J. Phys.* **2009**, *11*, 123016. [CrossRef]
25. Rodenburg, J.M. Ptychography and Related Diffractive Imaging Methods. *Adv. Imaging Electron Phys.* **2008**, *150*, 87–184.
26. Rodnyi, P.A. *Physical Processes in Inorganic Scintillators*; CRC press: Boca Raton, FL, USA, 1997.
27. Nikl, M. Scintillation detectors for x-rays. *Meas. Sci. Technol.* **2006**, *17*, R37–R54. [CrossRef]
28. Lecoq, P.; Gektin, A.; Korzhik, M. *Inorganic Scintillators for Detector Systems: Physical Principles and Crystal Engineering*; Springer: Berlin/Heidelberg, Germany, 2016.
29. Eymery, J.; Rieutord, F.; Favre-Nicolin, V.; Robach, O.; Niquet, Y.-M.; Fröberg, L.; Mårtensson, T.; Samuelson, L. Strain and Shape of Epitaxial InAs/InP Nanowire Superlattice Measured by Grazing Incidence X-ray Techniques. *Nano Lett.* **2007**, *7*, 2596–2601. [CrossRef] [PubMed]
30. Diaz, A.; Mocuta, C.; Stangl, J.; Mandl, B.; David, C.; Vila-Comamala, J.; Chamard, V.; Metzger, T.H.; Bauer, G. Coherent diffraction imaging of a single epitaxial InAs nanowire using a focused x-ray beam. *Phys. Rev. B* **2009**, *79*, 125324. [CrossRef]
31. Newton, M.C.; Leake, S.J.; Harder, R.; Robinson, I.K. Three-dimensional imaging of strain in a single ZnO nanorod. *Nat. Mater.* **2009**, *9*, 120. [CrossRef]
32. Favre-Nicolin, V.; Mastropietro, F.; Eymery, J.; Camacho, D.; Niquet, Y.M.; Borg, B.M.; Messing, M.E.; Wernersson, L.E.; Algra, R.E.; Bakkers, E.P.A.M.; et al. Analysis of strain and stacking faults in single nanowires using Bragg coherent diffraction imaging. *New J. Phys.* **2010**, *12*, 035013. [CrossRef]
33. Haag, S.T.; Richard, M.-I.; Welzel, U.; Favre-Nicolin, V.; Balmes, O.; Richter, G.; Mittemeijer, E.J.; Thomas, O. Concentration and Strain Fields inside a Ag/Au Core–Shell Nanowire Studied by Coherent X-ray Diffraction. *Nano Lett.* **2013**, *13*, 1883–1889. [CrossRef]
34. Stankevič, T.; Mickevičius, S.; Schou Nielsen, M.; Kryliouk, O.; Ciechonski, R.; Vescovi, G.; Bi, Z.; Mikkelsen, A.; Samuelson, L.; Gundlach, C. Measurement of strain in InGaN/GaN nanowires and nanopyramids. *J. Appl. Crystallogr.* **2015**, *48*, 344–349. [CrossRef]
35. Schroth, P.; Jakob, J.; Feigl, L.; Mostafavi Kashani, S.M.; Vogel, J.; Strempfer, J.; Keller, T.F.; Pietsch, U.; Baumbach, T. Radial Growth of Self-Catalyzed GaAs Nanowires and the Evolution of the Liquid Ga-Droplet Studied by Time-Resolved in Situ X-ray Diffraction. *Nano Lett.* **2018**, *18*, 101–108. [CrossRef] [PubMed]
36. Wallentin, J.; Osterhoff, M.; Wilke, R.N.; Persson, K.-M.; Wernersson, L.-E.; Sprung, M.; Salditt, T. Hard X-ray Detection Using a Single 100 nm Diameter Nanowire. *Nano Lett.* **2014**, *14*, 7071–7076. [CrossRef] [PubMed]

37. Hieslmair, H.; Istratov, A.A.; Sachdeva, R.; Weber, E.R. *New Synchrotron-Radiation-Based Technique to Study Localized Defects in Silicon: 'EBIC' with X-ray Excitation*; LBNL/ALS–43453; Ernest Orlando Lawrence Berkeley National Lab.: Berkeley, CA, USA, 2000; Available online: https://inis.iaea.org/search/search.aspx?orig_q=RN:33061273 (accessed on 15 August 2019).
38. Vyvenko, O.F.; Buonassisi, T.; Istratov, A.A.; Weber, E.R. X-ray beam induced current/microprobe x-ray fluorescence: Synchrotron radiation-*based* x-ray microprobe techniques for analysis of the recombination activity and chemical nature of metal impurities in silicon. *J. Phys. Condens. Matter* **2004**, *16*, S141. [CrossRef]
39. Buonassisi, T.; Heuer, M.; Vyvenko, O.F.; Istratov, A.A.; Weber, E.R.; Cai, Z.; Lai, B.; Ciszek, T.F.; Schindler, R. Applications of synchrotron radiation X-ray techniques on the analysis of the behavior of transition metals in solar cells and single-crystalline silicon with extended defects. *Phys. B: Condens. Matter* **2003**, *340–342*, 1137–1141. [CrossRef]
40. Buonassisi, T.; Istratov, A.A.; Pickett, M.D.; Marcus, M.A.; Hahn, G.; Riepe, S.; Isenberg, J.; Warta, W.; Willeke, G.; Ciszek, T.F.; et al. Quantifying the effect of metal-rich precipitates on minority carrier diffusion length in multicrystalline silicon using synchrotron-based spectrally resolved x-ray beam-induced current. *Appl. Phys. Lett.* **2005**, *87*, 044101. [CrossRef]
41. Seifert, W.; Vyvenko, O.; Arguirov, T.; Kittler, M.; Salome, M.; Seibt, M.; Trushin, M. Synchrotron-based investigation of iron precipitation in multicrystalline silicon. *Superlattices Microstruct.* **2009**, *45*, 168–176. [CrossRef]
42. West, B.; Husein, S.; Stuckelberger, M.; Lai, B.; Maser, J.; Stripe, B.; Rose, V.; Guthrey, H.; Al-Jassim, M.; Bertoni, M. Correlation between grain composition and charge carrier collection in Cu(In,Ga)Se2 solar cells. In Proceedings of the 2015 IEEE 42nd Photovoltaic Specialist Conference (PVSC), New Orleans, LA, USA, 14–19 June 2015; pp. 1–4.
43. Stuckelberger, M.; Nietzold, T.; Hall, G.N.; West, B.; Werner, J.; Niesen, B.; Ballif, C.; Rose, V.; Fenning, D.P.; Bertoni, M.I. Elemental distribution and charge collection at the nanoscale on perovskite solar cells. In Proceedings of the 2016 IEEE 43rd Photovoltaic Specialists Conference (PVSC), Portland, OR, USA, 5–10 June 2016; pp. 1191–1196.
44. Osterhoff, M.; Eberl, C.; Döring, F.; Wilke, R.N.; Wallentin, J.; Krebs, H.-U.; Sprung, M.; Salditt, T. Towards multi-order hard X-ray imaging with multilayer zone plates. *J. Appl. Crystallogr.* **2015**, *48*, 116–124. [CrossRef]
45. Bajt, S.; Prasciolu, M.; Fleckenstein, H.; Domaracký, M.; Chapman, H.N.; Morgan, A.J.; Yefanov, O.; Messerschmidt, M.; Du, Y.; Murray, K.T.; et al. X-ray focusing with efficient high-NA multilayer Laue lenses. *Light: Sci. Amp; Appl.* **2018**, *7*, 17162. [CrossRef]
46. Bell, P.; Hardion, V.; Jamróz, J.; Lidón-Simon, J. Control and Data Acquisition Using TANGO and SARDANA at the Nanomax Beamline at MAX IV. In Proceedings of the 16th International Conference on Accelerator and Large Experimental Control Systems, Barcelona, Spain, 8–13 October 2017; pp. 900–904.
47. Spear, J.D. Shot noise in x-ray measurements with p-i-n diodes. *Rev. Sci. Instrum.* **2005**, *76*, 076101. [CrossRef]
48. Stuckelberger, M.; West, B.; Nietzold, T.; Lai, B.; Maser, J.M.; Rose, V.; Bertoni, M.I. Engineering solar cells *based on* correlative X-ray microscopy. *J. Mater. Res.* **2017**, *32*, 1825–1854. [CrossRef]
49. Yang, C.; Pyry, K.; Mats-Erik, P.; Nicklas, A. Optimization of the short-circuit current in an InP nanowire array solar cell through opto-electronic modeling. *Nanotechnology* **2016**, *27*, 435404.
50. Alig, R.C.; Bloom, S. Secondary-electron-escape probabilities. *J. Appl. Phys.* **1978**, *49*, 3476–3480. [CrossRef]
51. Chahine, G.A.; Richard, M.-I.; Homs-Regojo, R.A.; Tran-Caliste, T.N.; Carbone, D.; Jacques, V.L.R.; Grifone, R.; Boesecke, P.; Katzer, J.; Costina, I.; et al. Imaging of strain and lattice orientation by quick scanning X-ray microscopy combined with three-dimensional reciprocal space mapping. *J. Appl. Crystallogr.* **2014**, *47*, 762–769. [CrossRef]
52. Wallentin, J.; Jacobsson, D.; Osterhoff, M.; Borgström, M.T.; Salditt, T. Bending and Twisting Lattice Tilt in Strained Core–Shell Nanowires Revealed by Nanofocused X-ray Diffraction. *Nano Lett.* **2017**, *17*, 4143–4150. [CrossRef]

© 2019 by the authors. Licensee MDPI, Basel, Switzerland. This article is an open access article distributed under the terms and conditions of the Creative Commons Attribution (CC BY) license (http://creativecommons.org/licenses/by/4.0/).